Development of a software trigger algorithm for electron identification using the NA62 RICH Cherenkov detector

Valeria Fascianelli

A Thesis submitted to
the University of Birmingham
for the degree of
Master by Research

Supervisors:
Dr. Evgueni Goudzovski
Prof. Cristina Lazzeroni

Particle Physics Group,
School of Physics and Astronomy,
University of Birmingham
March 14, 2016

Abstract

The thesis focuses on the development of a new algorithm able to identify an electron Cherenkov ring using the NA62 Ring Imaging CHerenkov detector (RICH). The algorithm is developed to act as an online Level 1 trigger algorithm and its execution time is studied to make it as fast as possible. In parallel, an efficiency analysis of the official offline NA62 RICH multi-ring reconstruction algorithm is performed in case it will be used as an online trigger algorithm. Studies on the efficiency and the rejection factor of the trigger cut to select the lepton number violating process $K^+ \to \pi^- e^+ e^+$ are described. Concerning the Level 1 trigger cut strategy, it is based on the use of the RICH detector only. Finally, a brief description of the NA62 PC-farm, where all the software trigger algorithms are implemented, is described.

Contents

List of Figures

List of Tables

Introduction

The Standard Model [1] of particle physics is a theoretical framework that describes and predicts particle physics phenomena. Experimental results have confirmed with a high level of accuracy the validity of the Standard Model. The discovery of the Higgs boson at the CERN LHC [2] represents one of the latest successes of the Standard Model predictions. Nevertheless, some aspects of Nature are not successfully explained by the Standard Model. The neutrinos in the Standard Model are described as massless particles even though experimental observations of neutrino oscillations [3] demonstrate that neutrinos are not massless. The experimental evidence of neutrino oscillations is also an example of the Lepton Flavour Violating process, representing the first evidence of physics beyond the Standard Model. The Standard Model, indeed, does not impose any conservation law of the lepton flavour and lepton number quantities, and their conservation is not dictated by a local gauge symmetry (Noether's theorem).

Processes involving Lepton Number Violation have not been detected up to now. These processes, with a violation of the lepton number by 2 units ($\Delta L = 2$), are quite interesting since they could explain the issue on the nature of the neutrinos, i.e. Dirac or Majorana, and the origin of the neutrino mass [4].

The main physics goal of the NA62 experiment [5] is to measure the branching ratio of the Flavour Changing Neutral Current decay $K^+ \to \pi^+ \nu \bar{\nu}$. Parallel searches to the main physics aim can be performed, in particular the search for Lepton Number Violating processes $K^\pm \to \pi^\mp l^\pm l^\pm$ is foreseen.

This thesis is focused on the development of a new software trigger algorithm able to identify an electron Cherenkov ring using the Ring Imaging CHerenkov (RICH) detector of the NA62 experiment. The kaon decay to be selected by the trigger algorithm is the Lepton Number Violating $K^+ \to \pi^- e^+ e^+$ decay. In principle the algorithm can be applied to select every event with an electron in the final state.

The first chapter gives a theoretical overview on the Lepton Number Violating processes $K^\pm \to \pi^\mp l^\pm l^\pm$ and on the experimental status of the search for heavy neutrinos. The Lepton Number Violating processes $K^\pm \to \pi^\mp l^\pm l^\pm$, indeed, can be mediated by the sterile Majorana neutrinos. The sensitivity to the branching ratio of $K^+ \to \pi^- e^+ e^+$ that can be reached by the NA62 experiment is also analysed. A review of the previous experiments in the search of heavy neutrinos, ranging from PS-191 experiment [6] performed at PS at CERN during the eighties to the existing proposal for the SHiP experiment [7, 8] at CERN, is presented. A brief overview of the physics behind the $K^+ \to \pi^+ \nu\bar{\nu}$ decay is also described.

In the second chapter, the NA62 experimental set up is described with particular attention to the RICH detector that is the main detector in the Level 1 (L1) software trigger studies. An overview of the NA62 trigger system and data acquisition is also presented.

An algorithm to reconstruct trackless multi-ring events, based on the geometrical Ptolemy's theorem, is described in the third chapter. The official NA62 RICH multi-ring reconstruction software is based on the Ptolemy's theorem. An analysis on the efficiency of this algorithm is performed and the results are discussed.

Studies of the trigger cut applied at L1 software-trigger stage to select multi-track events using the RICH detector only are presented in the fourth chapter. A cut based on the spatial distribution of the RICH PhotoMultiplier Tube (PMT) hits is explored in order to distinguish single-track from multi-track events. The event rate after a Level 0 (L0) and L1 trigger cut is shown. The $K^+ \to \pi^+ e^+ e^-$ decay is chosen as multi-track signal to be selected. A further trigger strategy is then studied to select the chosen signal and to suppress one of the main sources of background.

In the fifth chapter, a new L1 software trigger algorithm to identify an electron Cherenkov ring is described. Efficiency studies of the algorithm in selecting the signal are performed tuning the main parameters of the algorithm in order to have the best efficiency. Since the algorithm has to run as on-line software trigger, running time constraints are important: studies on the time improvement of the algorithm are described in this chapter.

The last chapter is focused on a technical description of the NA62 data format and of the PC farm framework where all the trigger algorithms are implemented. The analysis performed with data collected during 2015 run to study the performance of the L1 trigger algorithms is described. Considerations on the time budget available for the online execution of the L1 algorithms are discussed.

A brief summary of the analysis and of results of the thesis is described in the final conclusions.

Chapter 1

The Lepton Number Violating processes and the $K^+ \to \pi^+ \nu\bar{\nu}$ decay: theoretical overview and experimental status

1.1 Phenomenology of the Lepton Number Violation for the $K^\pm \to \pi^\mp l^\pm l^\pm$ processes

The Standard Model does not impose any conservation law of the lepton flavour and lepton number quantities. Their conservation is not dictated by a local gauge symmetry (Noether's theorem). The experimental evidence of neutrino oscillations is a proof of the Lepton Flavour Violation (LFV) process, representing the first phenomenon of physics beyond the Standard Model [3]. On the other hand, processes involving Lepton Number Violation (LNV) have not been detected up to now. Possible channels to be searched for include those that violate lepton number by two units ($\Delta L = 2$). These processes are quite interesting since they could explain the nature of the neutrinos, Dirac or Majorana, and the origin of the neutrino mass [4].

The $K^{\pm} \rightarrow \pi^{\mp} e^{\pm} e^{\pm}$ decay represents one of the lepton number violating processes and it is the signature that the software trigger strategy described in chapter 4 looks for.

Experimental observations of the neutrino oscillations demonstrate that neutrinos are not massless as predicted by the Standard Model. A Dirac mass term in the Standard Model is written as:

$$m\overline{\psi}\psi \tag{1.1}$$

where ψ is the Dirac spinor. Knowing that it can be decomposed into its left- and right-handed component,

$$\psi = \psi_R + \psi_L, \tag{1.2}$$

it follows that:

$$m\overline{\psi}\psi = m\overline{\psi_L}\psi_R + m\overline{\psi_R}\psi_L, \tag{1.3}$$

as $\overline{\psi_L}\psi_L = \overline{\psi_R}\psi_R = 0$. Hence Dirac particles in the Standard Model lagrangian, with non zero mass, must have both right and left handed states. Since the neutrino in the Standard Model has never been observed in its right handed component, it is not possible to write a neutrino mass term in the lagrangian $\mathcal{L}$ of the Standard Model. On the other hand, the experimental observation of the neutrino oscillations is a proof that the neutrinos are not massless and then a right handed component of the neutrinos state can be included in the lagrangian of the Standard Model. This leads to the open issue of the neutrino's nature as it can be either a Dirac or Majorana particle.

A Dirac particle is a fermion with 1/2 spin described by the Dirac equation

$$(i\partial_{\mu}\gamma^{\mu} - m)\psi = 0, \tag{1.4}$$

where γ^{μ} are the Dirac matrices and ψ is the 4-component-complex Dirac spinor.

A Majorana particle is a fermion described by the χ field satisfying the following relation:

$$C\overline{\chi}^T = e^{i\xi}\chi,\ |e^{i\xi}|^2 = 1, \tag{1.5}$$

where C is the charge conjugation operator and $e^{i\xi}$ is an arbitrary phase. The χ field is an eigenstate of the C operator as explained by the relation 1.5 and it means that the Majorana particle is its own antiparticle. Neutrinos are the only candidates for Majorana particles since these do not have any $U(1)$ charge, such as the electric charge.

If a particle is its own antiparticle it implies that the Majorana field has also non-zero propagators like $\langle 0| T(\psi_\alpha(x)\psi_\beta(y)) |0\rangle$ and $\langle 0| T(\overline{\psi}_\alpha(x)\overline{\psi}_\beta(y)) |0\rangle$, in addition to a non-zero propagator $\langle 0| T(\psi_\alpha(x)\overline{\psi}_\beta(y)) |0\rangle$. The T operator is the time-ordering operator. The relation 1.5 leads to:

$$\langle 0| T(\psi_\alpha(x)\psi_\beta(y)) |0\rangle = -e^{-i\xi} \langle 0| T(\psi_\alpha(x)\overline{\psi}_\beta(y)) |0\rangle\, C \neq 0 \tag{1.6}$$

$$\langle 0| T(\overline{\psi}_\alpha(x)\overline{\psi}_\beta(y)) |0\rangle = e^{i\xi}C^{-1} \langle 0| T(\psi_\alpha(x)\overline{\psi}_\beta(y)) |0\rangle \neq 0. \tag{1.7}$$

These propagators would violate the lepton number by two units. Processes violationg the lepton number by two units like $K^\pm \to \pi^\mp l^\pm l^\pm (l = e, \mu)$ can be justified by the mediation of a massive Majorana neutrinos. The lowest order contribution to the amplitude $\mathcal{A}_{\pi ll} = \mathcal{A}(K^\pm \to \pi^\mp l^\pm l^\pm)$ is illustrated by the Feynman diagram in Figure 1.1.

The branching ratio $\mathcal{B}(K^\pm \to \pi^\mp l^\pm l^\pm)$ can be studied in the limit of light sterile neutrinos (the neutrino mass is much smaller than the kaon mass), in the limit of heavy sterile neutrinos (the neutrino mass is much larger than the kaon mass) and finally when the neutrino is resonant, i.e. if at least one sterile neutrino has a mass within the mass-range shown in relation 1.8, the $K^\pm \to \pi^\mp l^\pm l^\pm$ decay may occur via resonant production of the heavy neutrino (for the production and decay mechanism of heavy neutrino see relations 1.9). In this section $\mathcal{B}(K^\pm \to \pi^\mp l^\pm l^\pm)$ is studied for resonant sterile neutrinos.

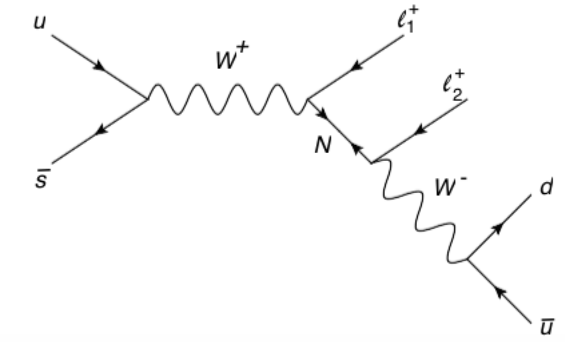

Figure 1.1: Feynman diagrams describing the contribution of the massive Majorana neutrinos to the $\Delta L = 2$ process $K^{\pm} \to \pi^{\mp} l_1^{\pm} l_2^{\pm}$, where l_1 and l_2 indicate the first and the second lepton, respectively.

Only one sterile neutrino is taken into account and it is denoted N_4. If a neutrino has a mass range such that (where m_π, m_l, m_{N_4} and m_K are the mass of pion, lepton, sterile neutrino and kaon, respectively)

$$m_\pi + m_l \leq m_{N_4} \leq m_K - m_l, \tag{1.8}$$

the lepton number violating processes $K^{\pm} \to \pi^{\mp} l^{\pm} l^{\pm}$ can occur by the mediation of the resonant sterile Majorana neutrino. In particular the processes are the following:

$$\begin{aligned} &K^{\pm} \to l^{\pm} N_4, \\ &N_4 \to \pi^{\mp} l^{\pm}. \end{aligned} \tag{1.9}$$

The maximum value of the mass that the sterile neutrino can have is obtained by kinematical constraints of the production process in relation 1.9. Concerning the minimum value reachable for the sterile neutrino mass, it is dictated by kinematical constraints of the decay process in relation 1.9. Considering a Majorana sterile neutrino with a mass $m_{N_4} = 300$ MeV, the branching ratio $\mathcal{B}(K^{\pm} \to \pi^{\mp} l^{\pm} l^{\pm})$ has the following form [9]:

$$\begin{aligned}\mathcal{B}(K^{\pm} \rightarrow \pi^{\mp} l^{\pm} l^{\pm}) &\sim 10^{-19}\mathrm{GeV} \times \frac{1}{\Gamma_{N_4}} |\mathcal{U}_{l4}|^4 \\ &\sim 10^{-7}\mathrm{ps}^{-1} \times \tau_{N_4} \mid \mathcal{U}_{l4} \mid^4,\end{aligned} \tag{1.10}$$

where $\mathcal{U}_{l4}$ is the mixing matrix element for the Majorana sterile neutrino. Further considerations on the sensitivity that NA62 can reach in the estimate of the branching ratio of $K^+ \rightarrow \pi^- e^+ e^+$ decay, are described in Section 1.1.2.

1.1.1 Experimental searches for heavy neutrinos

The study of $\mathcal{B}(K^{\pm} \rightarrow \pi^{\mp} l^{\pm} l^{\pm})$ is connected to the search for the exotic particles as heavy neutrinos.

The PS-191 beam dump experiment [6] has been performed during the eighties at PS at CERN. It looked for the heavy neutrino decays into lepton-pion and positron-electron-light neutrinos. The heavy neutrinos were searched through the decays of mesons produced by the interaction of 19.2-GeV proton beam on a beryllium target, assuming lepton conservation at production. The neutrino could be produced with either electronic flavour ν_e or muonic flavour ν_μ according to the other lepton. This experiment was designed to look for neutrino decays into $e^+ e^- \nu$. No events, above expectations of zero events, compatible with this decay have been observed and the experiment put a stringent exclusion limit on the mixing parameters $\mathcal{U}_{e4}$ and $\mathcal{U}_{\mu 4}$ in the mass range below 500 MeV, as shown in Figure 1.2. Early experimental results are also shown, in particular the printed references 9, 10, 11, 12 on the plots refer to [10], [11], [12], [13], respectively. The lowest limit on mixing parameters put by PS-191 for heavy neutrino masses less than 100 MeV is set searching for heavy neutrino produced via pion decay, while the other limit ranging up to ∼ 500 MeV mass is set searching for heavy neutrino produced via kaon decay.

Two different strategies can be explored to search for heavy neutrino: the first one consists of looking for peaks in the two body decays of pion and kaons (peak

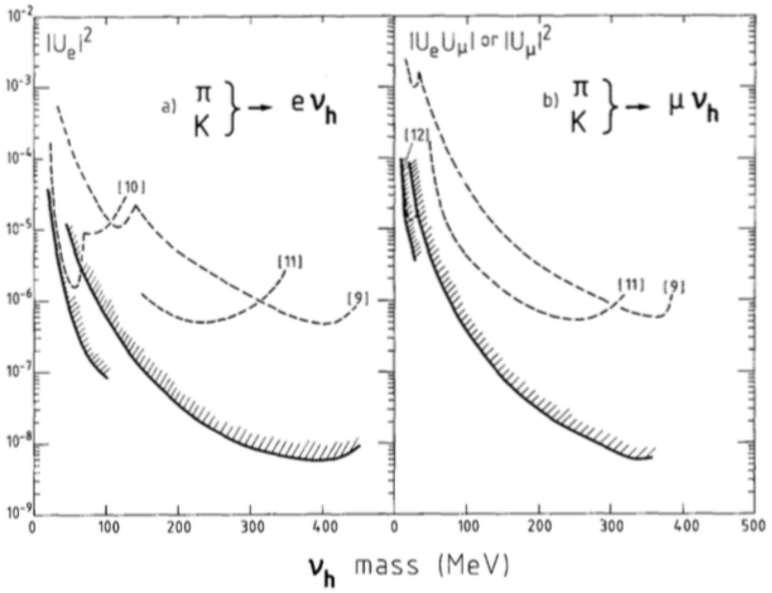

Figure 1.2: Upper limits on the mixing parameters obtained by PS-191. On the left the limit of the mixing parameter is shown for the production of heavy neutrino with electron while on the right the limit of the mixing parameter is shown for the heavy neutrino produced with muon. Early experiment results are also shown [6].

searches), with a neutrino mass 10 MeV $\leq m_{\mathrm{N}} \leq m_{\mathrm{K}}$ [14], the second one consists in searching for decay products of heavy neutrino, that is the strategy adopted by PS-191 experiment[4].

A survey on the limit of the mixing parameters $\mathcal{U}_{e4}$, $\mathcal{U}_{\mu 4}$ is shown in Figures 1.3 and 1.4 with a neutrino mass range extended up to 100 GeV [4, 15]. Figure 1.3 shows the limit on the mixing parameter $\mathcal{U}_{e4}$ as a function of the neutrino mass ranging from 10 MeV up to 100 GeV. Different experimental results are shown via the search of heavy neutrino at production, i.e. peak searches, or via heavy neutrino decays. The limits reached by the CHARM [16] and NA3 [17] beam-dump experiments are from searches of heavy neutrino decays as the PS-191 experiment [6]. The TRIUMPH [18] and KEK [12] experiments searched for heavy neutrino at production (peak searches) and their limits are labelled $\pi \rightarrow e\nu$ and $K \rightarrow e\nu$, respectively. The limits put by L3 [19] and DELPHI [20] experiment at LEP come from search of heavy neutrino at production and a following decay in Z^0. For a given neutrino mass m_4, the NA3 limit puts a range on the matrix element value and vice versa, at a given matrix element, a range on the neutrino mass is obtained.

Figure 1.4 shows the limits on the mixing parameter $\mathcal{U}_{\mu 4}$ as a function of the neutrino mass ranging from 100 MeV up to 100 GeV. Different experimental results are shown via the search of heavy neutrino at production, i.e. peak searches, or via heavy neutrino decays. The limits labelled by $K \rightarrow \mu\nu$ are reached by the KEK [12], NuTeV [21], BEBC [22], FMMF [23], CHARM II [24] and PS191 [6]. All these experiments were beam dump experiments searching for heavy neutrino decays.

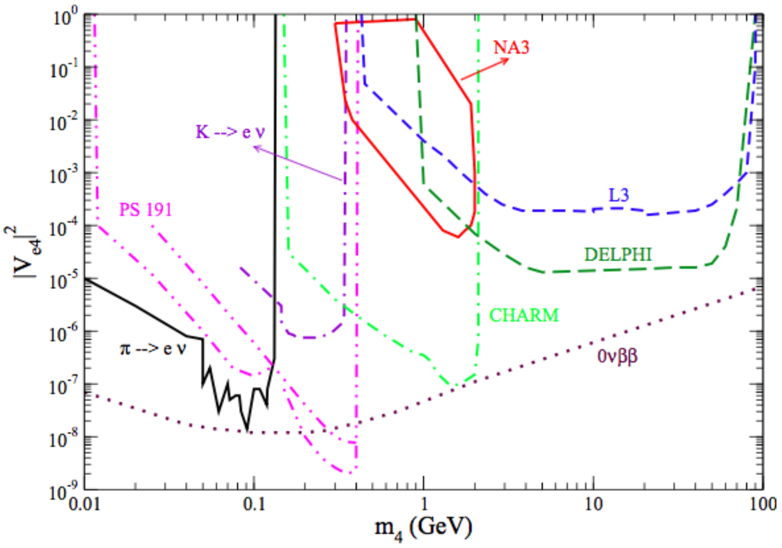

Figure 1.3: Upper limits on $|\mathcal{U}_{e4}|^2$ (i.e. $|V_{e4}|^2$ on the y-axis) from different experiments [4].

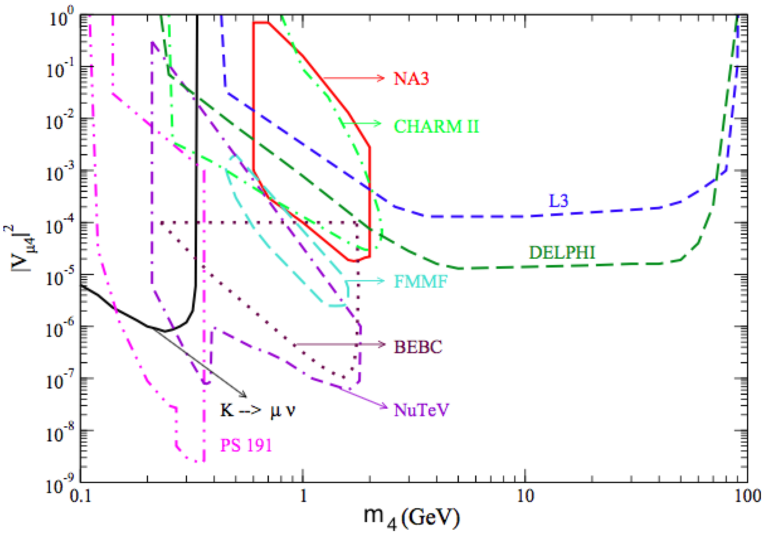

Figure 1.4: Upper limits on $|\mathcal{U}_{\mu4}|^2$(i.e. $|\mathrm{V}_{\mu4}|^2$ on the y-axis) from different experiments [4].

As already mentioned, the search for lepton number violating processes ($\Delta\mathrm{L} = 2$), like $K^+ \to \pi^- e^+ e^+$, is linked to the search for Majorana neutrinos since these processes can be explained by the mediation of on-shell or virtual Majorana neutrino.

The experiments in the B-physics sector represent an additional probe to the previous experiments of the low mass region. The LHCb experiment [25, 26] has recently given an important result on the limit of $|\mathcal{U}_{\mu4}|$ looking for heavy neutrinos produced by the $B^- \to \pi^+\mu^-\mu^-$ decay. The upper limits have been estimated for the heavy neutrino mass ranging from 250 MeV up to 5 GeV with 3fb^{-1} of integrated luminosity. The upper limit at 95% CL on $|\mathcal{U}_{\mu4}|^2$ is shown in Figure 1.5 (in the current figure, $|\mathcal{U}_{\mu4}|^2$ is replaced by $|\mathrm{V}_{\mu4}|^2$ on the y-axis). It is mass dependent and it ranges from $\sim 10^{-2}$ for neutrino masses of $\sim$ 250 MeV and larger than 4 GeV up to 10^{-4} for a neutrino mass of $\sim$ 2 GeV [25, 26].

A new beam dump experiment at the CERN SPS named SHIP [7, 8] will use charm

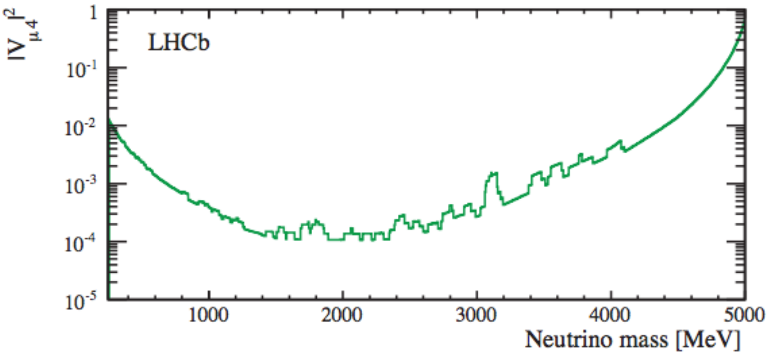

Figure 1.5: Upper limit at 95% CL on $|\mathcal{U}_{\mu 4}|^2$ (i.e. $|\mathrm{V}_{\mu 4}|^2$ on the y-axis) as a function of the neutrino mass from LHCb experiment [25, 26].

mesons decays to search for heavy neutrinos. The production mechanisms are

$$\begin{aligned}&D \to KlN\\&D_s \to lN\\&D_s \to \tau\nu \text{ followed by } \tau \to l\nu \text{ or } \tau \to \pi N\end{aligned} \tag{1.11}$$

where $l = e, \mu$. The most promising heavy neutrino decays among the two-body decays for the SHIP experiment are: $N \to l\pi^+$ and $N \to l\rho^+$, where $l = e, \mu$ [8]. The SHIP experiment will be able to reach a sensitivity for the parameter $|\mathcal{U}_{\mu 4}|^2$ between 10^{-7} and 10^{-9} for heavy neutrino masses below 2 GeV [7].

1.1.2 The NA62 sensitivity

The expected number of kaon decays in the NA62 fiducial region for two years of data taking is:

$$N_K \simeq 10.6 \times 10^{12}. \tag{1.12}$$

The sensitivity that NA62 can reach in the estimate of the branching ratio of the $K^+ \to \pi^- e^+ e^+$ decay is studied in this section. The Upper Limit (UL) for the branching ratio $\mathcal{B}(K^+ \to \pi^- e^+ e^+)$ is computed as follows:

$$\mathcal{B}(K^+ \to \pi^- e^+ e^+) = \frac{N(K^+ \to \pi^- e^+ e^+)}{N_K \epsilon_{\pi ee}}, \tag{1.13}$$

where $N(K^+ \to \pi^- e^+ e^+)$ is the number of signal events where UL is estimated using the Feldman-Cousins statistical method for 90% of CL [27], assuming to have zero background and to observe zero event candidates and $\epsilon_{\pi ee}$ is the geometrical acceptance of the signal.

The $K^+ \to \pi^- e^+ e^+$ geometrical acceptance $\epsilon_{\pi ee}$ is $\sim$ 30%. It is obtained simulating 1000 $K^+ \to \pi^+ e^+ e^-$ events in the NA62 decay region, and checking how many of these events have three reconstructed tracks by the spectrometer, at least two Cherenkov rings detected by the Ring Imaging Cherenkov detector, and at least two clusters in the electromagnetic calorimeter LKr (the NA62 experimental set up is described in chapter 2).

To observe zero signal events where zero background events are expected, the UL on the number of signal events of $K^+ \to \pi^- e^+ e^+$ decays at 90% of CL, using the Feldman-Cousins statistical method, is:

$$N(K^+ \to \pi^- e^+ e^+) \; < \; 2.44 \quad @ \, 90\% \text{ CL}, \tag{1.14}$$

The UL on the branching ratio $\mathcal{B}(K^+ \to \pi^- e^+ e^+)$ that is estimated to be reached by NA62 in two years of data taking is:

$$\mathcal{B}(K^+ \to \pi^- e^+ e^+) \; < \; 0.77 \times 10^{-12} \quad @ \, 90\% \text{ CL}. \tag{1.15}$$

The actual experimental limit on the branching ratio of the $K^+ \to \pi^- e^+ e^+$ decay is $\mathcal{B}(K^+ \to \pi^- e^+ e^+) < 6.4 \times 10^{-10}$ at 90% CL [3].

Considering now the scenario in the limit of the resonant sterile neutrino with a neutrino mass equal to 300 MeV (see Section 1.1, Equation 1.10 for $l = e$) the branching ratio is estimated to be [28, 9]:

$$\begin{aligned}\mathcal{B}(K^+ \to \pi^- e^+ e^+) &\sim 10^{-19}\text{GeV} \times \frac{1}{\Gamma_{N_4}} |\mathcal{U}_{e4}|^4 \\ &\sim 10^{-7}\ \text{ps}^{-1} \times \tau_{N_4} |\mathcal{U}_{e4}|^4 .\end{aligned} \tag{1.16}$$

From the relation in 1.16 the sensitivity to the mixing element depending on the neutrino lifetime is obtained. As the experimental sensitivity that NA62 can reach in the estimate of the branching ratio $\mathcal{B}(K^+ \to \pi^- e^+ e^+)$ is $\mathcal{O}(10^{-12})$, for the case where $\Gamma_{N_4} \lesssim 10^{-7}$ GeV (neutrino lifetime $\tau_{N_4} \gtrsim 10^{-5}$ ps), the NA62 experiment can place non-trivial constraints ($\mathcal{U}_{e4} < 1$) on the mixing matrix element $\mathcal{U}_{e4}$.

1.2 $K^+ \to \pi^+ \nu\bar{\nu}$ decay

1.2.1 The Cabibbo-Kobayashi-Maskawa matrix

The Cabibbo-Kobayashi-Maskawa matrix (V_{CKM}) allows to change from the mass eigenstates (d, s, b) to the weak eigenstates $(d^{'}, s^{'}, b^{'})$ which interact with the u, c, t quarks:

$$\begin{pmatrix} d' \\ s' \\ b' \end{pmatrix} = V_{CKM} \begin{pmatrix} d \\ s \\ b \end{pmatrix} = \begin{pmatrix} V_{ud} & V_{us} & V_{ub} \\ V_{cd} & V_{cs} & V_{cb} \\ V_{td} & V_{ts} & V_{tb} \end{pmatrix} \begin{pmatrix} d \\ s \\ b \end{pmatrix} .$$

Two parametrizations of the V_{CKM} available in literature are presented in this section: the Standard [29] and the Wolfenstein [30] parametrization.

The Standard parametrization

In the Standard parametrization the V_{CKM} matrix can be written as follows:

$$\begin{pmatrix} c_{12}c_{13} & s_{12}c_{13} & s_{13}e^{-i\delta} \\ -s_{12}c_{23} - c_{12}s_{23}s_{13}e^{i\delta} & c_{12}c_{23} - s_{12}s_{23}s_{13}e^{i\delta} & s_{23}c_{13} \\ s_{12}s_{23} - c_{12}c_{23}s_{13}e^{i\delta} & -s_{23}c_{12} - s_{12}c_{23}s_{13}e^{i\delta} & c_{23}c_{13} \end{pmatrix}$$

where $c_{ij} = \cos\theta_{\rm ij}$ and $s_{ij} = \sin\theta_{\rm ij}$ $(i, j = 1,\ 2,\ 3)$, and δ is the CP violation phase. The s_{13} and s_{23} are small numbers of the order $O(10^{-3})$ and $O(10^{-2})$ respectively, the $c_{13} \approx c_{23} \approx 1$ and the other four parameters are

$$s_{12} \overset{\rm def}{=} \mid V_{us} \mid, \quad s_{13} \overset{\rm def}{=} \mid V_{ub} \mid, \quad s_{23} \overset{\rm def}{=} \mid V_{cb} \mid, \quad \delta. \tag{1.17}$$

The CKM elements have been estimated by a plethora of experimental measurements. The present experimental results for the absolute value of the CKM elements are shown [3]:

$$\mid V_{CKM} \mid = \begin{pmatrix} 0.97426^{+0.00022}_{-0.00014} & 0.22539^{+0.00062}_{-0.00095} & 0.003501^{+0.000196}_{-0.000087} \\ 0.22526^{+0.00062}_{-0.00095} & 0.97345^{+0.00022}_{-0.00018} & 0.04070^{+0.00116}_{-0.00059} \\ 0.00846^{+0.00043}_{-0.00015} & 0.03996^{+0.00114}_{-0.00062} & 0.999165^{+0.000024}_{-0.000048} \end{pmatrix}$$

The Wolfenstein parametrization

In the Wolfenstein parametrization the four mixing parameters in 1.17 are replaced by:

$$\lambda, \quad A, \quad \rho, \quad \eta, \tag{1.18}$$

that are connected to the parameters in 1.17 by:

$$s_{12} = \lambda, \quad , s_{23} = A\lambda^2, \quad s_{13}e^{-i\delta} = A\lambda^3(\rho - i\eta). \tag{1.19}$$

The parameter ρ and η are then:

$$\rho = \frac{s_{13}}{s_{12}s_{23}}\cos\delta, \quad \eta = \frac{s_{13}}{s_{12}s_{23}}\sin\delta, \tag{1.20}$$

that are obtained by an exchange of variables from 1.17 to 1.18. The matrix V_{CKM} is written as follows:

$$\begin{pmatrix} 1-\frac{\lambda^2}{2} & \lambda & A\lambda^3(\varrho - \imath\eta) \\ -\lambda & 1-\frac{\lambda^2}{2} & A\lambda^2 \\ A\lambda^3(1-\varrho-\imath\eta) & -A\lambda^2 & 1 \end{pmatrix} + O(\lambda^4). \tag{1.21}$$

Each element of the V_{CKM} matrix, in the Wolfenstein parametrization, is written as a power series of the parameter $\lambda = |V_{us}| = 0.22$. Only the first few terms of the expansion, $O(\lambda^3)$, are kept due to the smallness of the λ parameter. According to the required level of accuracy, $O(\lambda^4)$ terms can be added to the V_{CKM} matrix in the Wolfenstein parametrization.

Wolfenstein parametrization at higher orders

Considering the parameters' definition in 1.19 and in 1.20, it is possible to write the standard parametrization in terms of powers of λ at higher orders defined as follows:

$$V_{ud} = 1 - \frac{1}{2}\lambda^2 - \frac{1}{8}\lambda^4 + O(\lambda^6) \tag{1.22}$$

$$V_{us} = \lambda + O(\lambda^7) \tag{1.23}$$

$$V_{ub} = A\lambda^3(\varrho - \imath\eta) \tag{1.24}$$

$$V_{cd} = -\lambda + \frac{1}{2}A^2\lambda^5\left(1 - 2(\varrho + \imath\eta)\right) + O(\lambda^7) \tag{1.25}$$

$$V_{cs} = 1 - \frac{1}{2}\lambda^2 - \frac{1}{8}\lambda^4(1+4A^2) + O(\lambda^6) \tag{1.26}$$

$$V_{cb} = A\lambda^2 + O(\lambda^8) \tag{1.27}$$

$$V_{td} = A\lambda^3 \left(1 - (\varrho + \imath\eta)\left(1 - \frac{1}{2}\lambda^2\right)\right) + O(\lambda^7) \tag{1.28}$$

$$V_{ts} = -A\lambda^2 + \frac{1}{2}A(1-2\varrho)\lambda^4 - \imath\eta A\lambda^4 + O(\lambda^6) \tag{1.29}$$

$$V_{tb} = 1 - \frac{1}{2}A^2\lambda^4 + O(\lambda^6). \tag{1.30}$$

The correction to the terms V_{us} and V_{cb} are of the order $O(\lambda^7)$ and $O(\lambda^8)$ respectively, and the term V_{ub} is unchanged. Introducing new variables $\overline{\rho} = \rho\left(1 - \frac{\lambda^2}{2}\right)$ and $\overline{\eta} = \left(1 - \frac{\lambda^2}{2}\right)$, the V_{us}, V_{cb}, V_{ub}, V_{tb} can be written with good accuracy as:

$$V_{us} = \lambda \tag{1.31}$$

$$V_{cb} = A\lambda^2 \tag{1.32}$$

$$V_{ub} = A\lambda^3(\varrho - \imath\eta) \tag{1.33}$$

$$V_{td} = A\lambda^3(1 - \bar{\varrho} - \imath\bar{\eta}). \tag{1.34}$$

1.2.2 The unitarity triangle

The V_{CKM} is a unitary matrix that means $\sum_k V_{ik}V_{jk}^* = \delta_{ij}$. If j and i are fixed, there is a relation between three complex numbers. Each relation can be represented by a triangle in the complex plane, known as "unitary triangle". One of the relations is:

$$V_{ud}V_{ub}^{*} + V_{cd}V_{cb}^{*} + V_{td}V_{tb}^{*} = 0. \tag{1.35}$$

An example of a "unitary triangle" is shown in Figure 1.6.

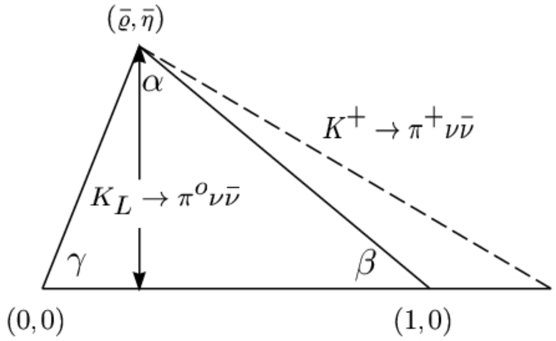

Figure 1.6: Unitarity triangle.

The measurement of the branching ratios of $K^{+} \to \pi^{+}\nu\bar{\nu}$ and $K_{L} \to \pi^{0}\nu\bar{\nu}$ leads to the knowledge of ρ and η parameters by the determination of the V_{td} matrix element.

1.2.3 Standard Model predictions for $K^{+} \to \pi^{+}\nu\bar{\nu}$

The rare decay $K^{+} \to \pi^{+}\nu\bar{\nu}$ is an extremely interesting process from the flavour physics point of view. It is a golden channel in the Flavour Changing Neutral Current (FCNC) modes and it is one of the cleanest decay modes mediated by the quark process $s \to d$ [31]. It is considered a golden channel in the FCNC processes for the following reasons:

- the rate is very small because of the Glashow-Iliopoulos-Maiani (GIM) suppression. For each of the penguin and box diagrams (see Figure 1.7), there are amplitudes with u, c and t quarks in the loops. Since the loop integrals scale with m_q^2 (m_q is the mass of the quark), the t quark contribution is the strongest. But because of the hierarchy of CKM matrix elements, $V_{td}^{*}V_{ts}$ is very tiny. So the total rate is very small (see Equation 1.40);

- the theoretical prediction is very precise for a number of reasons. The most important is that the hadronic matrix element, the factorizable part of the overall matrix element that accounts for the fact that the $s \to d$ transition does not take place among free quarks, but rather between an s quark that is bound into a kaon and a d quark that is bound into a pion, can be directly obtained from very precise existing measurements of the decays $K^+ \to e^+\pi^0\nu_e$ via a rotation in weak isospin (see Equation 1.37);
- there are no long distance contributions from states with intermediate photons that contribute to the total rate for $K^+ \to \pi^+\nu\bar{\nu}$.

The amplitude of the decay consists of two terms: one term is easily computed within the Standard Model rules, the second one is related to the hadronic part of the process and can be determined experimentally from the semileptonic decay of the kaon $K^+ \to \pi^0 e^+\nu$. The hadronic matrix, indeed, taking into account that the $s \to d$ transition does not happen among free quarks but between an s quark bound into a kaon and a d quark bound into a pion, can be estimated by the kaon semileptonic decay via a rotation in the weak isospin.

In the Standard Model this process is a combination of penguin diagrams (the first two diagrams on the left in Figure 1.7) and box diagram (the third diagram in Figure 1.7).

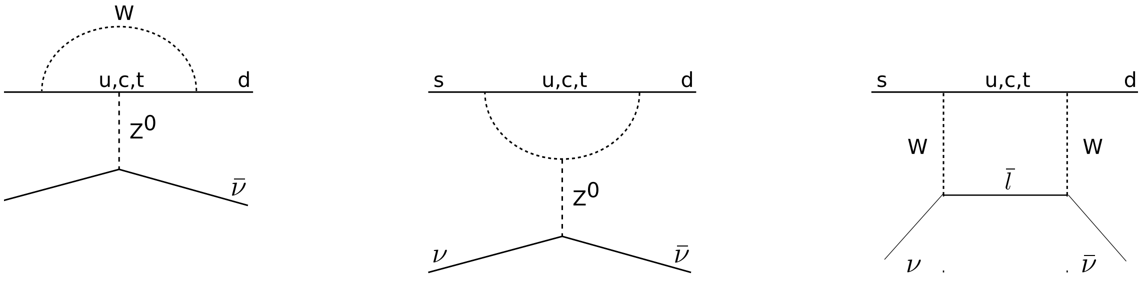

Figure 1.7: Feynman diagrams for $s \longrightarrow d\nu\bar{\nu}$ process.

In each of these Feynman diagrams the u, c, t quarks appear in the loops. The rate of the decay is very small because of the GIM suppression. The amplitude of the process, dictated by the GIM mechanism, is $A_q \sim m_q^2/m_W^2 V_{qs}^* V_{qd}$ where $q = u, c, t$. Because of the hierarchy of the CKM matrix elements, $V_{td}^* V_{ts}$ is very tiny and then the total rate is very small. The contribution of the top-quark is dominant for the $K^+ \to \pi^+ \nu\bar{\nu}$ process with a smaller contribution of the charm-quark. The contribution of the up-quark is negligible and then there are no long distance contributions with intermediate photons: the decay is a short distance process well described by the Fermi coupling:

$$H_{eff} = \sum_{l=e,\mu,\tau} \frac{G_l}{\sqrt{2}} \left(s\bar{d}\right)_{V-A} \left(\bar{\nu}_l \nu_l\right)_{V-A}, \tag{1.36}$$

where G_l is the effective coupling constant. Given G_l, the branching ratio comes from the branching ratio of the semileptonic decay $K^+ \to \pi^0 e^+ \nu$ via a rotation in the weak isospin:

$$BR(K^+ \to \pi^+ \nu\bar{\nu}) = \sum_{l=e,\mu,\tau} 2 r_{K^+} BR(K^+ \to \pi^0 e^+ \nu) \frac{|G_l|^2}{G_F^2 |V_{us}|^2} \tag{1.37}$$

where $r_{K^+} = 0.901$ [32] is due to the isospin breaking corrections in relating $K^+ \to \pi^+ \nu\bar{\nu}$ and $K^+ \to \pi^0 e^+ \nu$ decay [31]. The effective constant G_l can be expressed by the sum of two terms: the first one coming from a loop with the top-quark and the second one from a loop with the charm-quark:

$$G_l = \frac{\alpha G_F}{2\pi \sin^2(\Theta_W)} \left[V_{ts}^* V_{td} X(x_t) + V_{cs}^* V_{cd} X_{NL}^l\right], \tag{1.38}$$

where $x_t = (m_t/m_W)^2$, α is the electromagnetic coupling and θ_W is the weak mixing angle. The X coefficients depend on the loops and they are well known computed functions. The contribution of the top-quark is well known and the error on its estimate is due to the uncertainty on the knowledge of the top-quark mass. The smallest contribution is due to the charm-quark and it is affected by a higher uncertainty. Averaging over the three flavours of neutrinos the following expression is obtained:

$$P_0(X) = \frac{1}{\lambda^4} \left[\frac{2}{3} X_{NL}^e + \frac{1}{3} X_{NL}^\tau\right] = 0.42 \pm 0.06, \tag{1.39}$$

where λ is the $|V_{us}|$ in the Wolfenstein parametrization that means a theoretical error on the V_{td} estimate of $\sim$ 5-7%. This makes the $K^+ \to \pi^+ \nu\bar{\nu}$ decay one of the interesting channel to explore the "unitary triangle". The numerical prediction for the branching ratio is [33]:

$$\mathcal{B}(K^+ \to \pi^+ \nu\bar{\nu}) = (7.81^{+0.80}_{-0.71} \pm 0.29) \times 10^{-11}, \tag{1.40}$$

where the first error is due to the uncertainties on the parameters and the second error, which is due to theoretical issues such as the knowledge of the CKM elements and the quark masses, is expected to improve.

The $K^+ \to \pi^+ \nu\bar{\nu}$ decay, moreover, is very sensitive to new physics beyond the Standard Model. It is possible that, if the measured branching ratio is not compatible with the prediction of the Standard Model, the $K^+ \to \pi^+ \nu\bar{\nu}$ decay channel may give evidence of the presence of a new physics beyond the Standard Model.

In conclusion, the measurement of the branching ratio of the $K^+ \to \pi^+ \nu\bar{\nu}$ gives precise information on the "unitary triangle" and it is very sensitive to new physics beyond the Standard Model.

1.2.4 The experimental status

The first measurement of the branching ratio of the $K^+ \to \pi^+ \nu\bar{\nu}$ decay has been performed by the E787 and E949 [34] experiments at the Brookhaven National Laboratory with low-energy kaons stopped in a scintillating-fibre target. During four years of data taking, seven signal candidate events were observed. The probability to be a fluctuation around the $\sim$ 2 expected events of background is $\sim 10^{-3}$. The branching ratio has been estimated $\mathcal{B}(K^+ \to \pi^+ \nu\bar{\nu}) = 1.73^{+1.15}_{-1.05} \times 10^{-10}$ [35]. The result is consistent with the Standard Model prediction even though there is a significant difference between the theoretical precision and the experimental error.

The NA62 experiment at CERN aims to measure the branching ratio of the $K^+ \to \pi^+ \nu\bar{\nu}$ decay with a total uncertainty of 10% on the Standard Model prediction requiring $\mathcal{O}(100)$ events in two years of data taking. NA62 adopts a new strategy that has never been used in the search for $K^+ \to \pi^+\nu\bar{\nu}$ decay. The strategy consists of studying the decays of kaons in flight with a 75 GeV/c beam of kaons, protons and pions. The expected signal-background ratio is $S/B \sim 10$.

Chapter 2

The NA62 experimental setup, trigger and data acquisition

The NA62 experiment is located in the CERN North Area High Intensity Facility at the ECN3 cavern and it uses the SPS extraction line. Schematic descriptions of the CERN accelerator structure and of the NA62 detector are shown is Figure 2.1 and Figure 2.2, respectively.

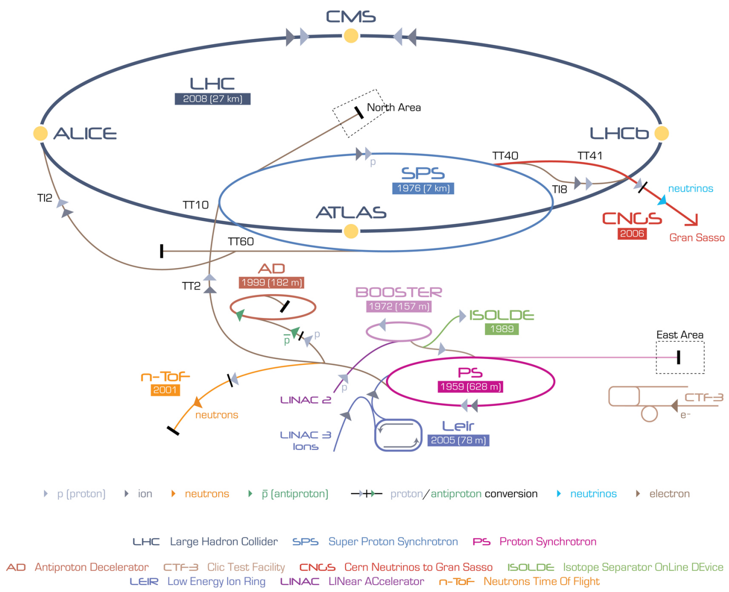

Figure 2.1: Schematic view of the CERN accelerators complex. The NA62 experiment is located in the North Area. This image is taken from [36].

The NA62 experiment is a fixed-target experiment and its main physics goal is to measure the branching ratio of the $K^+ \to \pi^+\nu\bar{\nu}$ decay [37]. In order to select $K^+ \to \pi^+\nu\bar{\nu}$ events, the NA62 detector aims to:

- identify incoming K^+ tracks;
- identify π^+ tracks coming from K^+ decays;
- to reject e^+ and μ^+ coming from other decay channels with a high efficiency;
- to reject additional photons coming manly from $\pi^0 \to \gamma\gamma$ decay where the π^0 is generated by $K^+ \to \pi^+\pi^0$ decay (the branching ratio of $K^+ \to \pi^+\pi^0$ decay is $\sim 20\%$ [3]).

The main elements for the detection of K^+ decay products cover a length of 170 m, starting about 100 m downstream of the beryllium target. The reference frame of the NA62 is a Cartesian reference frame. The origin of the system (x, y and $z = 0$) is the point located on the upstream surface of the beryllium target (z =0), where the x =0 and y =0 are set in the middle of this surface. The z is along the beam line, the y axis is orthogonal to the z axis going from bottom to top and the x axis is set in order to build a right-handed reference frame. The fiducial volume where the useful kaon decays are detected is in the first 60 m of the 117 m long evacuated tank. The main experimental elements placed along the NA62 nominal beam-axis are:

- the CEDAR, a Cherenkov detector that identifies the K^+ component in the beam (Section 2.3.1);
- the GigaTracker (GTK), a spectrometer consisting of three silicon pixel stations that measure the coordinates and momentum of the individual beam particle (Section 2.2.1);
- the CHANTI, a detector composed of six stations placed after the third station of GTK aiming to reduce the background due to the inelastic interactions of the beam with the GTK stations (Section 2.2.3);

- the Large Angle Veto (LAV) stations, a set of twelve photon-veto detectors aiming to detect photons within an angular region between 8.5 mrad and 50 mrad (Section 2.4.1);
- the STRAW, a spectrometer that detects and measures the coordinates and momentum of charged particles originated from the decay region (Section 2.2.2);
- the Ring Imaging CHerenkov (RICH), a particle identification detector that aims to separate π^+ from μ^+ between 15 GeV/c and 35 GeV/c (Section 2.3.2);
- the CHOD, a charged hodoscope that is important in the detection of multi-charged events (Section 2.3.3);
- the IRC calorimeter, a small angle photon and charged particle veto that covers an angular region up to 1 mrad (Section 2.4.3);
- the Liquid Krypton (LKr) calorimeter, an electromagnetic calorimeter that provides a photon-veto together with the LAV stations, covering an angular region between 1 mrad and 8.5 mrad (Section 2.4.2);
- the Muon Veto system(MUV), a system composed by three detectors: the MUV1 and MUV2 act as hadronic calorimeters that measure the deposit of energies and the shower shape of incident particles; the MUV3 consists of 140 scintillators with a time resolution $\sim$ 500 ps and it is used as a fast muon veto in the lowest trigger level (L0) (Section 2.5);
- the SAC calorimeter, a small angle photon-veto, placed downstream the MUV3, that detects photon emitted with angles approaching zero with respect to the kaon flight direction (Section 2.4.4).

The longitudinal position and the size along the NA62 nominal beam axis of all NA62 subdetectors are listed in Table 2.1 [38].

Subdetector	**Longitudianal position along the nominal beam axis[m]**	**Size along nominal beam axis[m]**
CEDAR	~ 69.79	~ 5
GTK station 1	~ 79.60	~ 0.16
GTK station 2	~ 92.80	~ 0.16
GTK station 3	~ 102.40	~ 0.03
CHANTI 1	~ 102.45	~ 0.03
CHANTI 2	~ 102.51	~ 0.03
CHANTI 3	~ 102.63	~ 0.03
CHANTI 4	~ 102.86	~ 0.03
CHANTI 5	~ 103.32	~ 0.03
CHANTI 6	~ 104.24	~ 0.03
LAV1	~ 122.20	~ 0.6
LAV2	~ 129.80	~ 0.6
LAV3	~ 137.40	~ 0.6
LAV4	~ 145.05	~ 0.6
LAV5	~ 152.66	~ 0.6
LAV6	~ 166.17	~ 0.6
LAV7	~ 173.68	~ 0.6
LAV8	~ 181.19	~ 0.6
STRAW 1	~ 183.60	~ 0.1
LAV9	~ 193.39	~ 0.6
STRAW 2	~ 193.87	~ 0.1
LAV10	~ 203.91	~ 0.6
STRAW 3	~ 204.55	~ 0.1
LAV11	~ 218.53	~ 0.6
STRAW 4	~ 218.98	~ 0.1
RICH	~ 219.60	~ 17
LAV12	~ 238.78	~ 0.6
CHOD	~ 2390.2	~ 0.02
IRC	~ 239.70	~ 0.09
LKr	~ 241.49	~ 0.40
MUV1	~ 244.34	~ 0.92
MUV2	~ 245.29	~ 0.85
MUV3	~ 246.85	~ 0.05
SAC	~ 261.21	~ 0.21

Table 2.1: NA62 subdetectors longitudinal positions and sizes along the nominal beam axis [38].

The detector has a cylindrical geometry around the beam axis and it can be divided into four sub-systems: the tracking system (Section 2.2), the particle identification system (Section 2.3), the photon veto system (Section 2.4) and the muon veto system (Section 2.5). A description of the beam line is given in Section 2.1.

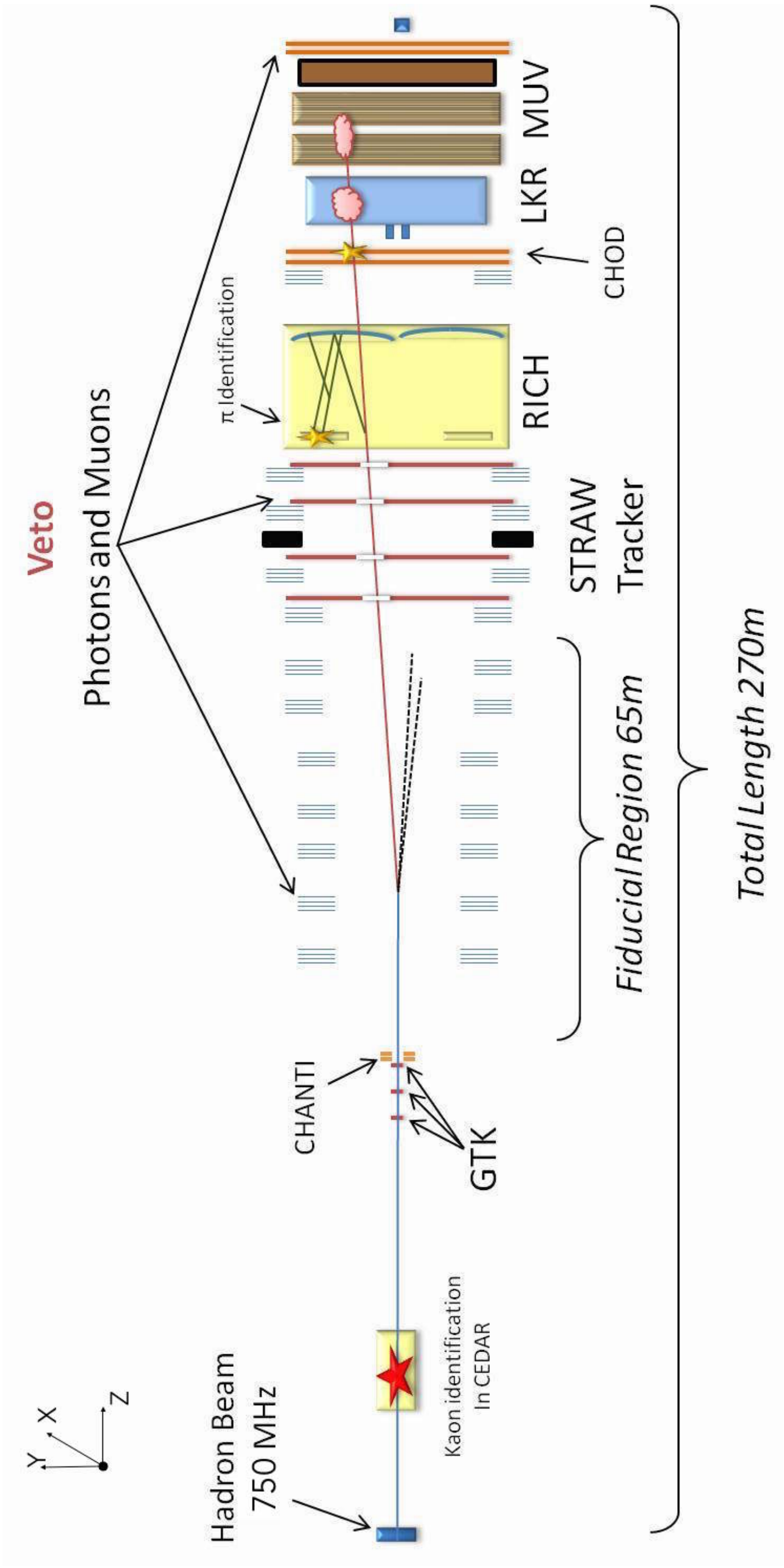

Figure 2.2: Schematic view of the NA62 experiment showing the main sub-detectors [39].

2.1 The beam line

Protons from the SPS at 400 GeV/c impinge on a 400 mm long, 2 mm diameter beryllium target producing a secondary charged beam. At the entrance of the fiducial volume the instantaneous rates of K^+, π^+, p^+, e^+ and μ^+ are 45 MHz, 525 MHz, 173 MHz, ~ 0.3 MHz and ~ 6 MHz, respectively [5], with an uncertainty of $\sim$10%. A secondary positive kaon beam of 75 GeV/c is selected by passing the beam through an achromat consisting of four dipole magnets (see Figure 2.3) [5]. For a kaon of 75 GeV/c the decay length is about 600m and it leads to a 10% fraction of kaon decays in an experimental fiducial volume of 60 m. After the beryllium target a system of quadrupole magnets focuses the charged particles towards a beam dump element represented by a momentum-defining slit. The magnet system is composed of TAX1 and TAX2 ("Target Attenuator eXperimental areas") that are enclosed in an achromat composed of four dipole magnets. Each TAX is made of 1.6 m of copper and iron (along the beam axis) that selects the particles with the correct charge and momentum through slits. The width of the slits determines the momentum spread of the particles. By closing one slit, one polarity can be selected to study K^+ or K^- separately. Additional quadrupoles focus the beam towards two collimator and align the beam on the axis of the Cherenkov differential counter that has to tag the kaon (the CEDAR).

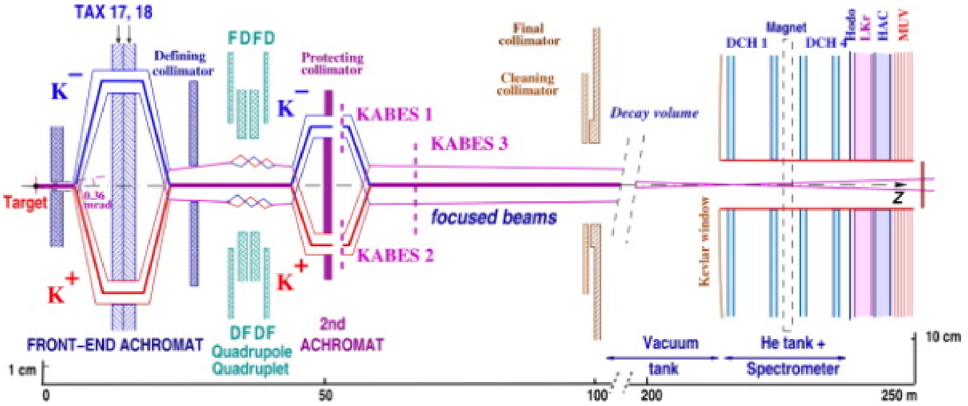

Figure 2.3: The beam line and the NA62 detector [40].

The upstream detectors are exposed to a high particle rate (750 MHz) that is ~ 17 times the rate due to the kaon component of the beam (45 MHz). Muons from pion and kaon decays represent an important contribution to the particle flux to which the detectors are exposed. Some NA62 beam properties are summarized in Table 2.2 [5].

SPS proton rate on target		1.1×10^{12} Hz
Fluxes at production	p	171 MHz
	K^+	53 MHz
	π^+	532 MHz
Fluxes at the beginning of the fiducial region	p	173 MHz
	K^+	45 MHz
	π^+	525 MHz
	e^+	0.3 MHz
	$\mu+$	6 MHz
Mean K^+ momentum		75 GeV/c
Momentum band r.m.s $\Delta p/p$		1%
2 r.m.s Beam size		x = ± 27.5 mm
		y = ± 11.4 mm
Fiducial volume length		60 m
K^+ decay length	$\beta\gamma c\tau$	563.9 m
K^+ decay fraction in the fiducial volume		0.10
K^+ decays in the fiducial volume per year		4.5×10^{12}

Table 2.2: NA62 beam properties. In the μ^+ flux the halo is not taken into account [5].

2.2 The tracking system

The tracking system is composed of two detectors: the GigaTracker and the STRAW spectrometer.

2.2.1 GigaTracker

The GigaTracker (GTK) is a spectrometer that has to provide a precise measurement of the momentum, time and direction of the incoming kaon beam at nominal beam momentum (75 GeV/c). The detector is formed by three hybrid silicon pixel stations placed along the beam line upstream the 60m-long fiducial region

(105m< $z_{FiducialRegion}$ <165m) between four magnets as shown in Figure 2.4. More precisely, each station is placed at the following z-coordinates along the nominal beam-axis:

- first GTK station: $z \sim 79.6$ m;
- second GTK station: $z \sim 92.8$ m;
- third GTK station: $z \sim 102.4$ m.

A charged particle passing through a magnetic field is bent and its path depends on its momentum. The GTK is fundamental for the selection of $K^+ \rightarrow \pi^+ \nu \bar{\nu}$ decay and the background reduction is achieved by kinematic constrains based on the missing mass variable:

$$m^2_{miss} \sim m^2_K \left(1 - \frac{|P_\pi|}{|P_K|}\right) + m^2_\pi \left(1 - \frac{|P_\pi|}{|P_K|}\right) - |P_K|\,|P_\pi|\,\theta^2_{\pi K}, \tag{2.1}$$

where m_K, m_π are the kaon and pion mass,respectively, P_K, P_π are the fourth-momentum of the kaon and pion, respectively, and $\theta_{\pi K}$ is the angle between the pion flight direction and the kaon flight direction. The quantity P_K is entirely measured by GTK while the angle, $\theta_{\pi K}$, is obtained from the measure of the kaon flight-direction given by the GTK and of the pion flight-direction coming from kaon decays, which is measured with the downstream spectrometer, the STRAW detector (Section 2.2.2), which also provides the measurement of P_π.

The GTK detector has to sustain a high beam rate of 0.75 GHz that is not uniform having a peak value over 1.4 MHz/mm^2. The GTK has to measure the momentum with a relative resolution of $\sigma(p)/p \sim 0.2\%$ and the direction with a resolution of 16 μrad per coordinate. The time resolution on a single track using the three stations must be 150 ps in order to minimize a wrong association of the beam particle to the decay product reconstructed in the downstream sub-detectors.

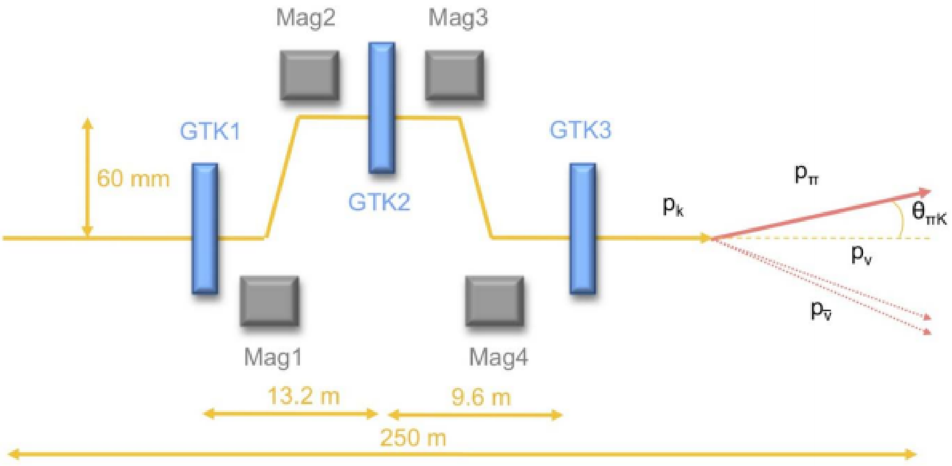

Figure 2.4: Layout of the GigaTracker stations [5].

2.2.2 STRAW spectrometer

The STRAW tracker is designed to measure the direction and the momentum of the secondary charged particles originating in the decay region. It consists of four drift chambers with a high aperture dipole placed in the middle as shown in Figure 2.5. The detector is placed in vacuum in order to reduce the multiple scattering effects. The z-positions of the chambers along the nominal beam-axis are:

- first chamber: $z \sim 183$ m;
- second chamber: $z \sim 194$ m;
- third chamber: $z \sim 204$ m;
- fourth chamber: $z \sim 219$ m.

Each chamber is equipped with 1792 straw tubes arranged in four "views" in the xy plane, 0°(X), 90°(Y), -45°(U) and +45°(V). The spectrometer is formed mainly by an ultra-light straw tube 2.1 m long with a diameter of 9.8 mm. Each chamber layer contains 112 straws and the distance between the straws in one layer is 17.6 mm. After the second chamber there is a magnet that is 1.3 m long and has an integrated field of 0.9 T m. The STRAW magnetic spectrometer must have a spatial resolution of 130 μm per coordinate and 80 μm per space point. The straws near the beam-axis operate in a high rate environment, of up to 40 kHz/cm and up to 500 kHz/Straw.

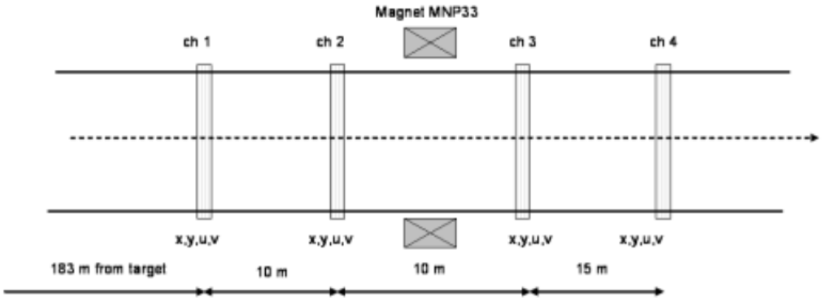

Figure 2.5: Schematic view of the magnetic spectrometer [5].

2.2.3 CHANTI

The CHANTI detector [41] is placed after the third station of the GTK ($z \sim 103$m) in order to reduce the background due to the inelastic interactions of the beam with the collimator and the GTK stations and also to tag the muon halo close to the beam coming from $\pi \rightarrow \mu\nu$ (BR∼99% [3]) and $K \rightarrow \pi\mu$ (BR∼63% [3]) decays. For instance, if a beam particle interacts inelastically with the third station of the GTK producing pions or other particles at large angle, these particles can reach the straw tracker and mimic a kaon decay in the fiducial region. If only this particle is detected, the event can appear as a signal event, i.e. one single π^+ in the final state. The CHANTI thus has to identify inelastic interactions in the GTK and to tag particles with higher angle with respect to the beam. It consists of six stations of scintillator bars around the beam placed in a vacuum vessel together with the GTK3 station. The scattered particles are detected by the CHANTI stations (blue bars) as shown in Figure 2.6 [5]. The CHANTI is supposed to veto 2 MHz of events coming from inelastic interactions and from muon halo.

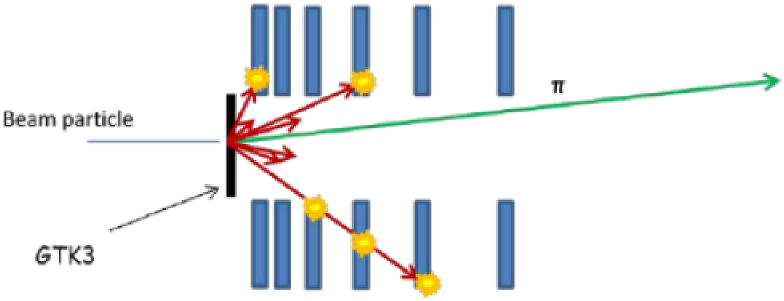

Figure 2.6: Schematic view of the CHANTI (blue bars), while detecting particle after inelastic interaction in the GTK3 [5].

2.3 The particle identification system

The particle identification system is composed of a detector for positive identification of the incoming K^+, the CEDAR, and a detector for the identification of the outgoing π^+, μ^+, e^- and e^+, the Ring Imaging CHerenkov.

2.3.1 CEDAR

The beam at the upstream detectors is mainly made up of pions ($\sim$ 70%) and protons ($\sim$ 20%), with only 6% of kaons. The identification of the minor kaon component is achieved by putting a Cherenkov Detector with Achromatic Ring focus, the CEDAR, in the incoming secondary beam. The design of the detector is based on a CERN West Area CEDAR detector used during the 1970s to discriminate pions, protons and kaon from the beam coming from the CERN SPS [42]. The CEDAR gas volume and optics are suitable for use in NA62, but the original photodetectors and read-out electronics are not suitable to sustain the particle rate in NA62 beam line. Therefore a new photodetection and read-out system is developed to meet the NA62 requirements, constituting the KTAG (Kaon TAGger) detector.

The detector has to identify particles with a specific mass while being blind to the Cherenkov light coming from particles with different mass. It is able to separate kaons and pions up to 150 GeV/c. The CEDAR is a $\sim$ 7 m long vessel filled with N_2

gas at room temperature with a pressure that can vary from near-vacuum ($\sim 10^{-1}$ bar) to 5 bar [43]. A charged particle passing through the gas with a momentum over the Cherenkov threshold produces Cherenkov light.

2.3.1.1 The Cherenkov effect

When a charged particle crosses a medium, which has a refractive index n, with a velocity β larger than the speed of the light in that medium (c/n), it emits a radiation at angle θ_c with respect to the particle trajectory, generating a Cherenkov-light cone in the medium such that:

$$\cos\theta_{\mathrm{c}} = \frac{1}{n\beta}. \tag{2.2}$$

Putting $\theta_{\mathrm{c}} = 0$ the threshold velocity β_t under which no Cherenkov light is emitted by the charged particle is obtained:

$$\beta_t = 1/n, \tag{2.3}$$

while putting β =1 the maximum Cherenkov angle θ_c is obtained:

$$\begin{aligned} \cos\theta_{\mathrm{c}}^{\max} &= \frac{1}{n}, \\ \sin\theta_{\mathrm{c}}^{\max} &= \frac{\sqrt{n^2-1}}{n}, \\ \tan\theta_{\mathrm{c}}^{\max} &= \sqrt{n^2-1}. \end{aligned} \tag{2.4}$$

If the particle has mass m, its momentum is:

$$p = m\gamma\beta = \frac{m\beta}{\sqrt{1-\beta^2}}. \tag{2.5}$$

The momentum threshold for a particle of a mass m to create a Cherenkov cone is given by:

$$p_t = \frac{m}{\sqrt{n^2-1}}. \tag{2.6}$$

The number of photons N emitted through a radiator thickness x depends on the wavelength λ (or energy E), the index of refraction and the Cherenkov angle (assuming a single charged particle):

$$\frac{d^2N}{dEdx} = \frac{2\pi\alpha}{hc}\sin^2\theta_\mathrm{c} \simeq 370\sin^2\theta_\mathrm{c}\ \mathrm{eV^{-1}cm^{-1}}, \tag{2.7}$$

which is the Frank-Tamm equation [44, 45]. It can be also written as:

$$\frac{d^2N}{d\lambda dx} = \frac{2\pi}{\lambda^2}\sin^2\theta_\mathrm{c}. \tag{2.8}$$

The Cherenkov light produced by a charged particle in the CEDAR gas tank is reflected by a spherical mirror, placed at the end of the vessel, with 300 mm diameter and a 100 mm aperture in the centre to allow the passage of the beam. The light is reflected onto a diaphragm with an adjustable aperture width placed at the entrance of the vessel in order to select rings of certain radius, Figure 2.7.

Given a particle momentum and a gas refractive index n, the angle of the emitted Cherenkov light is a function only of the mass of the traversing particle. The chromatic dispersion of the gas also gives a dependence of the angle on the wavelength of the light. There is a chromatic corrector lens placed between the diaphragm and the mirror (see Figure 2.7) aiming to match the chromatic dispersion curve of the gas; it ensures that light of different wavelengths arrives at the same radius on the diaphragm plane, avoiding therefore the detection of light from unwanted particle since it hits the diaphragm plane in a different radius, not passing through the aperture.

The light detection is performed by the KTAG (Kaon TAGger). There are 384 photomultipliers mounted on 8 light boxes. The KTAG has to cope with the expected 45 MHz kaon rate. The system of CEDAR and KTAG has an efficiency in kaon tagging above 95% with a kaon time resolution less than 100 ps in order sustain the total beam particle rate of 750 MHz.

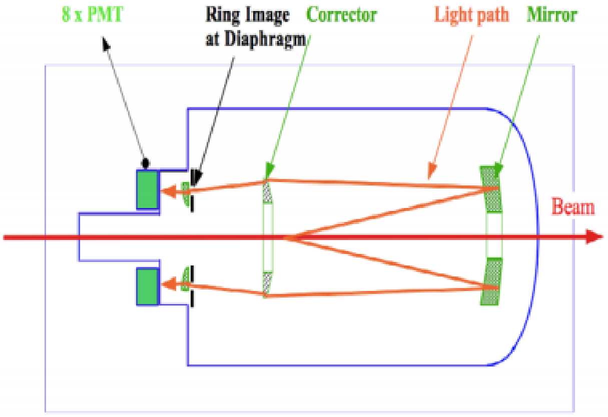

Figure 2.7: Schematic layout of the SPS CEDAR from [5].

2.3.2 RICH

The Ring Imaging CHerenkov (RICH) is the particle identification detector for the kaon decay products [46]. It aims to separate π^+ from μ^+ between 15 GeV/c and 35 GeV/c momentum providing a muon suppression factor of at least 10^{-2}. It exploits the emission of the light cones due to the Cherenkov effect (Section 2.3.1.1).

In the RICH detector the Cherenkov cone is reflected back by a spherical mirror on a photon detector placed at the focal plane of the mirror (for the description of the components of the RICH detector see Section 2.3.2.1). If the particle trajectory is orthogonal to the focal plane, the cone image reflected by the spherical mirror is a ring with a radius

$$r_{ring} = f \tan\theta_c \simeq f\theta_c, \tag{2.9}$$

where f is the focal length of the spherical mirror (i.e. half of its curvature radius). The approximation is good assuming small Cherenkov angles (this is the case in the gas radiator). Other important relations are (for small Cherenkov angles):

$$\begin{aligned}
r_{ring} &= f\frac{\sqrt{\tan^2\theta_c^{max} - \frac{m^2}{p^2}}}{\sqrt{1+\frac{m^2}{p^2}}} \simeq f\sqrt{(\theta_c^{max})^2 - \frac{m^2}{p^2}}, \\
r_{max} &= f\tan\theta_c^{max} = f\sqrt{n^2-1}, \\
r_{ring} &\simeq \sqrt{r_{max}^2 - f^2\frac{m^2}{p^2}},
\end{aligned} \tag{2.10}$$

where p is the particle momentum and m is the particle mass. Particles with parallel trajectories form concentric rings. If a particle trajectory has an angle α with respect to the axis orthogonal to the detector focal plane, the centre of the ring is shifted by a distance d given by

$$d = f\tan\alpha \tag{2.11}$$

in the same direction of the particle trajectory inclination and the ring is slightly distorted to an ellipse of minimum and maximum semiaxes:

$$a_{min} = f\tan\theta_c; \quad a_{max} = f\tan\theta_c/\cos\alpha. \tag{2.12}$$

2.3.2.1 The detector: basic design and characteristics

The choice of the Neon gas at atmospheric pressure as a Cherenkov radiating medium is due to the requirement to separate pions from muons in the momentum region between 15 GeV/c and 35 GeV/c, providing a muon suppression factor of at least 10^{-2}. In order to achieve this requirement, the Cherenkov momentum-threshold must be roughly 20% smaller than the minimum of the momentum range, i.e. $\sim$ 12.5 GeV/c (a sufficient number of hits is required to reconstruct the Cherenkov ring). This leads to a refractive index equal to $(n-1) = 62 \times 10^{-6}$, which is the value of the Neon gas at atmospheric pressure.

The measurement of the crossing-time of a particle has to be performed with a resolution of $\sim$ 100 ps or better. This leads to the choice to use fast single anode photomultilpliers, with a small dimension of the PMTs (for the PMT dimension see Section 2.3.2.5) and a compact packaging.

The Frank-Tamm equation in 2.8 gives the number of emitted photons through a radiator thickness per unit of photon energy as a function of the Cherenkov angle. The actual number of photoelectrons $N_{p.e.}$, i.e. the number of electrons produced by a photon impinging on the PMT-photocathode, is obtained by the convolution of several terms; in particular, starting from the Frank-Tamm equation, the reflectivity of the mirrors , the spectral response of the PMT, the transparency of the gas and of any other medium in front of the PMT, the geometrical acceptance of the PMTs, the length L of the radiator and the emitting Cherenkov angle have to be considered. All these quantities depend on the photon energy, except for the length of the radiator and the emitting Cherenkov angle. Hence a quality factor N_0 is defined to describe the performance of the RICH detector:

$$N_{p.e.} = N_0 L \sin^2 \theta_C. \tag{2.13}$$

A good RICH detector has the quality factor N_0 roughly equal to 100 cm^{-1} [3]. In this case the probability to produce more than one photoelectron in the same PMT is not negligible ($\sim$10%), thus it is better to use the number of fired PMTs, N_{hit}, that is smaller than $N_{p.e.}$. The NA62 RICH vessel, i.e. the gas container, is 17 m long in the beam direction: this number is a good compromise between the quality factor and the space available along the beam line between the last straw and the Liquid Krypton calorimeter: a longer detector is preferable because it provides a larger number of hits.

2.3.2.2 The RICH vessel

The NA62 RICH vessel is placed downstream the fourth STRAW chamber. It has to contain the Neon gas with no leakage, operating at atmospheric pressure. The gas density must remain constant (within 1%) over time dictated by the tolerance on the variation of the refractive index [5]. A schematic view of the vessel is shown in Figure 2.8. The Cherenkov light emitted in the gas system is reflected back by a system of hexagonal spherical mirrors into two different regions (flanges) upstream the gas tank, one on the right of the beam pipe and the other one on the left. They are placed outside the gammas acceptance (gammas from the kaon decay products) and placed in the transverse plane, with the centres in $y = 0$ according to the NA62 reference frame. The Cherenkov light is reflected into two different regions in order to avoid the shadow of the beam pipe, that would lead to a loss of Cherenkov photons. Each of the regions has a circular shape with a 780 mm diameter (Figure 2.9). The PMTs are lodged in the two flanges. The RICH vessel consists of several parts: each part has a different dimension. It has indeed a decreasing diameter, between 4 m at the entrance and 3.4 m at the end to avoid hindening the reflected Cherenkov light.

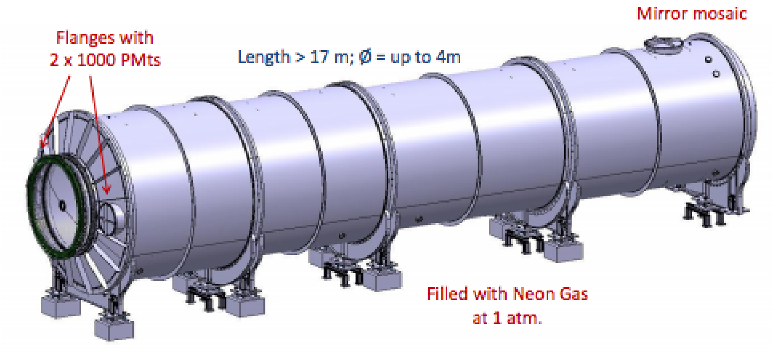

Figure 2.8: Schematic view of the RICH detector [46].

Figure 2.9: The RICH vessel installed in the NA62 cavern (left). The beam pipe seen from the inside of the RICH vessel where the entrance window and the PMT flanges are well visible (right) [47].

The diameter of the last downstream part is due to the size of the mirror support panel.

2.3.2.3 The gas system

The NA62 RICH radiator-gas has to satisfy five different requirements to achieve a good performance of the detector:

- appropriate refractive index at atmospheric pressure,
- good light transparency in the visible and near UV region (as the peak of the Cherenkov light emission is in the near UV with a long tail in the visible region),
- low chromatic dispersion,
- low atomic weight, in order to minimize radiation length,
- non-flammable.

The Neon is the most appropriate choice: it has a suitable refractive index, a small chromatic dispersion and a low atomic mass.

The RICH operating wavelength range starts at 190 nm, due to the Cherenkov light spectrum, and its performance is not sensitive to impurities in the gas. The light absorption for trace pollutants of Oxygen and H_2O, for example, becomes noticeable only at wavelength below 190nm. However the presence of residual gases affects the refractive index, degrading the Cherenkov angle resolution if concentration variations occur at different times.

2.3.2.4 The mirrors system

A mosaic of spherical mirrors images the Cherenkov light cone into a ring on the focal plane of the mirrors. As already mentioned, in order to avoid a loss of Cherenkov photons by the absorption due to the beam pipe, the mirrors are divided into two different spherical surfaces, one with the centre of the curvature pointing toward the left and the other one toward the right of the beam pipe. The total reflective surface exceeds 6 m^2 and a matrix of 20 mirrors is used.

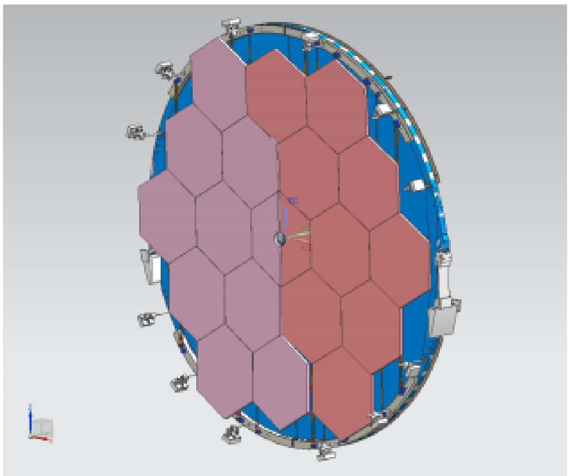

Figure 2.10: Design of the hexagonal spherical mirror of the RICH detector [46].

The NA62 RICH detector has spherical mirrors with a nominal curvature radius of 34 m and a focal length of 17 m. The 20 mirrors do not have all the same shape, in particular 18 mirrors have an hexagonal shape (35 cm side dimension) and 2 a semi-hexagonal shape as shown in Figure 2.10. The semi-hexagonal shaped mirrors are placed in the centre of the mosaic and they have a circular opening in the middle to accommodate the beam pipe. The mirrors have a thickness of 25 mm and they are coated with aluminium; a dielectric film is also added in order to protect the mirrors and to improve the reflectivity.

Each of the mosaic mirrors must satisfy three optical parameters:

- defining D_0 as the diameter of the smallest image of a point source placed in the centre of curvature which contains 95% of the light, each mirror is required to have a D_0 not larger than 4 mm;
- a radius of curvature within ± 20 cm of the nominal one;
- an average reflectivity, in the wavelength range between 195 nm and 650 nm, better than 90%.

The mounting of the mirrors downstream the vessel is shown in Figure 2.11.

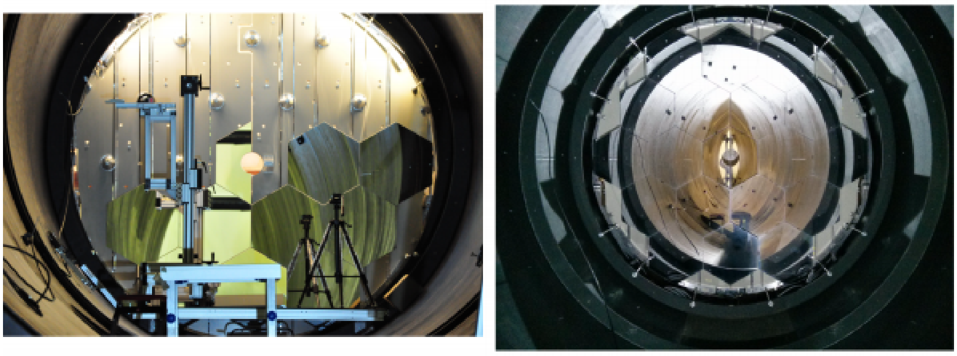

Figure 2.11: Some mirrors hung on the support in the lower part of the mosaic inside the RICH vessel (left); the completed mirror mosaic (right) [47].

In order to support the mirror mosaic, an aluminium honeycomb panel is placed in front of the downstream end-cap of the vessel. This panel, 50 mm thick, is divided into two halves and is designed to be stiff enough for the 400 kg load of the mirror mosaic, but at the same time as transparent as possible to gammas to be detected by the downstream Liquid Krypton (LKr) calorimeter.

Each mirror must be supported and adjustable for alignment. The mirrors are left free to rotate along the x and y axis.

2.3.2.5 Photon detection system

In order to have a good angular resolution of the detector, the granularity of the photon detection system has to be as small as possible. On the other hand, an increasing number of photo detectors would directly lead to a higher cost of the RICH detector. A reasonable compromise drives to the choice of 1952 PMTs in total. A simulation study has shown that they are quite enough to match the detector requirements. The single photo-sensor has diameter of 18 mm. They are mounted on the two different flanges: each flange is equipped with 976 PMTs, see Figure 2.12. The NA62 RICH PMTs must have a fast response and a small dimension. A group of 8 neighbouring PMTs defines a super-cell (SC): the RICH has in total 244 super-cells (the super-cells are useful for trigger purposes, see chapter 4).

Figure 2.12: On the left-hand side a schematic drawing of the NA62 RICH detector: the upstream section of the vessel shows a zoom on one of the two PMT flanges while the downstream section shows the mirror mosaic [47]. On the right-hand side, one of the two flanges with 976 PMTs mounted on it [47].

Each of the two flanges, 780 mm in diameter, consists of two parts both in aluminium: an inner part with 23 mm thickness divides the Neon gas from the air by means of 12.7 mm wide and 1 mm thick quartz windows. It also collects the incoming Cherenkov light through a Winston cone that is an hole with a shape of truncated paraboloid covered by a highly reflective Polyethylenterephthalat (trade name Mylar). The outer part holds the PMTs. A cylindrical hole, 16.5 mm wide and 10 mm high, is drilled in the aluminium flange for each PMT, followed by a 17.5 mm wide and 22 mm high hole for the HV divider. A 1 mm thick O-ring (with 17.5 mm outer and 13.5 mm inner diameter) is placed in front of the PMT (kept in place by a 2 mm thick gorge in the hole placed 0.5 mm above the end) and pressed against the quartz window to avoid external light to reach the PMT. A (5±1) mm thick O-ring (with the same outer and inner diameter of the 1 mm O-ring) is placed on the back of the PMT (after the end of the HV divider) to close the hole and avoid external light; this O-ring also guarantees a good thermal contact between the PMT and the aluminium flange and absorbs the tolerance in the PMT total length.

Concerning the front-end electronics, the signal output of the PMT has a roughly triangular shape with a rise time of 0.78 ns (on average) and a fall time about twice as long. At the nominal voltage (900 V), the gain is typically 1.5×10^6, with a charge output of ~ 240 fC, corresponding to a peak current of 200 μA and a negative peak voltage of 10 mV over 50 Ω. The front-end electronics are based on the NINO ASIC.

The 8-channel NINO ASIC [48, 49] is chosen as discriminator, because of its fast response. The PMT output is sent to a current amplifier, before reaching the NINO, in order to match the optimal NINO performance region. The NINO discriminator operates in time-over-threshold mode, its LVDS (Low Voltage Differential Signal) output signal is sent to 512-channels TEL62 [50] boards equipped with HPTDC (High Performance Time to Digital Convert) [51] chips. In order to increase the time performance a slewing correction in the analysis is necessary, thus both leading and trailing edge of the LVDS signal are recorded. Differences in the output height results in differences in the slope of the rise time: more the height is and more the steepness is. For this reason the threshold value of the signal amplitude is reached earlier in a higher signal than in a lower one, resulting in a global deterioration of the time resolution.

2.3.3 CHOD

The NA48 charged hodoscope (CHOD) detector [5] is placed downstream the RICH and upstream the Liquid Krypton calorimeter. The layout of the detector is shown in Figure 2.14. It consists of 128 detection channels reading the signals from two planes of 64 horizontal and vertical scintillator slabs. Each plane is divided in four quadrants with 16 counters each. The length of the slabs ranges from 60 cm to 121 cm and the width from 6.5 cm (close to the beam pipe) to 9.9 cm. The central hole has a radius of 10.8 cm because of the passage of the beam pipe. The scintillation light, produced by a charged particle passing through the slab, is collected at the edge of the slab from a Plexiglass fishtail shaped light guide connected to a photomultiplier. The passage of a charged particle through the detector is identified by the time matching between the hits of the two slabs of corresponding quadrants of the two planes. The two planes have a distance of ~ 30 cm between them; this distance allows to tag fake coincidences due to the back-splash from the LKr calorimeter surface according to the different timing of the two planes. The CHOD performs with a time resolution of 200 ps. A design for a new CHOD for the NA62 experiment is being developed in order to sustain the high hit rate (10 MHz) at which the scintillator slabs are exposed.

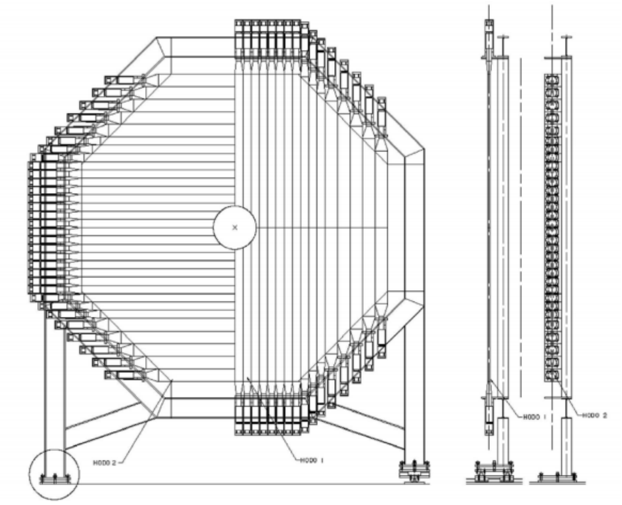

Figure 2.13: Sketch of the horizontal and vertical planes of the CHOD [5].

2.4 The photon veto system

The photon veto system aims to reject the dominant background to different signals (for example $K^+ \to \pi^+\nu\bar{\nu}$ or $K^+ \to \pi^+e^+e^-$). For instance, one of the main background for the $K^+ \to \pi^+e^+e^-$ signal to be rejected is the $K^+ \to \pi^+\pi^0$ decay (BR=20.7%), with an inefficiency for the rejection of π^0 of about 10^{-8}. It covers an acceptance region from 0 mrad up to 50 mrad in the polar angle with respect to the beam line. The acceptance region is split into three different angular regions with respect to the beam line, each with a different photon detector:

- the angular region between 8.5 mrad and 50 mrad is covered by the Large Angle Vetoes (LAV);
- the angular region between 1 mrad and 8.5 mrad is covered by the Liquid Krypton calorimeter (LKr);
- the angular region up to 1 mrad is covered by a Small Angle Calorimeter (SAC) and by the Inner Ring Calorimeter (IRC). Together they form the Small Angle Vetoes (SAV).

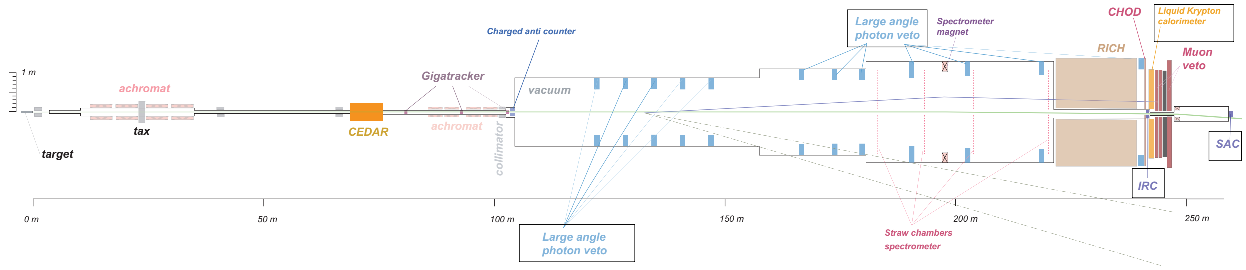

Figure 2.14: Sketch of the NA62 detector where the photon veto sub-detectors are underlined by black rectangles [5].

2.4.1 LAV

The LAV detector is composed of twelve stations placed between 120 m and 240 m along the z-axis in the NA62 reference frame (see Table 2.1). The first eleven stations are situated in the vacuum decay tube, while the last one is outside the vacuum tube. The diameter of the stations increases with the distance from the target on the z-axis.

The building blocks of all twelve stations are lead glass blocks from the OPAL electromagnetic calorimeter barrel [52]. The blocks are mounted radially inside a cylindrical station in an inward-facing ring called layer (see Figure 2.15). Multi-ring layers are constructed in each station. A photon impinging on a lead block creates an electromagnetic shower. Charged particles of the shower will create Cherenkov light in the block. Each block is read out by a photomultiplier placed at the back side of the block, Figure 2.15.

The LAV photon detection inefficiency has been measured at the Beam Test Facility at the Laboratori Nazionali di Fisica Nucleare e Subnucleare in Frascati and it is $(1.2^{+0.9}_{-0.8})\times10^{-4}$ at 200 MeV and $(1.1^{+1.8}_{-0.7})\times10^{-5}$ at 500 MeV [53].

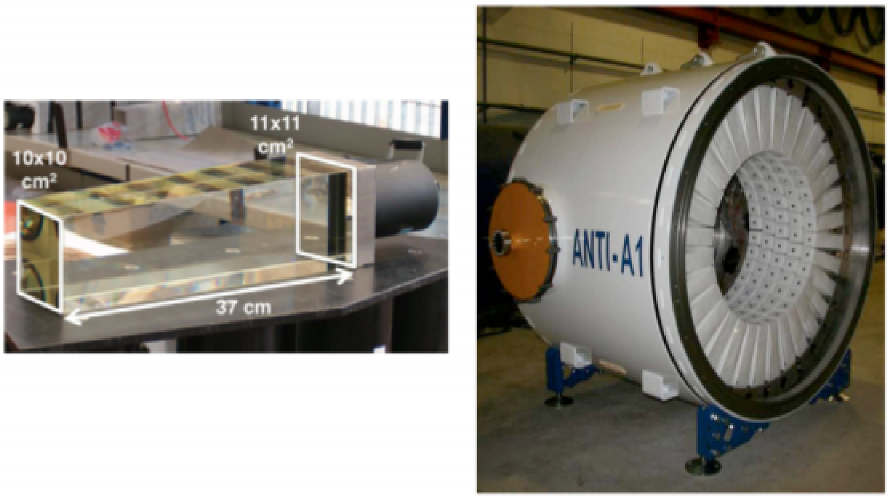

Figure 2.15: A lead glass block from the OPAL calorimeter (left). The first LAV station with 32 × 5 OPAL lead glass [5].

2.4.2 The Liquid Krypton calorimeter

The Liquid Krypton (LKr) detector is the same that has been used in the NA48 experiment, with a new readout. It is an homogeneous calorimeter. A photon or an electron passing through the active part of the detector creates an electromagnetic shower via either pair production or Bremsstrahlung process. The LKr calorimeter rejects photons in an angle between 1 mrad and 8.5 mrad with respect to the beam line. It is required to have a detection inefficiency better than 10^{-5} for energies larger than 35 GeV [5]. The shape of the detector is approximately octagonal in the xy plane and $\sim$ 127 cm long in the z direction, corresponding to 27 radiation length. The active part of the calorimeter is the liquefied Krypton noble gas and its choice is due to the good resolution, the absence of ageing problem and the short radiation length that allows a compact design along the longitudinal direction. A cryogenics system allows the LKr temperature to be constantly below the boiling temperature of the Kr (120 K). The calorimeter is enclosed in a cryostat consisting of an external aluminium vessel (4 mm thick) and an internal vacuum insulated steel container that contains 7 m^3 of liquid Krypton (Figure 2.16). The active volume of liquid Krypton is divided into 13 248 cells by 18 mm wide, 40 μm thick copper-beryllium ribbon at a distance of 1 cm from each other. The choice of this geometry is due to the necessity of the best accuracy in the measurement of the angle between the photon direction and the beam direction. The energy resolution of the LKr calorimeter is (all energies in GeV):

$$\frac{\sigma_E}{E} = \frac{0.031}{\sqrt{E}} \oplus \frac{0.09}{E} \oplus 0.0042. \tag{2.14}$$

The first term is due to the intrinsic fluctuations (Poisson) of the energy deposition, the second term comes from the instrumental noise and the constant term is due to the accuracy of the calibration between the reconstructed energy of the shower and the real energy deposition in the calorimeter. The photon energy in the LKr calorimeter ranges from $\sim$ 1 GeV up to $\sim$ 6 GeV [5].

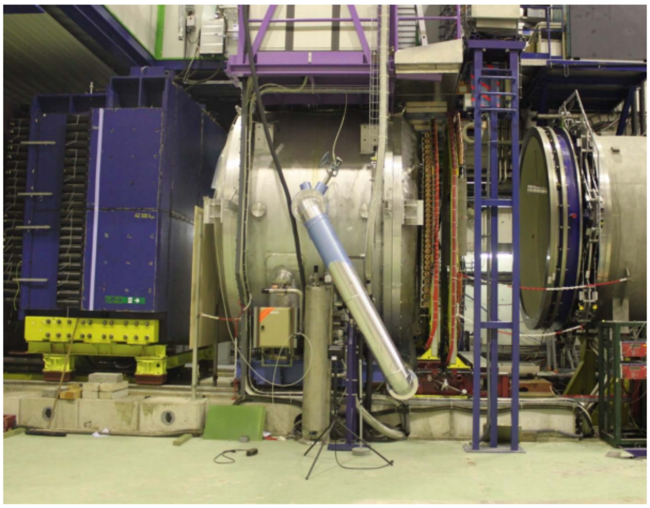

Figure 2.16: The LKr calorimeter [5].

2.4.3 IRC

The IRC calorimeter is located in front of the LKr and with the SAC calorimeter it has to detect photons emitted with angles approaching zero with respect to the kaon flight direction. Its active volume is placed as close as possible around the non decayed kaon beam and yet at sufficient large radius such that it is not subjected to extremely high rates due to the beam halo. It has to detect the photons travelling towards the inactive annular central region of the LKr around the beam pipe. It has a cylindrical geometry and it is made of two active regions, the first with 25 layers of lead and scintillators while the second one with 45 layers, for a total of 70 layers.

The outer radius is centred on the z-axis of the experiment while the inner radius is centred on the beam axis at a offset of $+1$ cm in the x-axis. The detector does not have a rotational symmetry around its axis. The front half of the detector has an inner and outer radii of 60 mm and 145 mm respectively, while the second half has an inner and outer radii of 61 mm and 145 mm respectively. The layout of the IRC is shown in Figure 2.17.

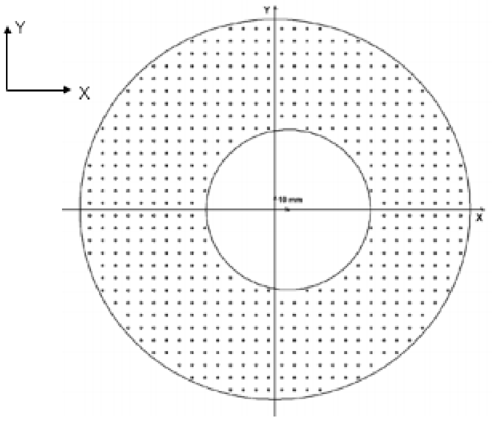

Figure 2.17: Distribution of the fibre holes of the IRC in the frontal view of the lead layer [5].

2.4.4 SAC

The SAC calorimeter is the last detector in the longitudinal order along the beam line. The SAC prototype is shown in Figure 2.18. It covers an area of 205 × 205 mm^2 centred on the axis. The SAC covers the region not covered by the IRC and the LKr. A sweeping magnet is placed upstream the SAC in order to deflect the charge component of the beam and to detect the remaining undeflected photons. The SAC is made of 70 lead plates of 1.5 mm thick with 1.5 mm plastic scintillator in between, for a total of 21 cm. The incoming photon interacts with the lead and develops an electromagnetic shower. The charged products of the shower produce scintillation light inside the plastic material. The light is taken out by wavelengths shifting fibres (WLS), passing through the plastic scintillator.

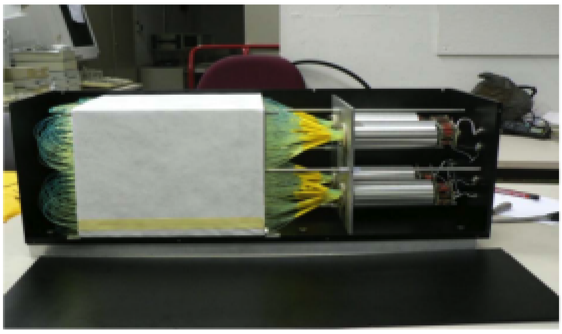

Figure 2.18: The SAC prototype [5].

2.5 The muon veto system

The muon veto system (MUV) consists of three distinct parts called MUV1, MUV2, MUV3 downstream the LKr, Figure 2.19.

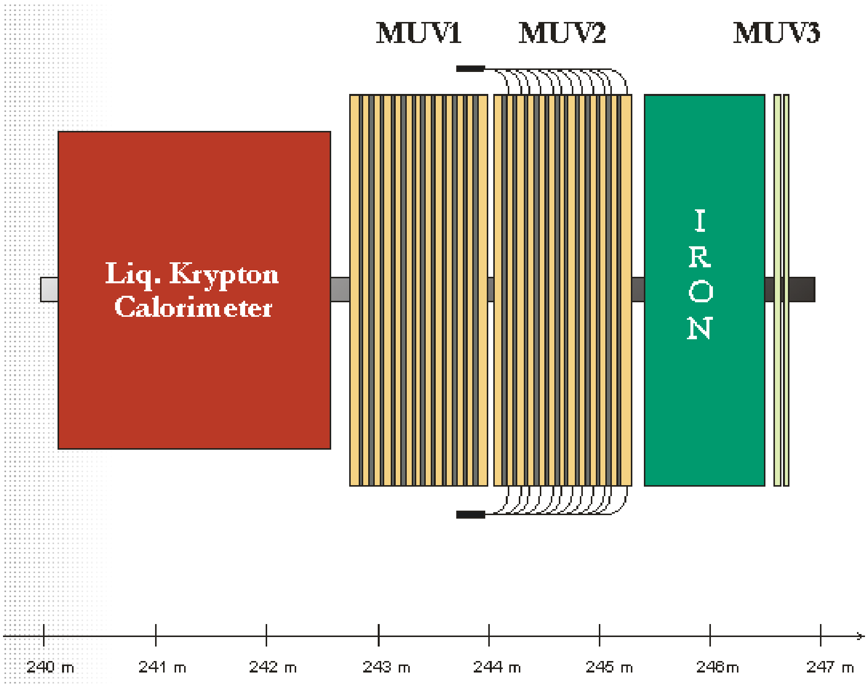

Figure 2.19: MUVs position along the NA62 beam line [5].

They are essential in reducing the background to different signals (for example $K^+ \to \pi^+ \nu \bar{\nu}$ or $K^+ \to \pi^+ e^+ e^-$) due to the kaon decays with muons in the final state, in particular the background coming from the most frequent kaon decay $K^+ \to \mu^+ \nu_\mu$.

2.5.1 MUV1-2

The MUV1 and MUV2 are two hadronic calorimeters that measure the deposit of energies and the shower shapes of incident particles. They are classic iron-scintillator sampling calorimeters with 24 (MUV1) and 22 (MUV2) layers of scintillator strips alternately oriented in the horizontal and vertical directions. The MUV1 steel layers have dimensions of $(2700 \times 2600 \times 25)\text{mm}^3$ with a central hole of 212 mm for the passage of the beam particles. The MUV2 steel layers have similar dimension of $(2600 \times 2600 \times 25)\text{mm}^3$ with the same central hole diameter. Each MUV1 scintillator layer contains a total of 48 strips of about 6 cm width for a total of $48 \times 24 = 1152$ strips while each MUV2 scintillator layer has 44 strips of about 11 cm width for a total of $48 \times 22 = 1056$ strips.

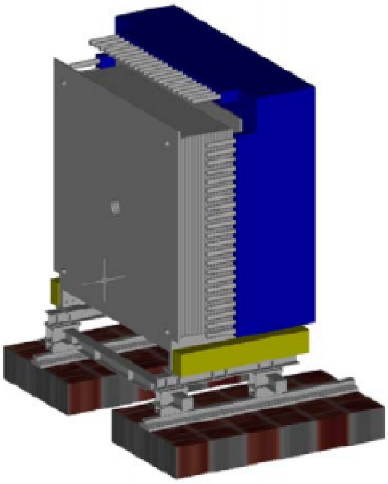

Figure 2.20: View of the MUV1 (grey) and MUV2 (blue) modules [5].

2.5.2 MUV3

The MUV3 is the third station of the muon veto system placed after the previous two stations and an iron wall of 80 cm depth that constitutes an additional muon filter. It consists of 140 large outer scintillator tiles of 22×22 cm^2 transverse area and 5 mm thick and 8 small inner tiles. A central beam hole is present for the passage of the beam particles. The light produced by a charged particle passing through the detector is collected about 20 cm downstream by photomultipliers. Each tile is read out by 2 PMTs. The time resolution of the MUV3 has been measured during a technical run to be $\sigma_t = 500$ ps.

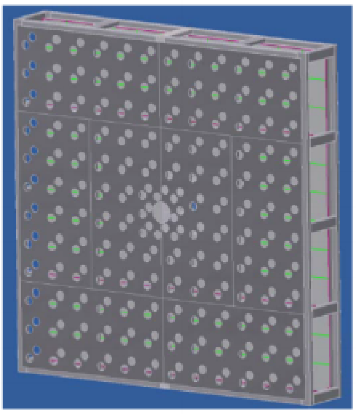

Figure 2.21: Layout of the MUV3 module [5].

2.6 The NA62 Trigger and Data Acquisition

A high particle flux ($\sim$ 10 MHz) demands a highly selective trigger and data acquisition (TDAQ) system. Figure 2.22 shows a schematic view of the trigger chain and data acquisition. The NA62 trigger is based on a multi-level trigger: a hardware lowest-level trigger (L0) and a software high-level triggers (L1 and L2) implemented on dedicated PCs.

2.6.1 The NA62 Trigger architecture

The NA62 trigger is based on the signal coming from charged particle, from the energy released in the calorimeter, and on the veto system. In the presence of a candidate signal event, for example a $K^+ \to \pi^+ e^+ e^-$ event, the sub-detectors, involved in the L0 trigger, generate a L0 trigger primitives through a Field Programmable Gate Array (FPGA). The L0 trigger primitives are managed by the L0 Trigger Processor (L0TP) which combines all the primitives from each sub-detector for a single event in order to make a final L0 trigger decision. During the elaboration of the L0 trigger

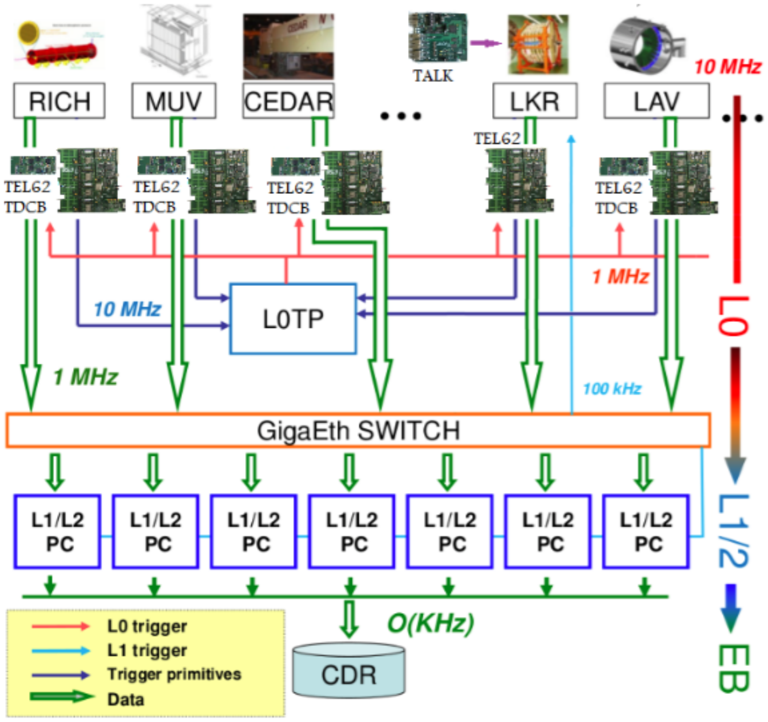

Figure 2.22: Trigger and Data acquisition overview [5].

decision, data from each sub-detector are stored in circular buffers for a time up to a defined maximum L0 trigger latency. When the L0 trigger decision is delivered, the trigger system is required to process events stored in the buffer within a time-window (±150 ns) around the central trigger-time.

The L0 trigger has to reduce the input rate of 10 MHz to an output rate of 1 MHz, that is the data bandwidth available for event storage in the PC-farm. After the L0 request, data stored within a time-window (±150 ns) around the central trigger-time are extracted and sent to the PC-farm for the L1 and L2 trigger processing. The L1 and L2 stages have to reduce the input rate from the L0 trigger by a total factor 100, so at the end 10 kHz of events will be sent to the PC-merger and then they will be written on disk. The PC-merger is a PC that receives the accepted events from the PC-farm, generates files with all events of one burst and stores them on the local disk buffer. The sending to the CERN data centre is done later by cronjobs.

2.6.1.1 The hardware low-level L0 trigger

The hardware L0 trigger is implemented in the TEL62 boards. The TEL62 is the motherboard for trigger generation and data acquisition for the NA62 experiment. Each TEL62 contains four TDC Boards (TDCB) that are mezzanine daughter-cards for the TEL62 board. Each TDCB holds four High Performance Time to Digital Converter (HPTDC) as time digitizers. Each HPTDC provides 32 TDC channels, so that a total of 128 channels are contained on TDCB and 512 channels in total are provided on the TEL62 board. On each TEL62 board four PP-FPGAs (Pre-Processing FPGA) and one SL-FPGA (SyncLink FPGA) are installed.

There are two streams in the TEL62: the data stream and the trigger stream. In the data stream, data are stored from TDCB for up to 1 ms that is the maximum latency of the L0 trigger; the trigger stream produces pre-primitives in the four PP-FPGA and, by combining them, the L0 trigger primitive in the SL-FPGA.

Each sub-detector involved in the L0 trigger produces trigger primitives with a time-stamp and a fine-time that are essential for the time matching among the data stream coming from the all sub-detectors. The time matching is performed by the L0TP. The L0TP takes trigger primitives from the TEL62 boards and combines them, looking for coincident trigger primitives in the various detectors, to produce a L0 trigger. During the processing of the L0 trigger request by the L0TP, data are stored in buffers for a time decided by the L0 trigger latency. Any L0 trigger is then sent back to each TEL62 board and demands any data collected in the relevant time period (in the 2015 run for the RICH a window of ±150 ns around the time associated with the L0 trigger has been chosen).

The NA62 sub-detectors involved in the L0 trigger are the RICH, the CHOD, the MUV (in particular the fast muon veto MUV3), the LKr and the LAV. For instance, the L0 trigger for the main physics goal of NA62 experiment, the search for $K^+ \to \pi^+ \nu\bar{\nu}$ event, requires a single ring in the RICH and a single track in the CHOD, not more than one cluster in the LKr, an energy cluster released in the

MUV1-2 by hadron, and nothing in the MUV3 and nothing in the LAV stations. In this case the CHOD is used to positively tag a single charged particle downstream the beam line. A L0 trigger strategy for the selection of multi-track even is discussed in detail in Section 4.2. The track multiplicity in the CHOD is important to tag multi-track kaon decays (Section 4.2).

The RICH multiplicity, that is the number of PMTs fired, is useful to either reduce or to select multi-track events. The particle identification feature of the RICH for particles with $\beta \neq 1$ can not be used at this early trigger stage since it would require a correlation among sub-detectors that are spatially separated; in particular the knowledge of the particle momentum from the straw spectrometer would be fundamental for the particle identification.

The third station of the muon veto system, the MUV3, has to veto the high rate of muon tracks coming from the $K^+ \rightarrow \mu^+ \nu_\mu$ decays and from the muon halo component from kaon decaying upstream of the final collimator. The LKr calorimeter is needed to reject the background decay $K^+ \rightarrow \pi^+ \pi^0$ to the $K^+ \rightarrow \pi^+ \nu \bar{\nu}$ signal. The LAV stations will reduce the photon component emitted at large angles, in particular the photons from the $K^+ \rightarrow \pi^+ \pi^0$ decay. The data acquisition process is described in Section 2.6.2. Once the data has been collected they are sent to the software high-level trigger.

2.6.1.2 The software high-level L1 and L2 triggers

The L1 and L2 trigger algorithms are implemented within a software framework running on each PC of the PC-farm. The NA62 PC-farm contains in total 30 PCs. Both the L1 and L2 algorithms are implemented on the same PCs to avoid data transfers. Data coming from the sub-detector readout system are organized in Multi Event Packets (MEPs), that is a storage packet with a defined "MEP packing factor" of events. During the 2015 run the MEP factor was set to 4, it means that each PC of the PC-farm received one MEP containing raw data of 4 events. After the PC-farm software has checked the data quality of the content of the MEP, each event data is analysed by the L1 trigger algorithm. Each sub-detector involved in the L1 trigger has a software algorithm able to do a partial reconstruction of the raw data from the TEL62 and to apply the L1 trigger cut for the signal selection. A L1 trigger strategy for the selection of multi-track events with electron identification using the RICH detector is described in chapters 4 and 5. The implementation of the RICH software L1 algorithm on the PC-farm is described in chapter 6.

The L1 trigger has to reduce the input event rate by a factor 10, to achieve an overall data rate of 100 kHz going to the L2 trigger stage. If the event has passed the L1 trigger cut, it is sent to the L2 trigger which contains software algorithms able to do a first reconstruction of the event. A further reduction factor of 10 is achieved by the L2 trigger cut, leading to a 10 kHz event rate sent to the PC-merger and then stored to disk.

2.6.2 The Data Acquisition

Most part of the NA62 sub-detectors uses a common readout system based on the TEL62 motherboard and the TDCB daughter-card. This system provides a good time resolution in a high-rate environment and ensures a manageable data rates. The TDC readout system reads the pulse information by using the Time-Over-Threshold technique when both leading and trailing edges are measured. The sub-detectors that adopt the TEL62 readout system are: the CEDAR, the LAVs, the CHANTI, the RICH, the CHOD and the MUV3. The readout of the other sub-detectors is based either on a custom TDC approach or an ADC readout. The number of channels and the hit rate for each sub-detectors are shown in Table 2.3. The total number of channels of the experiment to be read is about 80 000; considering the rate to which each sub-detector is exposed and the event size detected by each sub-detectors, the NA62 DAQ system produces about 2 TB/s of raw data bandwidth.

Sub-detectors	**Total channels**	**Hit rate [MHz]**
CEDAR	384	50
GTK	54000	2700
LAV	4992	11
CHANTI	276	2
STRAW	7168	240
RICH	1929	11
CHOD	128	12
IRC	4	6
LKr	13248	40
MUV1+MUV2+MUV3	576	30
SAC	4	2

Table 2.3: Number of channels and typical rates of NA62 sub-detectors.

Chapter 3

Efficiency studies of the offline NA62 RICH multi-ring reconstruction algorithm

Cherenkov ring identification is crucial to identify an electron track in a multi-track event. The official offline NA62 RICH multi-ring reconstruction software is based on the Ptolemy's algorithm: starting from purely geometrical considerations, this algorithm allows a trackless multi-ring reconstruction [54]. An explanation of Ptolemy's algorithm, described in the mathematical and astronomical treatise *The Almagest*, is presented in Section 3.1.

Monte Carlo studies on the momentum threshold for Cherenkov radiation are described in Section 3.2.

Efficiency studies of the official NA62 multi-ring reconstruction software when used as an online software trigger are described in Section 3.3.

The analysis shown in this chapter is based on the output of the official NA62 Monte Carlo based on the Geant4 package [55] and of the official NA62 Reconstruction software [56].

3.1 The RICH reconstruction algorithm

The first book of Ptolemy's Almagest ($M\epsilon\gamma\alpha\lambda\eta\ \Sigma\upsilon\nu\tau\alpha\xi\iota\varsigma$, *The Great Treatise*) contains Ptolemy's Theorem. This theorem presents a relation between the lengths of the four sides and the two diagonals of a cyclic quadrilateral, that is a quadrilateral whose vertices lie on a circle. The theorem states:

> *"In a convex quadrilateral, if the sum of the products of its two pairs of opposite sides is equal to the product of its diagonals, then the quadrilateral can be inscribed in a circle."*

In particular the definition of a quadrilateral circle is given as follows with respect to Figure 3.1:

> *A quadrilateral is cyclic, i.e. the vertices lie on a circle, if and only if the following relation is satisfied:*

$$\overline{AD} \times \overline{BC} + \overline{AB} \times \overline{DC} = \overline{AC} \times \overline{BD}. \tag{3.1}$$

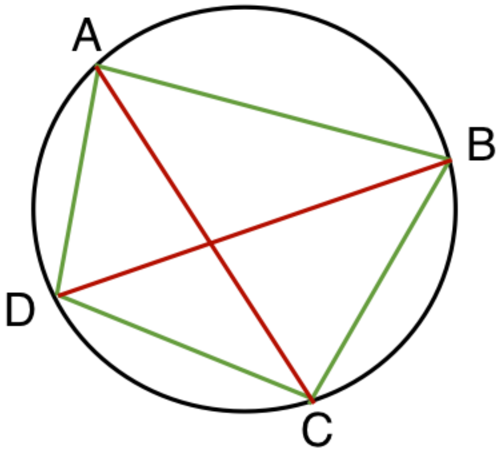

Figure 3.1: The Ptolemy theorem.

A secondary particle produced from kaon decays (pion, muon or electron) will produce hits in the RICH PMTs if the momentum of the particle is above the momentum threshold for Cherenkov radiation.

Starting from these hits, the algorithm has to reconstruct the Cherenkov ring associated with the particle. The procedure is quite challenging if there is more than one Cherenkov ring to reconstruct in the absence of any information about the ring centre position (trackless ring reconstruction algorithm).

Eight directions in the PMT hits space are chosen as indicated in Figure 3.2. Considering one direction, for instance the direction labelled with *Up*, this direction represents a new reference axis. The algorithm selects three PMT hits with the smallest coordinate according to this new axis. If these three hits, called a triplet, do not lie on the same line in the PMTs space and the minimum distance between each of them is 90 mm[1], this triplet represents the starting PMT hits from which the algorithm begins to reconstruct the first Cherenkov ring. If there is no starting triplet satisfying the above conditions along this direction, none of the Cherenkov rings is reconstructed and a new reference direction is chosen (Figure 3.2).

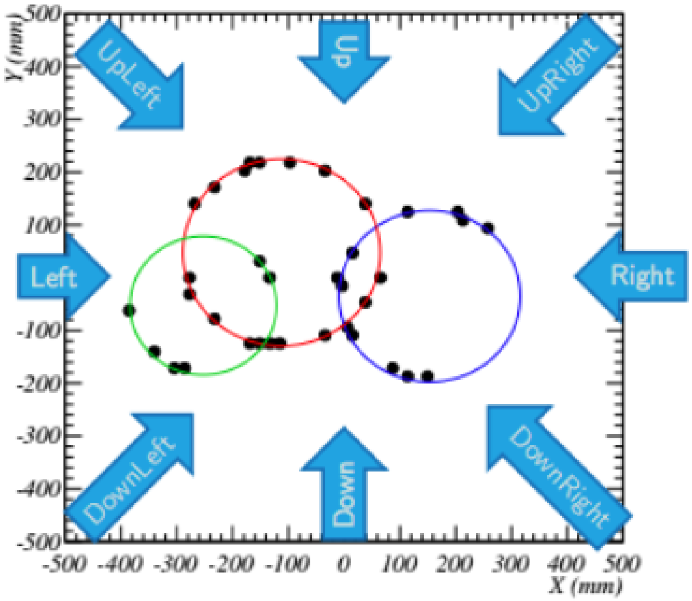

Figure 3.2: The RICH multi-ring reconstruction for a 3 tracks signature [57].

---

[1] It has been optimised by Monte Carlo simulation.

For instance, looking at Figure 3.1, the points A, B, D can be considered as the three PMT hits of the starting triplet chosen along the direction *Up* in Figure 3.2. The algorithm looks for the point C (the PMT hit) satisfying the Ptolemy theorem according to the following relation:

$$\left|\overline{AD} \times \overline{BC} + \overline{AB} \times \overline{DC} - \overline{AC} \times \overline{BD}\right| < d^2, \tag{3.2}$$

where d^2 is 40 mm^2 [2]. Naturally, more than one PMT hit can satisfy the relation 3.2. All the PMT hits satisfying the relation 3.2, collected from the starting triplet chosen along the fixed direction, represent the first ring candidate.

In order to reconstruct the other potential Cherenkov rings with the residual PMT hits, the previous operations are repeated along the same direction. Hence a new starting triplet is chosen from the residual PMT hits along the *Up* direction. All the PMT hits satisfying the relation 3.2 constitute a second ring candidate. These operations are repeated until fewer than four PMT hits are available. Once all possible PMT hits are classified as belonging to different ring candidates, a set of ring candidates is obtained for that fixed direction (in this case for the *Up* direction). If no PMT hits collected from the starting triplet, along that direction, satisfy the condition 3.2, the ring candidate is discarded since it is required to be reconstructed with at least four PMT hits, by construction. A ring-fit is performed on each of the ring candidates. The total χ^2 of the set of ring candidates is defined as the sum of the χ^2 obtained from the ring-fit on each ring candidate. Hence, after choosing one of the eight directions shown in Figure 3.2, a set of reconstructed rings with a total χ^2 is obtained after a ring-fit procedure.

All the operations described above are repeated for the other seven directions shown in Figure 3.2. At the end, eight sets of ring candidates are obtained, each of them with a total χ^2 value. The best set of reconstructed ring candidates, among the eight directions, is chosen according to the smallest total χ^2.

---

[2] It has been optimised by Monte Carlo simulation.

3.2 Monte Carlo RICH multi-ring studies

Before starting the efficiency study of the multi-ring reconstruction algorithm, simple studies on the momentum threshold for Cherenkov radiation are performed to compare the expected theoretical value of the momentum threshold with that obtained from Monte Carlo truth information [3].

A Monte Carlo sample of 10 000 $K^+ \to \pi^+\pi^+\pi^-$ events is generated using the official NA62 Monte Carlo software [56]. The events are generated with the kaon decay vertex lying in the NA62 fiducial region (105m< z <165m). The events for which the kaon decay products decay or interact after the RICH mirror, which is placed at 236 875 m along the z-axis of the NA62 reference frame, are selected.

The image of a Cherenkov cone on the focal plane is a ring of radius r_{ring} given by, in the small Cherenkov angle approximation (see Chapter 2, Section 2.3.1.1):

$$r_{ring} = \sqrt{r_{max}^2 - f^2 \frac{m^2}{p^2}}, \tag{3.3}$$

where:

- f is the focal length;
- $r_{max} = f \tan\theta_{max} = f\sqrt{n^2 - 1}$ (n is the refractive index of the gas radiator and θ_{max} is the maximum angle at which the Cherenkov radiation is emitted with respect to the particle trajectory);
- p is the particle momentum;
- m is the particle mass,

---

[3] Monte Carlo truth information indicates the quantity obtained from Geant4 simulation before digitization process.

If the momentum is below the Cherenkov threshold, the quantity in 3.3

$$r_{max}^2 - f^2\frac{m^2}{p^2} \tag{3.4}$$

is negative. Given the momentum threshold for a particle of mass m to create a Cherenkov cone (Chapter 2, Section 2.3.1.1):

$$p_t = \frac{m}{\sqrt{n^2-1}}, \tag{3.5}$$

and substituting formula 3.5 into relation 3.3, it is evident that, at the momentum threshold the quantity in 3.4 is zero and then the radius is zero. It is possible to compute the momentum threshold for Cherenkov radiation for a pion, requiring:

$$r_{max}^2 - f^2\frac{m_\pi^2}{p^2} > 0, \tag{3.6}$$

and knowing that $r_{max} = f\tan\theta_{max} = f\sqrt{n^2-1}$ and $(n-1) = 6.2 \times 10^{-5}$, it means

$$p > \frac{m_\pi}{\sqrt{n^2-1}} \approx 90 \cdot m_\pi = 12.6 \text{ GeV/c}, \tag{3.7}$$

where m_π is the mass of the pion.

The distribution of the minimum momentum among the three pions' momenta from Monte Carlo truth information for a $K^+ \to \pi^+\pi^+\pi^-$ sample is shown in Figure 3.3. The minimum pion momentum above the Cherenkov momentum-threshold to create a Cherenkov cone, from relation 3.7, is indicated by a vertical arrow. It has been verified that the request to have the radius larger than zero, according to formula 3.6, leads to a momentum threshold equal to $\sim$ 12 GeV/c, in agreement with the result obtained in formula 3.7. 91% of $K^+ \to \pi^+\pi^+\pi^-$ events have all pions above the Cherenkov threshold.

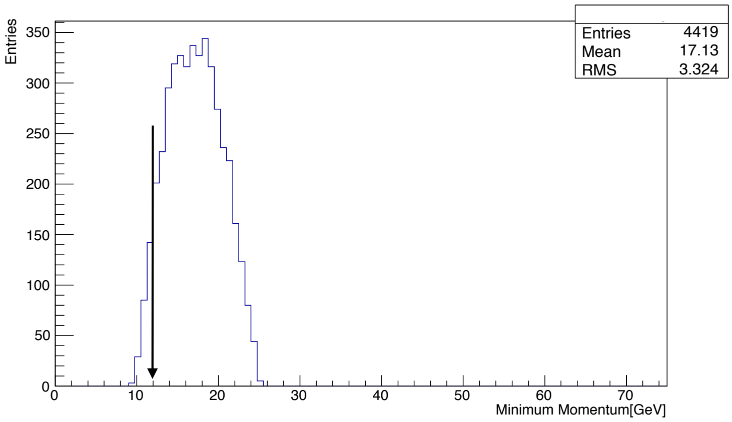

Figure 3.3: Minimum pion momentum distribution from Monte Carlo truth information for a $K^+ \to \pi^+\pi^+\pi^-$ sample. The vertical arrow identifies the minimum pion momentum above the Cherenkov momentum-threshold to create a Cherenkov cone.

To estimate the efficiency of the official NA62 multi-ring reconstruction algorithm, the radius and the centre of the Cherenkov ring obtained from the Monte Carlo truth information (Monte Carlo Cherenkov ring) are used: it is possible then to perform efficiency studies of the multi-ring reconstruction algorithm. The analysis is performed comparing the reconstructed rings with the information on the centre position and on the ring radius computed directly from the kinematics of the event. The ring radius is obtained from the kinematics as described by the formula 3.3.

The ring centre coordinates are computed from the kinematics as follows:

$$\begin{aligned} X_{centre} &= f \tan\theta_x^{am}, \\ Y_{centre} &= f \tan\theta_y^{am}, \end{aligned} \tag{3.8}$$

where $\theta_x^{am}(\theta_y^{am})$ is the angle formed by the projection of the flight direction of the emitting particle on the $xz(yz)$ plane and the $x(y)$ axis:

$$\begin{aligned} \theta_x^{am} &= \arcsin(p_x^{am}/p) \\ \theta_y^{am} &= \arcsin(p_y^{am}/p). \end{aligned} \tag{3.9}$$

The quantities p_x^{am} and p_y^{am} in formula 3.9 are the x and y components of the momentum p of the particle After the Magnet. In particular, due to the small thickness of the magnet with respect to the bending radius of the particle trajectory, the quantity θ_x^{am} can be approximated as follows:

$$\theta_x^{am} = \theta_x^{bm} - q \cdot \frac{p_x^{kick}(x, y)}{p}, \tag{3.10}$$

where θ_x^{bm} is the angle defined above Before the Magnet, (x, y) are the coordinates of the position of the particle at the entrance of the magnet and $p_x^{kick}(x, y)$ is given by the integral of the y component of the magnetic field (B_y) along the particle trajectory multiplied by the electric charge. The dimension of the p_x^{kick} and p is expressed in multiples of eV/c. Because the B_y component is not uniform, the mean variation of the $p_x^{kick}(x, y)$ on the surface xy of the magnet is of the order of few percent. The mean value of the p_x^{kick} is 270 MeV/c with a variation of $\lesssim$5% in the region $\sim$ 50 cm away from the centre of the magnet. In the version of the Monte Carlo software used to perform the studies described in this thesis, the effects on p_x^{kick} due to the non-uniformity of the magnetic field were not taken into account as this effect is negligible. For this reason, p_x^{kick} is considered equal to 270 MeV/c in the current studies. The x component of the momentum after the magnet can be written as:

$$p_x^{am} = p_x^{bm} - q \cdot 270\,\mathrm{MeV/c}. \tag{3.11}$$

For θ_y^{am} and $p_y^{kick}(x, y)$, the effect of the magnetic field is neglected and they are assumed to be equal to the angle θ_x^{bm}.

Finally the coordinates of the centre of the Cherenkov ring in 3.8, considering relations 3.9 and 3.11, are written as:

$$\begin{aligned} X_{centre} &= f \cdot \tan\Big[\arcsin\Big(\frac{p_x^{bm} - q \cdot 270}{p}\Big)\Big] \\ Y_{centre} &= f \cdot \tan\big[\arcsin(p_y^{am}/p)\big] . \end{aligned} \tag{3.12}$$

As already mentioned, if the quantity $r_{max}^2 - f^2 \frac{m^2}{p^2}$ is negative (or equal to zero), no

Cherenkov light is emitted and there is no Cherenkov ring. It is possible to count the number of Cherenkov rings obtained from the Monte Carlo truth (Monte Carlo Cherenkov rings) requiring $r^2_{max} - f^2\frac{m^2}{p^2} > 0$.

3.3 Efficiency study of the RICH multi-ring reconstruction algorithm

The aim of the efficiency study of the offline NA62 RICH multi-ring reconstruction algorithm is to check how many rings the algorithm reconstructs with respect to the number of Cherenkov rings expected from the Monte Carlo truth information, that are in the RICH detector acceptance. This is a completely new study of the algorithm's efficiency that has not been done before within NA62. In case this algorithm is used as online software trigger, it is necessary to have a high efficiency, as every event discarded by the software trigger can not be retrieved in any further stage of the analysis.

The study is performed using the reconstructed rings and the Monte Carlo rings. The reconstructed rings are selected according to the smallest χ^2 after a ring-fit procedure (see Section 3.1). The Monte Carlo rings are the radius and centre computed by the relations 3.3 and 3.12, starting from the Monte Carlo truth information. The radius and centre coordinates of the Monte Carlo ring are computed only for particles with a momentum above the threshold for Cherenkov radiation obtained from the Monte Carlo truth information.

The efficiency study is performed with a Monte Carlo sample of 10 000 $K^+ \rightarrow \pi^+\pi^+\pi^-$ decays. Only the events in which the kaons decay in the fiducial region and all the three pions decay or interact after the RICH mirror are selected. It is observed that after requiring all three pions decay or interact after the RICH mirror, only events with at least two rings above the Cherenkov threshold are kept.

Two categories of events are defined: the first category includes events with two rings above the Cherenkov threshold and the second category includes events having three rings above the Cherenkov threshold. The efficiency of the multi-ring reconstruction algorithm is estimated for each category.

The information available for each event to study the efficiency of the algorithm is:

- the number of Monte Carlo rings generated by the particles in the radiator gas with momentum above the momentum threshold for Cherenkov radiation;
- the number of reconstructed rings;
- the centre and radius of each Monte Carlo ring;
- the centre and radius of each reconstructed ring;
- the total number of the RICH PMT hits [4];
- the number and positions of the RICH PMT hits used to reconstruct each Cherenkov ring;
- the number and positions of the RICH PMT hits not used to reconstruct any Cherenkov ring, called residual RICH PMT hits.

Each event is classified according to the number of Monte Carlo rings above the Cherenkov threshold. Given the event category i ($i = 2$ or 3 Monte Carlo rings), the efficiency ϵ of the multi-ring reconstruction algorithm for each event category i is defined as follows:

$$\epsilon(i) = \frac{N^{reco}_{events}(i)}{N^{MC}_{events}(i)}, \tag{3.13}$$

where $N^{MC}_{events}(i)$ is the number of Monte Carlo events belonging to the event category i obtained from the Monte Carlo truth while $N^{reco}_{events}(i)$ is the number of reconstructed events for which the algorithm is efficient. In particular, the events in which the number of reconstructed rings is at least the number of expected Monte Carlo rings are considered fully efficient. This means that the quality of the reconstructed rings is not considered, particularly for those events in which the number of reconstructed

---

[4] The PMT hits are the reconstructed PMT hits obtained after digitization.

rings is larger than the number of expected Monte Carlo rings. This is acceptable where the algorithm is used to act as software trigger: if the trigger request relies only on a minimum number of tracks (i.e. on the number of reconstructed rings), the algorithm is considered suitable for this trigger purpose. On the other hand, the quality of each reconstructed ring is important for an offline analysis. Formula 3.13 defines the multi-ring algorithm efficiency. This efficiency definition does not take into account the efficiency to have reconstructable PMT hits, i.e. PMT signals greater than a fixed voltage threshold, and the efficiency of the simulated detector.

For events in which the number of reconstructed rings is smaller than the number of expected Monte Carlo rings, the procedure to evaluate the efficiency of the multi-ring reconstruction algorithm for each category of events is described in Section 3.3.1.

From this analysis, the efficiency of the multi-ring reconstruction algorithm is $\sim 70\%$ for both the event categories. In order to investigate the reason behind the $\sim 30\%$ inefficiency, a further analysis is performed, as described in Section 3.3.2.

3.3.1 Efficiency evaluation

For those events in which the number of reconstructed rings is lower than the number of Monte Carlo rings, the analysis associates the PMT hits of the event with all Monte Carlo rings above the Cherenkov threshold. Associating a PMT hit with a Monte Carlo ring means to compute the distance of the PMT hit with respect to the Monte Carlo ring. The distance between the PMT hit and the Monte Carlo ring is obtained by computing first the distance between the PMT hit and the centre of the Monte Carlo ring and then subtracting the radius of the Monte Carlo ring. In order to associate the PMT hit with the Monte Carlo ring, this distance must be smaller than 9 mm, which is the radius of the effective sensitive area of the photon detection system, i.e. PMT and Winston cone (Chapter 2, Section 2.3.2.1).

If the number of Monte Carlo rings with more than three PMT hits associated is larger than the number of reconstructed rings, the algorithm is inefficient. Otherwise, if the number of Monte Carlo rings with more than three hits associated is less than or equal to the number of reconstructed rings, the algorithm is fully efficient.

The criteria to associate more than three PMT hits is due to the construction of the multi-ring reconstruction algorithm, which reconstructs a Cherenkov ring with at least four PMT hits. The Ptolemy's algorithm reconstructs a ring from a starting triplet of PMT hits. The triplet is chosen according to some conditions. For example a minimum distance between each pair of the three PMT hits is required and the three PMT hits do not have to lie on a line. The hit-associating procedure tries to associate each PMT hit with a Monte Carlo ring. This operation does not check if the PMT hits lie on a line because it would be redundant: if they are associated with a Monte Carlo ring they can not lie at the same time on a line. This does not have any impact on the estimate of the efficiency.

The results of the analysis of the official RICH multi-ring reconstruction algorithm are shown in Table 3.1 for each event category. The error is computed in the following way (the error of the binomial distribution):

$$\Delta\epsilon(i) = \sqrt{\frac{\epsilon(i)\cdot(1-\epsilon(i))}{N^{MC}_{events}(i)}}. \tag{3.14}$$

Event category i	$\frac{N^{reco}_{events}(i)}{N^{MC}_{events}(i)}$	$\epsilon(i)$
2	$\frac{110}{158}$	0.70±0.04
3	$\frac{1199}{1702}$	0.70±0.01

Table 3.1: Efficiency of the multi-ring algorithm for the events with two and three Monte Carlo rings above the Cherenkov threshold.

The distribution of the fraction of events as a function of the number of not reconstructed Cherenkov rings is shown in Figures 3.4 and 3.5 for the events with two and three Monte Carlo rings above the Cherenkov threshold, respectively. The fraction of events considered efficient ($\sim$ 70% for both the event categories) has zero not reconstructed Cherenkov rings. Moreover, this fraction of events, according to the definition of the efficiency given in Section 3.3.1, includes both the events with a number of reconstructed rings greater than or equal to the number of Monte Carlo rings, and the events considered efficient with a number of reconstructed rings lower than the number of Monte Carlo rings.

The fraction of events with at least one not reconstructed Cherenkov ring corresponds to the remaining $\sim 30\%$ considered inefficient. For the events with two Monte Carlo rings above the Cherenkov threshold, the $\sim 30\%$ inefficiency events, i.e. events where rings are not both reconstructed, always have one not reconstructed Cherenkov ring and hence it has only one reconstructed ring (Figure 3.4). For the events with three Monte Carlo rings, the $\sim 30\%$ inefficiency events has one ($\sim 16\%$) or two ($\sim 13\%$) not reconstructed Cherenkov rings (Figure 3.5).

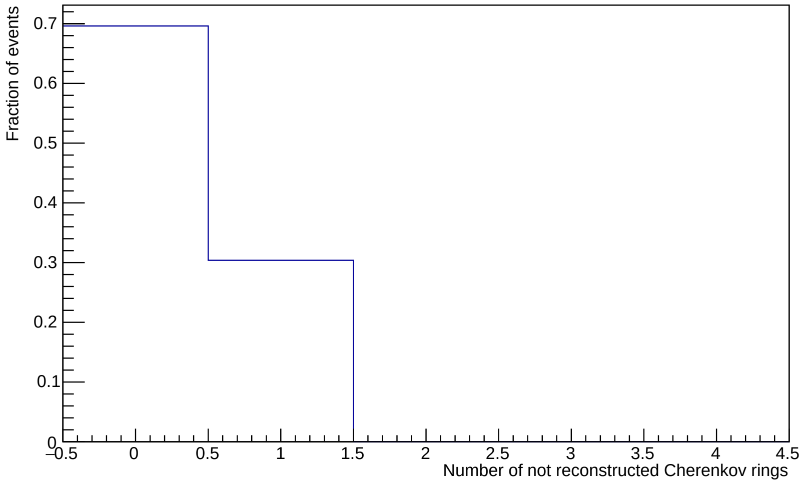

Figure 3.4: Distribution of the fraction of events with two Monte Carlo rings above the Cherenkov threshold as a function of the number of not reconstructed Cherenkov rings .

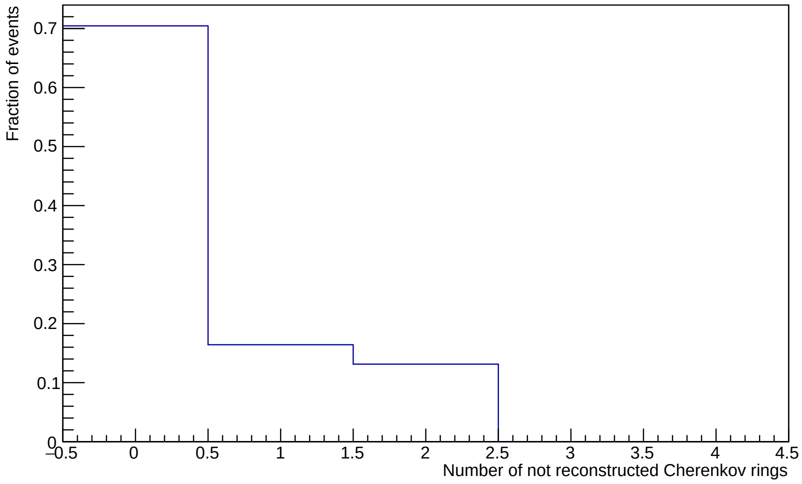

Figure 3.5: Distribution of the fraction of events with three Monte Carlo rings above the Cherenkov threshold as a function of the number of not reconstructed Cherenkov rings.

3.3.2 Investigation of the inefficiency

In order to investigate the reason behind this $\sim 30\%$ inefficiency of the multi-ring reconstruction algorithm, a further analysis is performed. This analysis, as before, is based on the comparison of the number of Monte Carlo rings above the Cherenkov threshold with the number of reconstructed rings.

If the number of reconstructed rings is smaller than the number of Monte Carlo rings, the first step is to match each reconstructed ring with one of the Monte Carlo rings. Matching each reconstructed ring with the Monte Carlo ring means satisfying the following criteria:

a. the particle that generated the Cherenkov ring is required to be the same both for the reconstructed ring and the Monte Carlo ring;

b. the absolute value of the difference between the radius of the reconstructed ring and the radius of the Monte Carlo ring is required to be smaller than 10mm (DeltaRadius in Figure 3.6);

c. the distance between the centre of the reconstructed ring and the centre of the

Monte Carlo ring is required to be smaller than 20 mm (DeltaCentre in Figure 3.7).

The particle that generated the Monte Carlo ring is known directly from the Monte Carlo output. The PMT hits of a single Cherenkov ring are generated by the Cherenkov light produced by the particle passing through the gas radiator of the RICH and the information about the particle ID generating each PMT hit is stored. In order to identify the particle associated with the reconstructed ring, one reconstructed ring and only the PMT hits associated with it are considered and it is checked that the same generating particle is associated with each PMT hit.

A suitable criterion to define good quality of a reconstructed ring is that all the PMT hits associated with the reconstructed ring are generated by the same particle. In this case the identification of the particle associated with the reconstructed ring is immediate: it is the particle that generated the PMT hits associated with the ring.

However, the Cherenkov ring can also be reconstructed with PMT hits generated by different particles and therefore different Cherenkov rings. In this case of PMT hits from multiple particles being reconstructed as a single ring, the particle associated with the reconstructed ring is defined as the particle responsible for generating the largest number of PMT hits associated with the reconstructed ring. A ratio between the largest number of PMT hits generated by the same particle and the number of PMT hits generated by different particles is defined. The particle is considered to be correctly identified if this number of hits is at least $\frac{1}{3}$ of the all hits from which the ring is formed.

The condition b(c) is determined by looking at the distribution of the absolute value of the difference between the radius(centre) of the reconstructed and Monte Carlo rings for a $K^+ \to \mu^+\nu_\mu$ sample (see Figure 3.6 and Figure 3.7). For each distribution the value is chosen to include 90% of the $K^+ \to \mu^+\nu_\mu$ events, and the value is 10(20) mm for the distance between the radius(centre) of the reconstructed ring and the radius(centre) of the Monte Carlo ring.

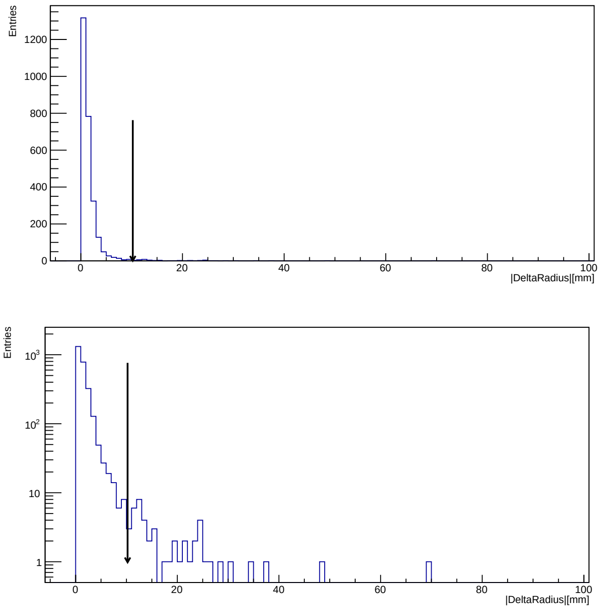

Figure 3.6: Absolute value of the difference between the radius of reconstructed and Monte Carlo ring for a $K^+ \to \mu^+\nu_\mu$ sample (upper plot). The upper plot with $y-$axis in log-scale where tail is more appreciated (bottom plot).

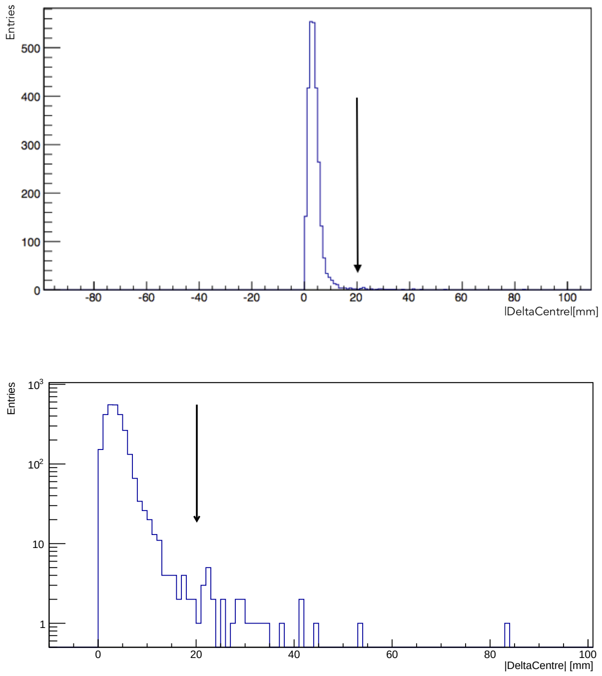

Figure 3.7: Absolute value of the difference between the centre of reconstructed and Monte Carlo ring for a $K^+ \to \mu^+\nu_\mu$ sample (upper plot). The upper plot with $y-$axis in log-scale where tail is more appreciated (bottom plot).

After matching the reconstructed ring with the Monte Carlo ring, the next step is to associate the residual PMT hits with the Monte Carlo ring not previously matched.

If no more than three residual PMT hits are associated with any of the Monte Carlo rings (not previously matched), the algorithm is not supposed to reconstruct these Monte Carlo rings with the available residual PMT hits.

On the other hand, if the "hit-associating" procedure succeeds in associating more than three residual PMT hits to one of the Monte Carlo rings not previously matched, it means that this Monte Carlo ring in principle should be reconstructed by the algorithm.

The fraction *f(i)* of events, shown in Table 3.2 for each event category, includes two classes of events: the events for which the number of reconstructed rings is greater than or equal to the number of Monte Carlo rings, and the events for which the number of reconstructed rings is lower than the number of Monte Carlo rings. The latter class represents the event with no more than three residual PMT hits associated with the Monte Carlo ring not previously matched. The notation $N_{events}(i)$ in Table 3.2 is the number of events satisfying the above criteria. The error is computed in the following way:

$$\Delta f(i) = \sqrt{\frac{f(i) \cdot (1 - f(i))}{N^{MC}_{events}(i)}}, \tag{3.15}$$

where the i-index is the event category and $N^{MC}_{events}(i)$ is the number of Monte Carlo events belonging to the event category i.

Event category i	$\frac{N_{events}(i)}{N^{MC}_{events}(i)}$	$f(i)$
2	$\frac{151}{158}$	0.96±0.02
3	$\frac{1608}{1702}$	0.945±0.005

Table 3.2: Fraction of events for which the number of reconstructed rings is equal or larger than the number of Monte Carlo rings, and the events for which the number of reconstructed rings is smaller than the number of Monte Carlo rings with no more than three residual PMT hits associated to the Monte Carlo ring not previously matched. The results are shown for each event category.

From the previous analysis it is clear that most of the $\sim 30\%$ inefficiency of the algorithm is due to the fact that some rings are reconstructed with PMT hits generated by different particles and then attributed to other rings. Hence, wrong PMT hits are associated to one reconstructed ring at the expense of others, leaving too few PMT hits for the last ring to be reconstructed. Since the $\sim 30\%$ inefficiency is mainly due to the partial merge of PMT hits belonging to more than one Cherenkov ring, it is possible to improve the algorithm performance and make it more efficient by tightening the conditions in the pattern recognition. This would represent an important task for future studies of the algorithm.

3.3.3 Summary and discussion of the results

A study of the efficiency of the official RICH multi-ring reconstruction algorithm (Ptolemy's algorithm) is described in the current section.

The efficiency study of the algorithm is performed with a $K^+ \to \pi^+\pi^+\pi^-$ Monte Carlo sample. It is observed that after requiring all the three pions decaying or interacting after the RICH mirror, only the events with at least two Monte Carlo rings above the Cherenkov threshold are kept. This leads to the definition of two event categories: the events with two Monte Carlo rings above the Cherenkov threshold and the events with three Monte Carlo rings above the Cherenkov threshold.

The analysis procedure consists of associating all the PMT hits of the events to all the Monte Carlo rings above the Cherenkov threshold. If the number of Monte Carlo rings with more than three PMT hits associated is larger than the number of reconstructed rings, the algorithm is inefficient; otherwise if the number of Monte Carlo rings with more than three PMT hits associated is equal or smaller than the number of reconstructed rings the algorithm is efficient.

The result of the analysis shows that the efficiency of the official RICH multi-ring reconstruction algorithm is $\sim 70\%$, for each event category. A further analysis is performed to investigate the reason behind the $\sim 30\%$ inefficiency of the algorithm.

It consists of matching each reconstructed ring to one of the Monte Carlo rings and associating the residual PMT hits with the Monte Carlo rings not previously matched. The fraction of events with a number of reconstructed rings greater or equal to the number of Monte Carlo rings, and for which the number of reconstructed rings is smaller than the number of Monte Carlo rings, having no more than three residual PMT hits associated with the Monte Carlo ring not matched, is estimated to be $\sim$ 95%, for each event category. From the analysis on this fraction of events, it is clear that most of the $\sim 30\%$ inefficiency of the algorithm is due to the hit sharing of the reconstructed rings. The analysis of the PMT hits associated with the reconstructed ring shows that some rings are reconstructed with PMT hits generated by different particles and then attributed to other Cherenkov rings. The inefficiency is due to the wrong PMT hits associated with one reconstructed ring at the expense of others, leaving too few PMT hits for the last ring to be reconstructed.

The efficiency analysis does not take into account the distance between each of the PMT hits associated with a ring. It means that if more than three PMT hits are associated with one of the Monte Carlo rings, the distance between each of the PMT hits associated with the Monte Carlo ring is not checked. It is possible that the multi-ring algorithm is not supposed to reconstruct the Monte Carlo ring by construction, since the three PMT hits of the triplet do not have the minimum distance between each of them as required by the algorithm. This feature is not considered in the efficiency studies and it leads to a lower estimation of the efficiency of the algorithm. It represents a possible extension for further studies.

Chapter 4

Trigger strategy to select multi-track events with an electron track

The Level 1 (L1) trigger strategy described in this chapter aims to select multi-track events with an electron track in the final state. The signal to be selected is the $K^+ \to \pi^+ e^+ e^-$ decay channel. A new trigger algorithm for the electron Cherenkov-ring identification is described in detail in chapter 5. The software trigger algorithm for the electron identification can in principle be applied to select every kind of decay with an electron Cherenkov ring in the final state, in the acceptance of the RICH sub-detector. The trigger cut analysis aims to achieve a high efficiency on the signal and a high suppression factor on the background. Achieving a reduction factor of 10 on the event rate with the L1 trigger cut is an important task.

The processes simulated by the official NA62 Monte Carlo software are described in Section 4.1.

In order to study the efficiency of the L1 trigger algorithm, the input from the Level 0 (L0) trigger stage has to be produced (Section 4.2). To simulate a possible L0 strategy able to select multi-track events, I chose to use the CHOD and the RICH sub-detectors as main players at L0. The L0 trigger rates after L0 cuts are estimated for each of the six main kaon decay modes. The obtained results are in agreement with the internal note NA62-14-07 "*Studies of the L0 trigger for rare decays*" [58].

The L1 trigger cut strategy to select multi-track events, based on the analysis of the spatial distribution of the RICH PMT hits, is described in Section 4.3.1. The efficiency of the L1 trigger cut is discussed in Section 4.3.1. The final event rate for the dominant kaon decay modes is also shown.

The role of the RICH sub-detector in discarding the two main background sources, $K^+ \to \pi^+\pi^0$ and $K^+ \to \pi^+\pi^+\pi^-$, is studied in Sections 4.3.2 and 4.3.3. Since the exclusive contribution of the RICH sub-detector in reducing the $K^+ \to \pi^+\pi^0$ background would be smaller than 40%, it is essential to develop a L1 trigger cut strategy to get rid of $K^+ \to \pi^+\pi^+\pi^-$ decays as they represent the second main source of background.

4.1 Monte Carlo sample

The analyses shown in this section are performed using the output of the official NA62 Monte Carlo and the official NA62 Reconstruction software [56]. The outputs of the NA62 Monte Carlo software are called Monte Carlo hits, i.e. non-digitised signals from sub-detectors. After reconstructing the Monte Carlo hits with the NA62 Reconstruction software, the output is analysed within the NA62 Analysis framework. The following processes are simulated.

- **Beam kaons** (K^+). The simulation of the kaon propagation is performed by the TURTLE ray-tracing program [59] up to the beginning of the CEDAR sensitive region ($z \sim$ 69m, see Chapter 2, Table 2.1), and by the Geant4 software afterwards. The kaons decay in the standard decay region from the beginning of the vacuum tank to the end of the NA62 Monte Carlo volume (104 m $< z <$ 300 m). The six main kaon decay modes are simulated separately using detailed generators available within the NA62 Monte Carlo software. They represent the dominant part of the total kaon decay width.

- **Beam pions** (π^+). The simulation of the pion propagation is performed by TURTLE up to the beginning of the CEDAR sensitive region, and by Geant4 afterwards. Pions are not forced to decay in the standard decay region; the pion scattering in the CEDAR and in the GTK is included. The mean free path of a pion with a momentum $p = 75$ GeV/c is $L_\pi = (p/m_\pi)c\tau_\pi = 4.2$ km. It means that about 2.2% of pions decay between the third station of the GTK and the spectrometer magnet.

- **Beam protons** (p). The simulation of the beam protons is performed by TURTLE and Geant4 software as for the beam pions. Protons contribute to the trigger rates via interactions in the CEDAR and GTK because of their stability, $\tau_p > 10^{29}$ years [3].

- **Beam halo**. Muons from the decays of the beam pion and kaon upstream of the GTK station are simulated using external files storing the positions and momenta of the individual muons pre-generated by the HALO program. They are introduced at the third station of the GTK in the front plane ($z \sim 102.4$ m,see Table 2.1) and propagated by Geant4 afterwards.

4.2 The L0 trigger cut analysis

In order to study the efficiency of the L1 trigger cut and the event rate after applying the trigger cut, the input events to the L1 stage, surviving the L0 trigger cut, are produced.

To perform this analysis, the sub-detectors considered for the L0 trigger strategy are the CHOD and the RICH. The following cut is based on the multiplicity in the RICH and CHOD. The results on the L0 trigger rate are a reproduction of the studies described in the internal note NA62-14-07 [58].

It is worth to explain the notation. The primitives generated by the sub-detectors are defined as follows:

- **$\mathbf{R}_{\boldsymbol{N}}$:** coincidence of signals in at least N RICH super-cells (the super-cells are groups of 8 PMTs, see Section 2.3.2.1);
- **$\mathbf{Q}_{\boldsymbol{X}}$:** coincidences in the two CHOD planes in a pair of opposite quadrants (each CHOD plane is divided in 4 quadrants, see Section 2.3.3 and Figure 4.2).

Before evaluating the multiplicity of the RICH and CHOD, the Monte Carlo hits undergo an acceptance and rejection treatment performed by the NA62 Reconstruction software.

The CHOD consists of two planes, therefore a particle passing through the subdetector gives two hits, each in one of the two planes. A CHOD candidate is obtained by matching the hits in the two CHOD planes. In this work the NA62 Reconstruction software is not used to reconstruct a CHOD candidate. The reconstruction of the CHOD candidate and the Q_X condition is performed with a private code in the following way (the input is represented by the reconstructed hits):

- a first check on the z-coordinate of the CHOD hits is performed. The z-coordinate distribution for each CHOD hit for a $K^+ \to \pi^+ e^+ e^-$ sample is shown in Figure 4.1. The two peaks are centred in the longitudinal position of the CHOD planes along the NA62 nominal beam axis, as expected. The two CHOD planes are located at a distance of $\sim$ 40 cm.
- Each CHOD plane can be divided in four quadrants as shown in Figure 4.2. The numbering of the quadrants is arbitrary and it is the same for both planes. The two CHOD planes have 128 read-out channels in total, i.e. 64 channels each. From the read-out channel of the hit, the plane which the hit belongs to is known. Looking at the sign of the hit-coordinates, the fired quadrant is obtained (according to the numbering of the quadrants as shown in Figure 4.2).

- The CHOD candidate is reconstructed looking at the coincidence in the correspondent quadrants in the two planes, i.e. the quadrants with the same

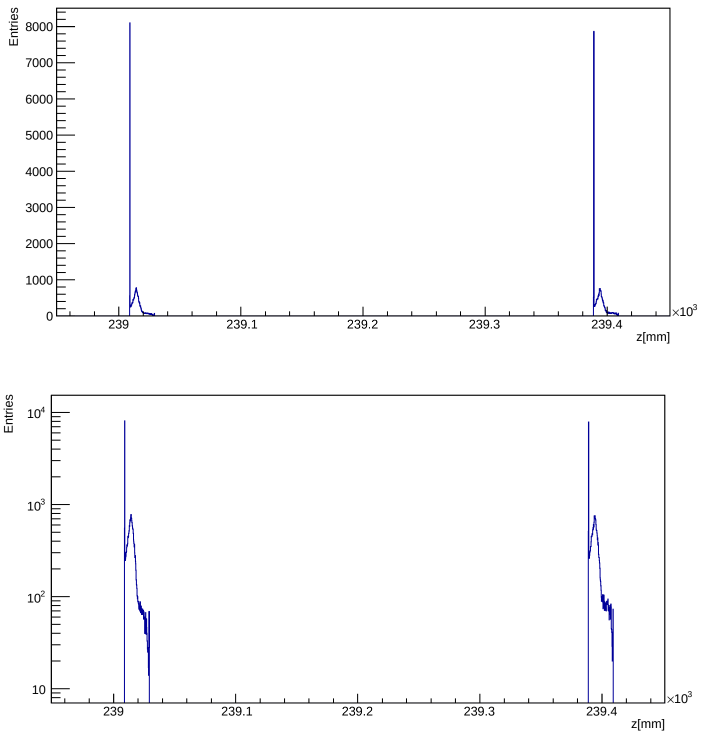

Figure 4.1: z-coordinate of the positions of the hits in the two CHOD planes (upper plot). y-axis of the upper plot shown in log-scale (bottom plot).

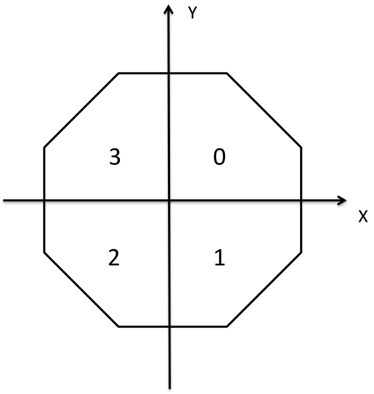

Figure 4.2: Schematic view of one CHOD plane with the numbering of the quadrants.

number. If both of the corresponding quadrants count more than zero hit, the CHOD candidate for that quadrant is obtained.

- The Q_X condition is built looking at the number of CHOD candidates in a pair of opposite quadrants: it means in the 0 and 2 quadrants, and 3 and 1 quadrants (Figure 4.2). If each quadrant of the pair counts at least one candidate, the Q_X condition for the event is satisfied.

The evaluation of the number of the RICH super-cells per event is not performed by the NA62 Reconstruction software. Starting from the reconstructed RICH hits, the number of super-cells is obtained by a private code in the following way:

- for each reconstructed RICH hit the corresponding super-cell ID is known. The super-cell ID is the number that identifies the super-cell which the RICH hit belongs to. The super-cell is a group of 8 neighbouring PMTs. From the hardware point of view, the super-cell is a stand-alone element read-out by a specific channel and labelled by an ID number.
- An array with a size equal to the total number of RICH super-cells, i.e. 244, is built. Each element of the array stores how many times each super-cell is fired.
- Some RICH hits could belong to the same super-cell. To avoid an over estimation of the number of super-cells, a counter is incremented each time a new super-cell is fired, looking at the content of the previous array. The result of the counter is the number of distinguished super-cells fired in the event.

One possible L0 trigger strategy to select multi-track events can consist in the following criteria:

$$\mathbf{R_{10}\ AND\ Q_{\boldsymbol{X}}}^{1}.$$

It means that only the events with at least 10 fired super-cells in the RICH and with a coincidence in the two CHOD planes in a pair of opposite quadrants are sent to the L1 trigger stage.

The total rate of kaon decays in the NA62 "standard decay region", 104m$< z <$300m, is estimated as:

$$\mathrm{R_K} = \mathrm{F_k} \cdot (1 - \exp(\mathrm{L_v}/\mathrm{L_k})) = 13.2 \quad \mathrm{MHz}, \tag{4.1}$$

---

[1] In the following text it is indicated with $\mathbf{R_{10}} \cdot \mathbf{Q}_{\boldsymbol{X}}$.

where $\mathrm{F_k}$ = 45 MHz is the kaon rate, $\mathrm{L_v}$ = 196 m is the length of the standard decay region and $\mathrm{L_k}$ = 563.9 m is the K^+ decay length ($\mathrm{L_k} = \frac{\mathrm{p}}{\mathrm{m_k}} c\tau_\mathrm{k}$) at 75 GeV/c. The event rate due to a specific kaon decay is obtained by multiplying $\mathrm{R_k}$ by the branching ratio of the decay. The NA62 decay region considered in these studies extends beyond the NA62 detector (the NA62 beam dump is located at $z \sim 265$ m). Therefore the rates due to K^+ decays actually seen by the sub-detectors are smaller than R_K quoted above.

The RICH multiplicity distribution of the hits and super-cells for a $K^+ \to \pi^+ e^+ e^-$ sample is shown in Figure 4.3. Requiring at least 10 super-cells fired rejects 10% of the signal. A Monte Carlo sample of 10000 events is generated for each of the main six kaon decay modes. Kaons decay along the NA62 "standard decay region". The event rates after different L0 cuts, at nominal beam intensity, for each of the main six kaon decay modes are shown in table 4.1. The obtained results are in agreement with the results shown in the internal note NA62-14-07 [58]. From table 4.1 the dominant kaon decay channels are the $K^+ \to \pi^+\pi^0$ ($K_{2\pi}$) and $K^+ \to \pi^+\pi^+\pi^-$ ($K_{3\pi}$). The total rates shown in table 4.1 are obtained neglecting the contributions from accidental effects.

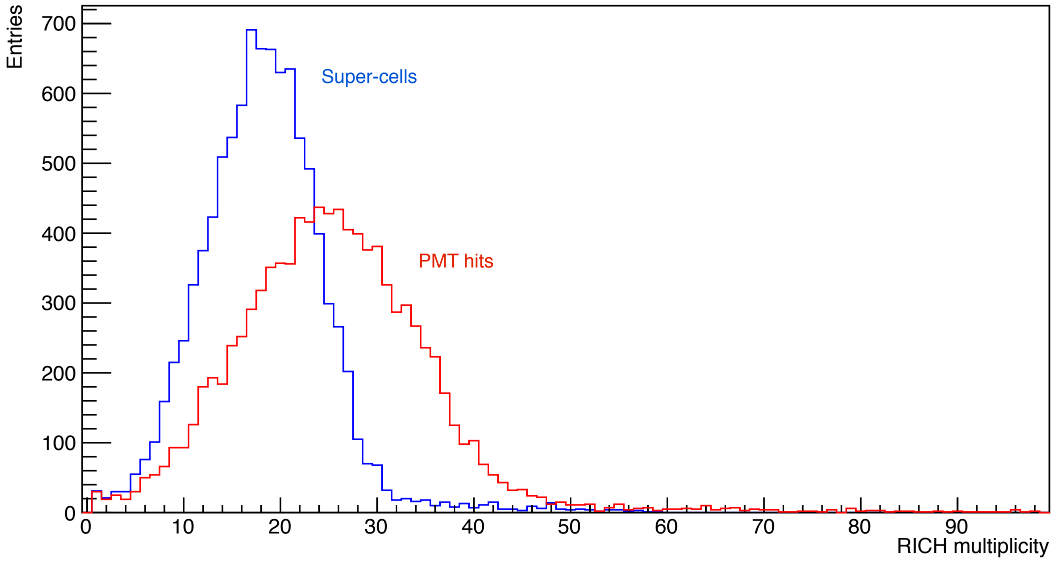

Figure 4.3: RICH multiplicity distribution for hits and super-cells for $K^+ \to \pi^+ e^+ e^-$ decays.

Process	**R_4[MHz]**	**R_{10}[MHz]**	**Q_X[MHz]**	**$R_{10}\cdot$ Q_X[MHz]**
$K_{2\pi}$	1.42	0.93	0.56	0.33
$K_{3\pi}$	0.40	0.34	0.36	0.30
$K_{3\pi}^{00}$	0.13	0.07	0.06	0.03
$K_{\mu 2}$	3.95	2.1	0.02	0.003
$K_{\mu 3}$	0.23	0.14	0.07	0.04
K_{e3}	0.33	0.23	0.09	0.06
Total	6.46	3.81	1.16	0.76

Table 4.1: Q_X and RICH multiplicity trigger rates for the six main kaon decay channels.

The branching ratios of the hadronic decay modes $K_{2\pi}$, $K_{3\pi}$ and $K^+ \to \pi^+\pi^0\pi^0(K_{3\pi}^{00})$ are ~21%, ~6% and ~2%, respectively [3]. The $K_{2\pi}$ and $K_{3\pi}$ (the only sizeable 3-track decay mode) decays are dominant. The $K_{2\pi}$ and $K_{3\pi}^{00}$ can mimic a multi-track decay in the CHOD and the RICH sub-detectors after the π^0 decays two photons followed by a pair-production of at least one photon. An analysis of the contribution to the total Q_X rate from the $K_{2\pi}$ decay is described in Section 4.3.2.

The branching ratios of the leptonic and semi-leptonic decay modes $K^+ \to \mu^+\nu_\mu$ ($K_{\mu 2}$), $K^+ \to \pi^0\mu^+\nu_\mu$ ($K_{\mu 3}$) and $K^+ \to \pi^0 e^+\nu_e(K_{e3})$ are ~64% ~3% and ~5%, respectively [3]. The $K_{\mu 3}$ and K_{e3} can mimic a multi-track decay in the CHOD and in the RICH sub-detectors after the π^0 decays two photons followed by pair-production. Finally the contribution of the $K_{\mu 2}$ decay channel to the multi-track rate, i.e. after the $R_{10}\cdot Q_X$ request, is negligible. On the other hand, the contribution of the $K_{\mu 2}$ to one-track events rate, described by the R_4 primitive, is dominant.

The beam pions (π^+), beam protons (p) and halo muons rates are not reproduced in this work. The estimation of the rates after the R_4 and $R_{10}\cdot Q_X$ request shown in table 4.2 are taken from the internal note NA62-14-07 [58]. The nominal rate of beam pions at the entrance of the decay volume is 525 MHz. Considering that 2.2% of pions decays in the region between the third station of the GTK and the spectrometer magnet, and the branching ratio of $\pi^+ \to \mu^+\nu$ is 99.9% [3], the event rate due to $\pi^+ \to \mu^+\nu$ decay between the third station of the GTK and the spectrometer magnet is 11.5 MHz. Beam pions are also a source of positrons via $\pi^+ \to e^+\nu$ decays (~1kHz, neglected in the previous results) and the $\pi^+ \to \mu^+ \to e^+$ decay chain (~5kHz, included in the previous results).

The nominal rates of beam protons and halo muons at the transverse plane of the GTK third station are 173 MHz and 134 MHz, respectively.

Process	**R_4[MHz]**	**$R_{10}\cdot$ Q_X[MHz]**
π^+	1.11	0.03
p	0.02	-
Halo	4.12	0.01
Total	5.25	0.04

Table 4.2: Beam pion, beam protons and the muons halo rates. The results are taken from the internal note NA62-14-07 [58].

In conclusion the multi-track rate, not including the contribution from the beam pion, beam protons and muons halo, is estimated to be:

$$R(\mathrm{R}_{10} \cdot \mathrm{Q}_\mathrm{X}) = 0.76 \text{ MHz}, \tag{4.2}$$

that is dominated by the $K_{3\pi}$ decay and $K_{2\pi}$ decay followed by photon conversion.

The choice of the $\mathrm{R}_{10}\cdot\mathrm{Q}_X$ for the L0 trigger condition is due to the trigger rate shown in table 4.1. The trigger rate in fact has to satisfy the data bandwidth available for event storage at L1 trigger stage in the PC farm (1 MHz).

A possible minimum bias L0 trigger condition $\mathrm{R}_{10}\cdot\mathrm{Q}_X/100$ could be applied and it is estimated to be $\sim$ 10 kHz. This estimation is taken from the internal note NA62-14-07 [58].

4.3 The L1 trigger cut analysis

4.3.1 Spatial range measurement

A Monte Carlo sample of 10 000 $K^+ \to \pi^+ e^+ e^-$ events is generated with the official NA62 Monte Carlo software. The events are generated with the kaon decay vertex lying in the NA62 "standard decay region". The events satisfying the following criteria are selected:

- the kaon decay vertex must lie in the NA62 fiducial region;
- the total number of RICH hits (called PMT hits) has to be greater than one.

The analysis on the x and y-range distribution of the PMT hits is based on a proposal discussed in the internal note NA62-14-08 [60]. Knowing the position of the fired RICH PMTs, i.e. x-y PMT coordinates, it is possible to find the maximum and the minimum coordinates on the x (X_{min} and X_{max}) and y (Y_{min} and Y_{max}) axes among the RICH PMT hits. The x and y-range of the PMT hits is the respective difference between the X_{max} and X_{min}, and the y_{max} and y_{min} of the PMT hit coordinates and it is defined as follows:

$$\begin{aligned} \Delta X &= X_{max} - X_{min}; \\ \Delta Y &= Y_{max} - Y_{min}. \end{aligned} \tag{4.3}$$

The x and y-range distribution of the RICH PMT hits is different for multi-track events from one-track events. In Figure 4.4 the spatial range distribution of the RICH PMT hits is shown for a $K^+ \to \pi^+ e^+ e^- (K^+ \to \pi^+ \nu\bar{\nu})$ sample in blue(red). The $K^+ \to \pi^+ \nu\bar{\nu}$ decay is chosen as the single track decay.

The x and y projections of the spatial range distribution are shown in Figure 4.5 (the blue and red colour lines refer respectively to $K^+ \to \pi^+ e^+ e^-$ and $K^+ \to \pi^+ \nu\bar{\nu}$ samples). A trigger cut to select a multi-track signature (blue line) at L1 stage could be:

$$\begin{aligned} \Delta X &> 400 \text{ mm}, \\ \Delta Y &> 380 \text{ mm}. \end{aligned} \tag{4.4}$$

This trigger cut is shown in Figure 4.4 by black bars.

The spatial range distribution of the x coordinates is slightly larger than the y

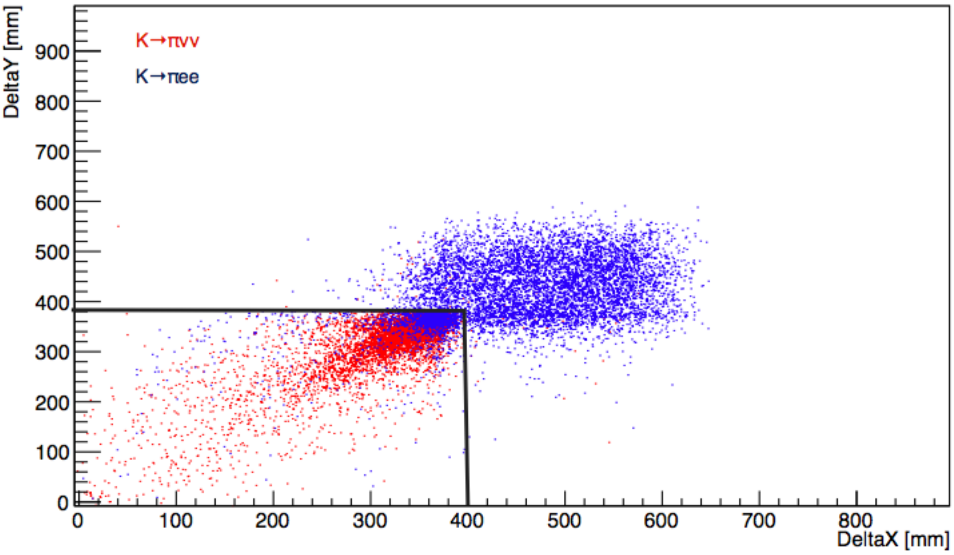

Figure 4.4: In blue(red) the spatial range distribution of the RICH PMT hits for a $K^+ \to \pi^+ e^+ e^-$($K^+ \to \pi^+ \nu\bar{\nu}$) sample. The black bars underline the trigger cut.

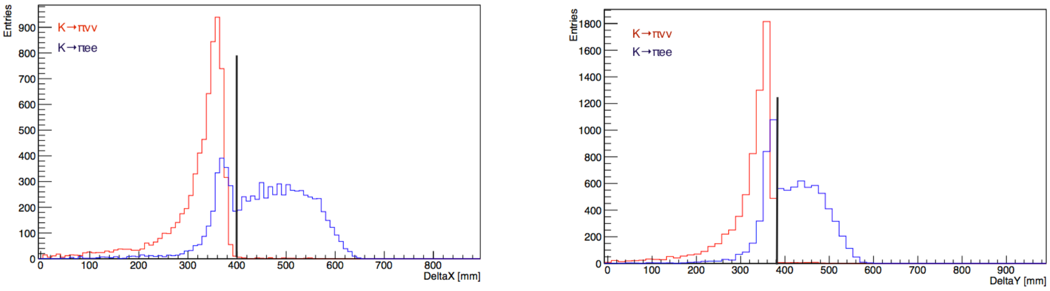

Figure 4.5: ΔX (left) and ΔY (right) distribution for $K^+ \to \pi^+ e^+ e^-$($K^+ \to \pi^+ \nu\bar{\nu}$) in blue(red). The black bars show the trigger cuts described in relation 4.4

component because of the presence of the magnet giving a momentum-kick to the particle in the x direction upstream the RICH entrance.

After the selection of the events with $\Delta X > 400$ mm and $\Delta Y > 380$ mm at L1 trigger stage, the acceptance of the multi-track events $A_{K^+ \to \pi^+ e^+ e^-}$ and of the one-track events $A_{K^+\to\pi^+\nu\bar{\nu}}$ in the signal region is:

- $A_{K^+\to\pi^+e^+e^-} \sim 82\%$;
- $A_{K^+\to\pi^+\nu\bar{\nu}} \sim 1\%$.

The denominator of the acceptance is the number of events passing the L0 condition $\mathrm{R}_{10}{\cdot}\mathrm{Q}_X$ while the numerator is the number of events surviving both the L1 and L0 trigger requests. The spatial spread cut is applied on top of the L0 trigger cut. Two trigger cuts are considered:

- $\mathrm{R}_{10}{\cdot}\ \mathrm{Q}_X \cdot (\Delta X > 400\ \mathrm{mm}\ \|\ \Delta Y > 380\ \mathrm{mm})$[2];
- $\mathrm{R}_{10}{\cdot}\ \mathrm{Q}_X \cdot \Delta X > 400\ \mathrm{mm}$ [3].

The event rates after the L0 trigger cut and the L1 spatial spread cut for the six main K^+ decay modes are shown in table 4.3. The second and the third columns show the total event rates after two different L0 requirements. The last two columns show the total event rates after the L0 cut and two different L1 spatial-spread cuts. A suppression factor of ~ 1.5 on the total event rate is achieved after the L1 trigger cut on the spatial spread of the RICH PMT hits (for both the L1 trigger cuts shown in table 4.3). The main sources of the background to the signal $K^+ \to \pi^+e^+e^-$ are the $K^+ \to \pi^+\pi^0$ (0.17 MHz) and $K^+ \to \pi^+\pi^+\pi^-$ (0.27 MHz) decay channels. The

Process	$\mathbf{Q_X}$**[MHz]**	$\mathbf{R_{10}\cdot\ Q_X}$**[MHz]**	$\mathbf{R_{10}\cdot\ Q_X\cdot\ (\Delta X\ \|\ \Delta Y)}$**[MHz]**	$\mathbf{R_{10}\cdot\ Q_X \cdot \Delta X}$ **[MHz]**
$K_{2\pi}$	0.56	0.33	0.17	0.14
$K_{3\pi}$	0.36	0.30	0.27	0.26
$K_{3\pi}^{00}$	0.06	0.03	0.02	0.02
$K_{\mu2}$	0.02	0.003	–	–
$K_{\mu3}$	0.07	0.04	0.02	0.02
K_{e3}	0.09	0.06	0.04	0.04
Total	1.16	0.76	0.52	0.48

Table 4.3: Event rate after different trigger cuts. The second and the third columns show the total event rates after two different L0 requests. The last two columns show the total event rates after the L0 cut and two different L1 spatial-spread cuts.

---

[2] In the following text it is indicated with $\mathrm{R}_{10}{\cdot}\ \mathrm{Q}_X{\cdot}\ (\Delta X\ \|\ \Delta Y)$.

[3] In the following text it is indicated with $\mathrm{R}_{10}{\cdot}\ \mathrm{Q}_X \cdot \Delta X$.

ΔX distribution for the $K^+ \to \pi^+\pi^0$ and for the $K^+ \to \pi^+\pi^+\pi^-$ decays is shown in Figure 4.6. They are the two dominant sources of background: the $K_{3\pi}$ is the only sizeable 3-track decay mode while the $K_{2\pi}$ can mimic a multi-track decay in the RICH sub-detector after the π^0 decays in two photons followed by a pair-production of at least one photon. For this reason, a cut on the hit spatial spread distribution is not powerful enough to reduce the incoming rate by factor 10 (for more detail see Sections 4.3.2 and 4.3.3). For the same reason, the $K_{3\pi}^{00}$, $K_{\mu3}$ and K_{e3} can mimic a multi-track decay in the RICH but, since their branching ratios are lower than the $K_{2\pi}$ branching ratio (BR($K_{2\pi}$) $\sim$ 21%, BR($K_{3\pi}^{00}$)$\sim$2%, BR($K_{\mu3}$)$\sim$3%, BR(K_3)$\sim$5% [3]), the final rates after the L0 and L1 cuts are lower. Concerning the $K_{\mu2}$ decay, its contribution to the multi-track rate is negligible, i.e. less than 10^{-3} MHz.

Since the L1 trigger cut has to reduce the event rate by a factor 10, it is then necessary to develop a further L1 trigger cut in order to discard the remaining background using the RICH sub-detector.

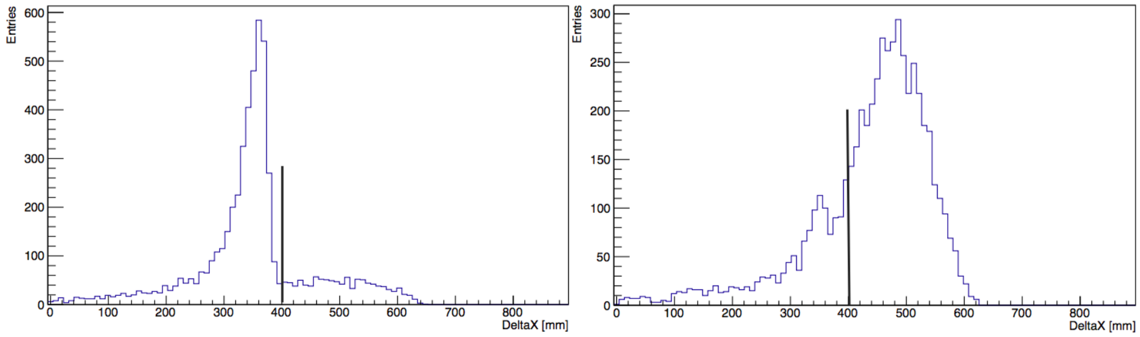

Figure 4.6: ΔX distributions for $K^+ \to \pi^+\pi^0$ (left) and $K^+ \to \pi^+\pi^+\pi^-$ (right) samples. The vertical bars show the value for the L1 trigger cut, i.e. $\Delta X > 400$mm.

4.3.2 $K^+ \to \pi^+\pi^0$ rejection studies

The $K^+ \to \pi^+\pi^0$ decay can mimic the signal after the π^0 decay in two photons when a photon converts in the RICH or before the RICH sub-detector. The first issue to be understood is where the Q$_X$ rate, from a $K^+ \rightarrow \pi^+\pi^0$ decay, is generated. It is worth a reminder that the Q$_X$ rate from $K^+ \rightarrow \pi^+\pi^0$ decay is 0.56 MHz (see table 4.1). Samples of 10000 $K^+ \rightarrow \pi^+\pi^0$ decays are produced with different configurations of the NA62 Monte Carlo software as listed in table 4.4. In the first configuration the RICH sub-detector is disabled from the Monte Carlo simulation, i.e. the RICH itself is removed from Geant4 simulation, and the Q$_X$ drops to 0.10 MHz. In the second configuration the π^0 particle is not tracked by the Monte Carlo simulation, i.e. it is not propagated by Geant4. In the last configuration both the RICH sub-detector and the π^0 particle tracking are disabled, leading to a lower Q$_X$ rate (0.01 MHz).

Monte Carlo configuration	**Q$_X$ rate from $K^+ \rightarrow \pi^+\pi^0$[MHz]**
RICH disabled	0.10
π^0 suppressed	0.11
π^0 suppressed and RICH disabled	0.01

Table 4.4: Q$_X$ rate generated by $K^+ \rightarrow \pi^+\pi^0$ decay in different Monte Carlo configurations.

It is possible to conclude that $\sim$ 80 % of the Q$_X$ rate from $K^+ \rightarrow \pi^+\pi^0$ decay with following photon conversion is due to the presence of the RICH sub-detector. Since the photon conversion occurs in the RICH itself, it is necessary to understand where the photons convert in the RICH.

As before, samples of 10 000 $K^+ \rightarrow \pi^+\pi^0$ decays are produced with different configurations of the RICH sub-detector within the NA62 Monte Carlo software as listed in table 4.5. Each Monte Carlo configuration is run with a part of the RICH sub-detector disabled in order to quantify its contribution to the Q$_X$ rate. If the radiator gas (Neon) and the beam-pipe are disabled the Q$_X$ is 0.51 MHz: it

Monte Carlo configuration	**Q$_X$ rate from $K^+ \rightarrow \pi^+\pi^0$[MHz]**
Neon and beam-pipe disabled	0.51
Mirror and mirror support disabled	0.31
RICH vessel disabled	0.52
RICH entrance window disabled	0.45

Table 4.5: Q$_X$ rate generated by $K^+ \rightarrow \pi^+\pi^0$ decay in different RICH Monte Carlo configurations.

means that the contribution of these two parts to the total Q_X is 9%. In the second configuration the mirror and its support are disabled and the Q_X rates drops to 0.31 MHz: the contribution of the mirror and its support to the Q_X rate is 45%. It means that the RICH is powerless in rejecting these events as the photon conversion happens in the mirror itself. The contributions of the RICH vessel and the RICH entrance window to the total Q_X are 7% and 20%, respectively. In conclusion, the contribution of the RICH in decreasing the Q_X rate from $K^+ \to \pi^+\pi^0$ with respect to the total Q_X would be smaller than 40%.

4.3.3 $K^+ \to \pi^+\pi^+\pi^-$ rejection studies

The $K^+ \to \pi^+\pi^+\pi^-$ decay is one of the main background source to the multi-track decays, i.e. to the signal $K^+ \to \pi^+e^+e^-$ (see table 4.3) using only the RICH subdetector at L1 trigger stage. The current analysis uses the tool provided by the offline NA62 RICH ring-reconstruction software in order to study a proper L1 trigger cut to get rid of the $K^+ \to \pi^+\pi^+\pi^-$ decay.

A $K^+ \to e^+\nu$ and $K^+ \to \pi^+\nu\bar{\nu}$ Monte Carlo samples are generated to investigate the reconstructed radius of the Cherenkov ring for the electron and the pion. The distribution of the reconstructed radii of the electron(blue line) and pion(red line) are shown in Figure 4.7. A $K^+ \to \pi^+e^+e^-$ Monte Carlo sample is generated and the distributions of the radii for all the reconstructed rings from a $K^+ \to \pi^+e^+e^-$(blue line) and $K^+ \to \pi^+\pi^+\pi^-$(red line) samples are shown in Figure 4.8.

Focusing on the $K^+ \to \pi^+e^+e^-$ sample (Figure 4.8), it is possible to identify the main blue peak as the radius of the reconstructed electron ring ($\sim$ 190 mm) in agreement with the electron radius distribution (Figure 4.7). The second tiny peak at $\sim$ 180 mm is the radius of the reconstructed pion ring ($\sim$ 180 mm) in agreement with distribution of the radius of the the pion's ring.

The classification of all reconstructed rings with radius R <180 mm as pions leads to the identification of all rings with radius R $\geq$180 mm as electrons. The fraction

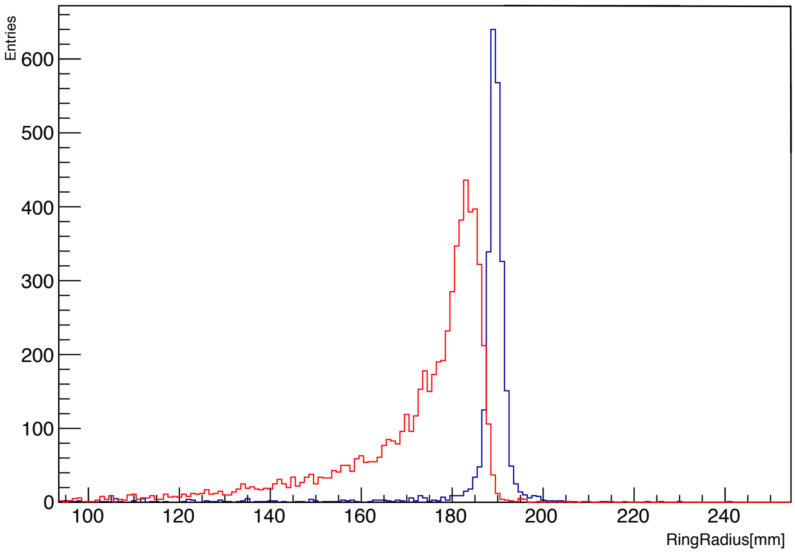

Figure 4.7: Distribution of the reconstructed ring radius of electron (blue) and pion (red) Cherenkov ring from a $K^+ \rightarrow e^+\nu$ and $K^+ \rightarrow \pi^+\nu\bar{\nu}$ sample, respectively.

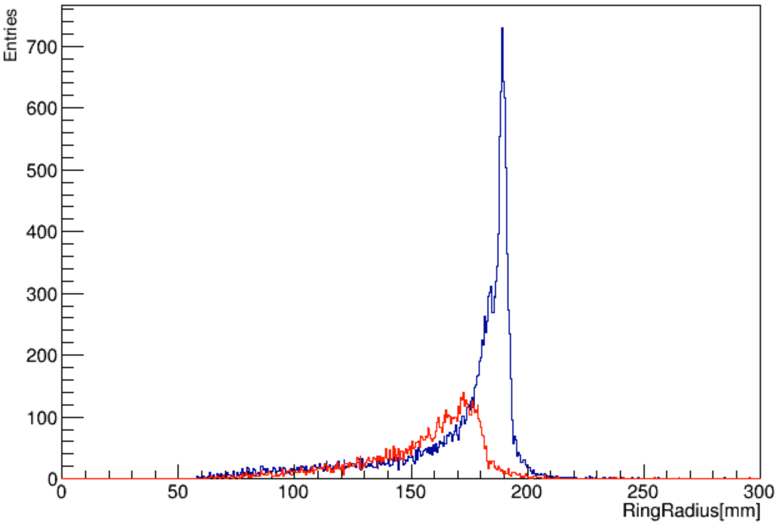

Figure 4.8: Distribution of the reconstructed ring radii of a $K^+ \rightarrow \pi^+e^+e^-$ (blue) and $K^+ \rightarrow \pi^+\pi^+\pi^-$ (red) sample.

of reconstructed pions' rings (N_{pion}) versus the fraction of reconstructed electrons' rings per event ($N_{electron}$) for the $K^+ \to \pi^+ e^+ e^-$ ($K^+ \to \pi^+ \pi^+ \pi^-$) sample is shown in Figure 4.9 (4.10). The integrals over columns and rows are displayed in red. Both histograms in Figures 4.9 and 4.10 are normalized, so their integral is equal to unity. The events considered have passed the L0 requirement, i.e. $\mathrm{R}_{10} \cdot \mathrm{Q}_X$, and the L1 spatial range cut, i.e. $\Delta X > 400$ mm or $\Delta Y > 380$ mm. The kaons are required to decay in the NA62 "standard decay region". No kinematics selections are applied to the Monte Carlo sample.

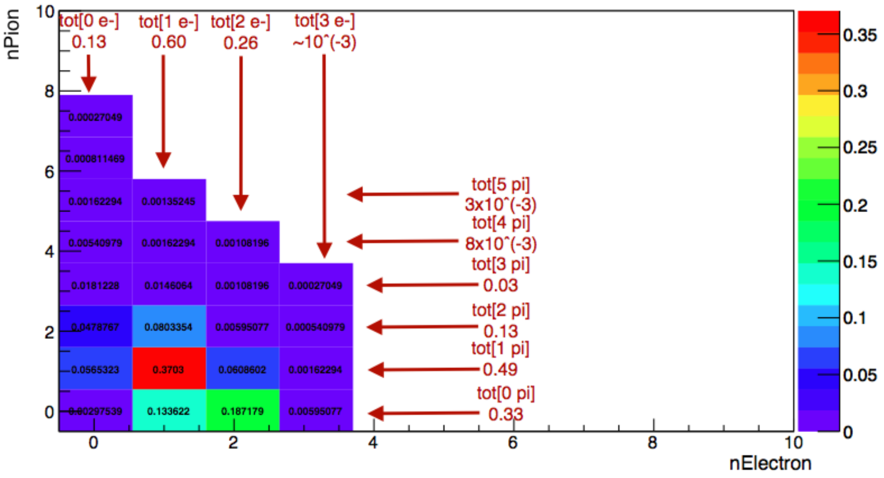

Figure 4.9: Fractions of reconstructed pions' rings vs number of reconstructed electrons' rings for a $K^+ \to \pi^+ e^+ e^-$ sample. The events have passed the L0 request, $\mathrm{R}_{10} \cdot \mathrm{Q}_X$, and the L1 spatial range cut.

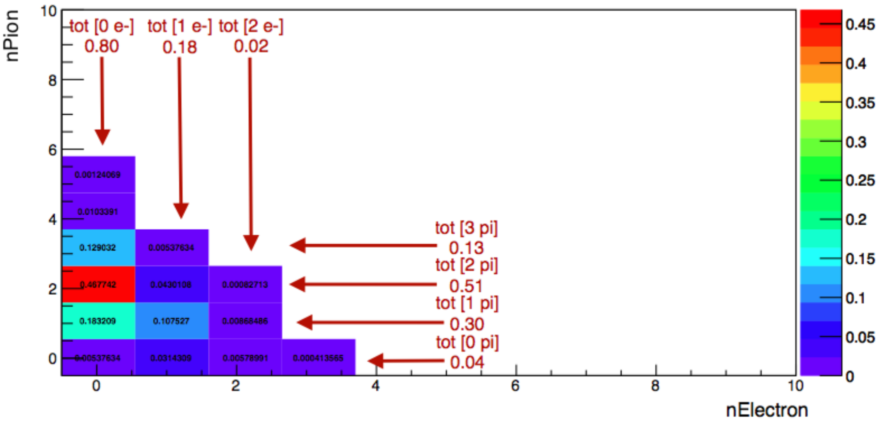

Figure 4.10: Fractions of reconstructed pions' rings vs number of reconstructed electrons' rings for a $K^+ \to \pi^+\pi^+\pi^-$ sample. The events have passed the L0 request, $R_{10}{\cdot}Q_X$, and the L1 spatial range cut.

From Figures 4.9 and 4.10, a powerful L1 trigger cut to select $K^+ \to \pi^+ e^+ e^-$ events is $N_{electron} > 0$ for which 80% of background is discarded while more than 80% of signal is kept. It is then necessary to develop an algorithm able to identify an electron Cherenkov-ring. The algorithm is required to have a fast execution time as it has to act as an online software trigger (for the execution time budget see Chapter 6). A new algorithm to identify an electron Cherenkov-ring detected by the NA62 RICH sub-detector is described in Chapter 5.

The rejection factor in discarding the $K^+ \to \pi^+\pi^+\pi^-$ decay after applying the $N_{electron} > 0$ L1 request on top of the L0 request, $\mathbf{R_{10}} \cdot \mathbf{Q_X}$, and on the spatial range cut is studied. Knowing the branching ratio of the $K^+ \to \pi^+\pi^+\pi^-$ (5.583%) [3], the total rate of kaon decays in the NA62 "standard decay region" (see relation in 4.1), and the fraction of background event in the signal region after the L0 and the L1 trigger cuts (0.20 from Figure 4.10), the total event rate for the $K^+ \to \pi^+\pi^+\pi^-$ decay is:

$$R(K^+ \to \pi^+\pi^+\pi^-) = 13.2\,\text{MHz} \times 0.05583 \times 0.20 = 0.15\ \text{MHz}. \qquad (4.5)$$

Comparing the new estimate of the event rate, 0.15 MHz, with the $K^+ \to \pi^+\pi^+\pi^-$

rate after the $\mathbf{R_{10}} \cdot \mathbf{Q_{\boldsymbol{X}}}$ request shown in table 4.1, 0.30 MHz, a rejection factor equal to 2 is obtained.

Chapter 5

A new RICH L1 trigger algorithm for electron identification

The existing offline RICH multi-ring reconstruction algorithm is too slow to act as an online L1 trigger, its efficiency is too low, and there is not any other existing RICH L1 trigger algorithm so far. For these reasons, a new algorithm for electron Cherenkov-ring identification using the RICH sub-detector is studied in the current work. The new algorithm is developed to act as an online L1 software trigger. It has to be fast with an execution time equal to ~ 450 μs (for the execution time constraints see chapter 6) and with a high signal efficiency. To perform efficiency studies of the new algorithm, the $K^+ \to \pi^+ e^+ e^-$ decay is chosen as signal. It is worth bearing in mind that one of the main source of background to multi-track decays is the $K^+ \to \pi^+ \pi^+ \pi^-$ decay with a total event rate of 0.30 MHz at the entrance of the L1 trigger stage (see chapter 4). A description of how the algorithm works is given in Section 5.1. Efficiency studies of the algorithm are described in detail in Section 5.2. Studies on the execution time of the algorithm are presented in Section 5.3. The electron-ring identification algorithm explained in this chapter can be applied in principle to select every decay with at least one electron Cherenkov-ring in the final state detected by the RICH detector.

5.1 The algorithm

The algorithm is developed to identify an electron Cherenkov-ring detected by the RICH. An electron Cherenkov-ring can be distinguished from a Cherenkov ring generated by another charged particle through the ring radius at a given momentum. The distribution of the reconstructed radii of the electron(blue line) and pion(red line) from a $K^+ \rightarrow e^+\nu$ and $K^+ \rightarrow \pi^+\nu\bar{\nu}$ Monte Carlo samples is shown in Figure 4.7 and it is proposed again in Figure 5.1.

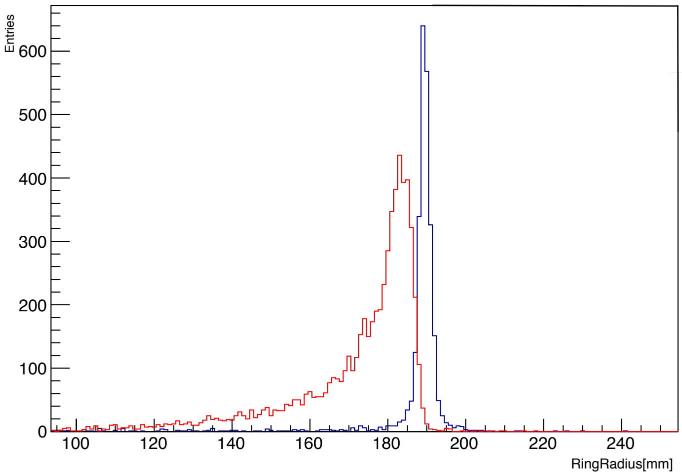

Figure 5.1: Distribution of the reconstructed ring radius of electron(blue) and pion(red) Cherenkov ring from a $K^+ \rightarrow e^+\nu$ and $K^+ \rightarrow \pi^+\nu\bar{\nu}$ sample, respectively.

The criteria to choose the optimal ring radius to identify an electron Cherenkov-ring are described in Section 5.2. A visual example of a Monte Carlo $K^+ \rightarrow \pi^+e^+e^-$ event detected by the RICH sub-detector is shown in Figure 5.2. The PMT hits are well visible. Two Cherenkov-rings in the RICH acceptance with a momentum over the Cherenkov threshold can be identified at first view.

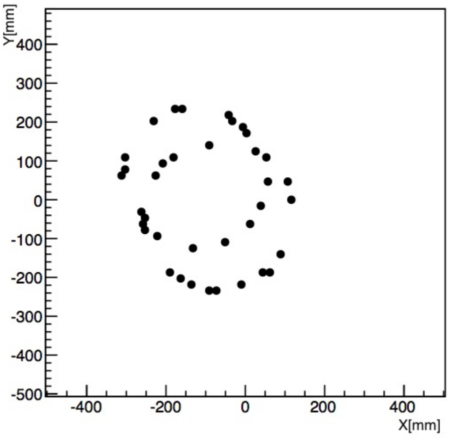

Figure 5.2: A Monte Carlo $K^+ \to \pi^+ e^+ e^-$ event detected by the RICH. The PMT hits are visible. Two Cherenkov-rings in the RICH acceptance can be identified at first view.

5.1.1 Preliminary consideration on the ring-centre identification

The algorithm aims to find the centre of the electron Cherenkov-ring. The centre of a circle is defined as the point inside the circle that is at an equal distance from all the points of the circle. The Cherenkov ring detected by the RICH is not a circle identified by a continuous line; it is a ring constituted of a discrete number of points represented by the PMT hits. Hence a discrete number of PMT hits are supposed to lie in a ring at a certain distance from the ring centre. The distance values belong to a fixed range, according to the particle generating the Cherenkov ring.

The ring centre may be located in a region that is wider than the RICH PMTs region as shown in Figure 5.3. The grid of the RICH PMTs and few hits, shown in red, belonging to the Cherenkov ring are visible. The black circle is the Cherenkov ring obtained from the Monte Carlo truth information while the blue circle is obtained from the official RICH-Reconstruction software. In this case, the reconstructed centre of the ring lies outside the RICH PMTs region.

The ring centre belongs to a continuous space and it does not coincide necessarily with a PMT position. The search area for the centre is chosen by looking at the

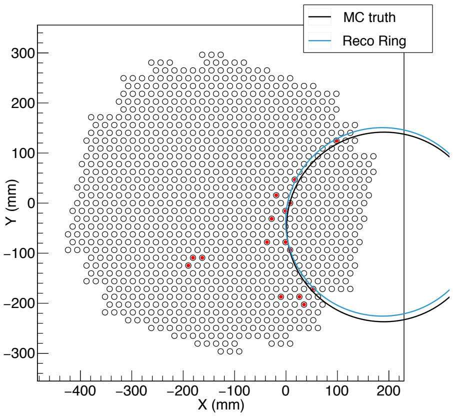

Figure 5.3: A Monte Carlo Cherenkov ring with part of it out of acceptance. The grid of PMTs with few hits in red belonging to the Cherenkov ring are visible. The black circle is the Cherenkov ring obtained from the Monte Carlo truth information while the blue circle is obtained from the official RICH-Reconstruction software.

distribution of the position of the reconstructed centres in a $K^+ \to \pi^+ e^+ e^-$ Monte Carlo sample. The optimal region is the one containing most of the reconstructed centres, see Section 5.1.5. The ring centre therefore must be searched for by a systematic method on a fixed region. A discrete grid of points is built on the chosen region to cover as many of the location of the centres as possible. A scan looking for the ring centre is applied on the grid: each point of the grid represents the potential centre of a Cherenkov ring. A finer granularity of the grid leads to a higher identification efficiency of the ring centre but it slows down the execution time of the algorithm. The choice of the granularity of the grid, i.e. the step of the scan, is a compromise between the efficiency of the signal and the execution time of the algorithm, which must be fast for operation as an L1 trigger.

5.1.2 First algorithm implementation

The algorithm performs a spatial scan over the x and y coordinates of the points placed on a two-dimensional lattice. The lattice does not necessarily coincide with the entire area of the RICH PMTs region. The distance along the x and y axes between two neighbouring points of the lattice, called lattice-step, is tuned to have a good efficiency. In order to find the centre of the electron Cherenkov-ring, for each lattice-point the algorithm computes the number of the PMT hits located at distance d, such that $R_{min} < d < R_{max}$, where R_{min} and R_{max} are the inner and the outer radius to be tuned according to the electron ring-radius distribution. A visual example of the lattice with a $K^+ \to \pi^+ e^+ e^-$ event superimposed is shown in Figure 5.4. The RICH PMT hits are shown in red. The blue arrows identify the outer R_{max} and the inner R_{min} radius of the electron Cherenkov-ring. The black arrows are a sketch of how the hit-scan algorithm works: it looks for the Cherenkov-ring centre computing the distance of each point of the lattice from each PMT hit. Each point of the grid represents a potential ring centre.

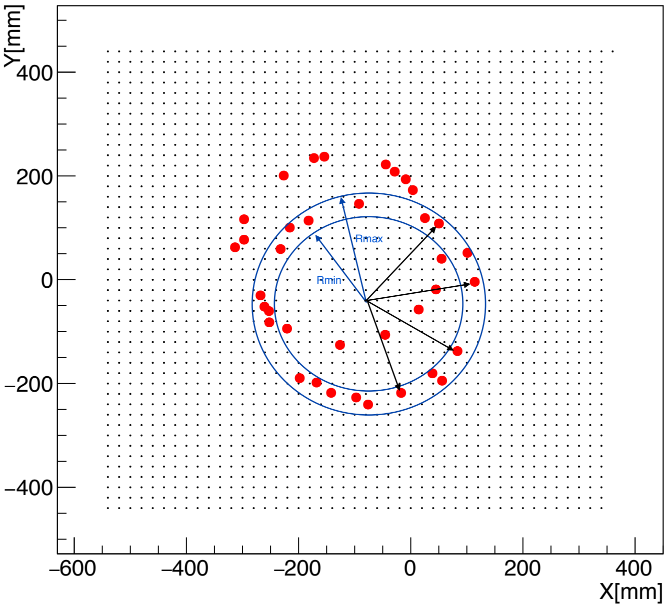

Figure 5.4: A two-dimensional lattice with a $K^+ \to \pi^+ e^+ e^-$ event superimposed. The RICH PMT hits are shown in red. The blue arrows identify the outer R_{max} and the inner R_{min} radius of the electron Cherenkov-ring. The black arrows are a sketch of how the hit-scan algorithm works: it looks for the Cherenkov-ring centre computing the distance of each point of the lattice from each PMT hit.

After scanning over all the lattice, the algorithm defines a point of the lattice as the centre of the Cherenkov-electron ring if it has collected the largest number of PMT hits, lying between the inner and the outer radius, with respect to all the other points of the lattice. This means that the algorithm is forced to scan over all the points of the two-dimensional lattice.

5.1.3 Improved algorithm implementation

In the first implementation of the algorithm, the scan is applied over all the points of the lattice. The centre is the point of the lattice that has collected the largest number of PMT hits. A first improvement on the implementation does not scan over all the points of the lattice. According to the new implementation, the algorithm finds an electron ring-centre if the number of the PMT hits collected by one lattice-point is equal to 10. The choice of the minimum number of PMT hits to be collected is due to the distribution of the number of the RICH PMT hits for an electron Cherenkov-ring as shown Figure 5.5. Requiring at least 10 PMT hits retains more than 80% of the electron Cherenkov-rings. The hit-scan algorithm is applied once to each event: if the algorithm finds one electron ring according to the procedure described above, the event is kept, otherwise it is discarded.

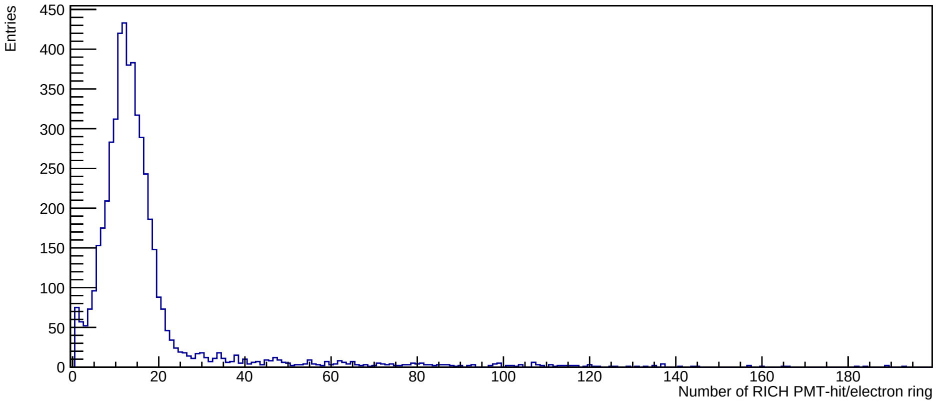

Figure 5.5: Distribution of the number of RICH PMT hits for a $K^+ \to e^+\nu$ decay.

5.1.4 General overview of the algorithm parameters

There are three main parameters of the algorithm that determine its efficiency and speed, as summarized below.

5.1.5 The area of the scan region

A first parameter of the hit-scan algorithm to be fixed is the area of the region over which the hit-scan is applied, i.e. the area of the two-dimensional lattice. This is the area where the algorithm looks for the electron Cherenkov-ring centre. One way to choose the area is to look at the distribution of the coordinates of the reconstructed Cherenkov-ring centres. The distribution of the centres of the reconstructed Cherenkov rings for a $K^+ \to \pi^+ e^+ e^-$ sample is shown in Figure 5.6. Each point represents the centre of one of the Cherenkov rings of the event. The centre coordinates are reconstructed by the NA62 RICH-Reconstruction software.

Two different scan-regions are taken into account as shown in Figure 5.6: a wide region within the red lines and an inner region within the blue lines [1]. The region of the PMT positions is located between the red and the blue region. The final choice of the region comes from efficiency and execution-time studies described in Section 5.2 and 5.3, respectively.

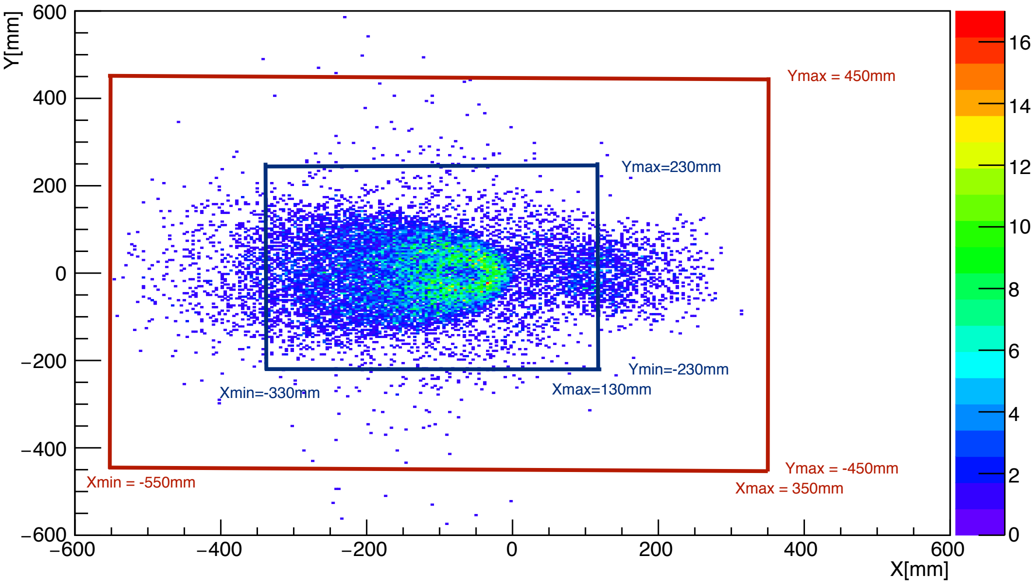

Figure 5.6: Coordinates of the Cherenkov-ring centres for a $K^+ \to \pi^+ e^+ e^-$ sample reconstructed by the NA62 RICH-Reconstruction software. Two regions where to apply the scan algorithm are considered.

---

[1] These regions are called wide-red and inner-blue regions along the text.

5.1.6 The lattice-step

Each point of the lattice is placed from the neighbour points at the same distance L (lattice-step) along the x and y direction. This distance is tuned in order to have an optimal algorithm efficiency. The efficiency of the algorithm, indeed, depends on the L parameter. This happens because the algorithm looks for the ring centre on a two-dimensional lattice that is discrete by definition, while the coordinates of the centre belong actually to a continuous space. A larger lattice-step means a higher loss in the identification of the ring-centre (see Section 5.2).

5.1.7 The paths

The algorithm can scan over the lattice according to different paths. There is not any a priori reason for which a particular path has to be chosen. Two different paths are studied: a rectangular and a spiral path. The efficiency of the algorithm does not depend on the path through which the algorithm scans over the lattice. The main difference between the two paths is the final execution-time of the algorithm.

The rectangular path

The rectangular path starts to scan over the lattice from the left-bottom corner and connects the lattice-points along the y axis, Figure 5.7. The starting point is pointed out by the red arrow. As soon as it reaches the top edge of the lattice, it starts again from the bottom edge. This means that the rectangular path connects all the points of the lattice not always with the same step-size.

The spiral path

The spiral path starts from the centre of the scan-region and connects the points according to a spiral, Figure 5.8. Unlike the rectangular path, the spiral path links all the points with the same step-size that is equal to the lattice-step. This means

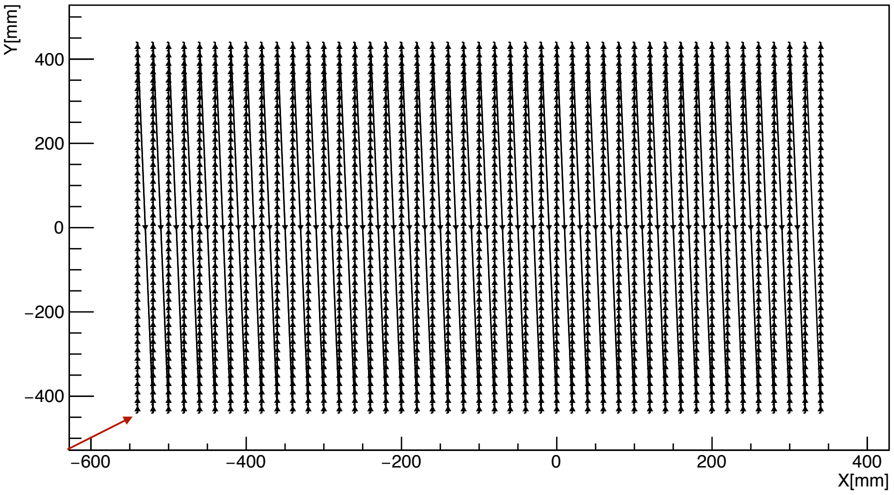

Figure 5.7: Rectangular path identified by arrows on the lattice. The starting point is pointed out by the red arrow.

that the distance between the PMT hit from a point of the lattice changes from one point to the neighbouring one by a maximum factor equal to the step-size. The maximum change in the distance is equal to the step-size and it is obtained if the points and the PMT hit are aligned as shown in Figure 5.8. This feature of the spiral path is important since it allows to implement an improvement to speed up the execution time of the algorithm, see Section 5.3.

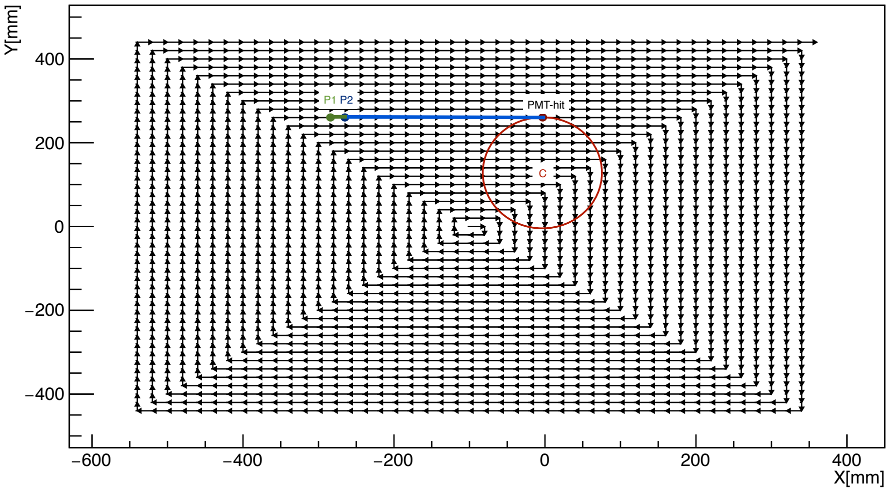

Figure 5.8: Spiral path identified by arrows on the lattice. The maximum change of the distance between two neighbour points P1 and P2 from one PMT hit is obtained if all the three points are aligned.

5.2 Efficiency studies

To select the electron ring it is important to fix an optimal range for the radius, i.e. R_{max} and R_{min}. According to the radius distribution in Figure 5.1, the value of the outer radius R_{max} for the electron Cherenkov-ring is set equal to 200 mm. In order to choose the value of the inner radius R_{min}, the efficiency of the hit-scan algorithm is tested with different values of the inner radius. The efficiency ϵ is computed as follows:

$$\epsilon = \frac{n}{N}, \tag{5.1}$$

where N is the total number of events passing the L0 trigger cut, i.e. $\mathrm{R}_{10} \cdot \mathrm{Q}_{\mathrm{X}}$ condition, and the L1 spatial-range trigger-cut, i.e. $\Delta X > 400$mm or $\Delta Y > 380$mm. The numerator n is the total number of events passing both the L0 and L1 spatial-range trigger-cut and the requirement of the hit-scan algorithm to find 10 PMT hits lying between the outer and inner radius of the electron ring. The error on the efficiency is:

$$\Delta\epsilon = \sqrt{\frac{\epsilon(1-\epsilon)}{\mathrm{N}}}. \tag{5.2}$$

The wide-red area of Figure 5.6 is studied with $L = 1$ mm. The fraction of background events is also analysed. The efficiency of the algorithm as a function of the inner radius is shown in red in Figure 5.9. The fraction of $K^+ \rightarrow \pi^+\pi^+\pi^-$ events is shown in black. The inner radius is chosen equal to 183 mm, for which the efficiency on the signal is the 87%, while $\sim$ 40% of background is kept. The inner and outer radii to identify an electron Cherenkov-ring are then:

$$\begin{aligned} R_{min} &= 183\,\text{mm}, \\ R_{max} &= 200\,\text{mm}. \end{aligned} \tag{5.3}$$

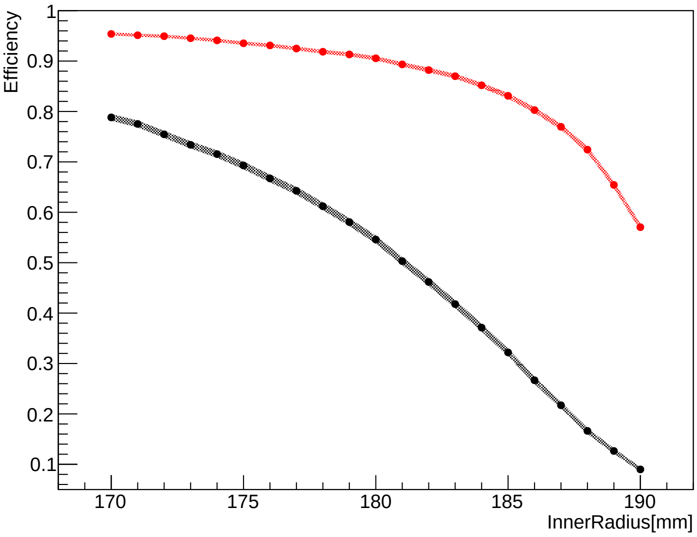

Figure 5.9: In red the efficiency of the algorithm in selecting the signal ($K^+ \rightarrow \pi^+ e^+ e^-$) as a function of the inner radius. In black the fraction of background ($K^+ \rightarrow \pi^+ \pi^+ \pi^-$) in the signal region. In both cases the error band is shown. The algorithm is applied with $L = 1$ mm. The outer radius is equal to 200 mm.

A visual representation of the electron-ring identification for a $K^+ \rightarrow \pi^+ e^+ e^-$ event using the hit-scan algorithm is shown in Figure 5.10: the blue(red) circle is the inner(outer) circle of the electron ring. More than 10 RICH PMT hits within the ring are collected.

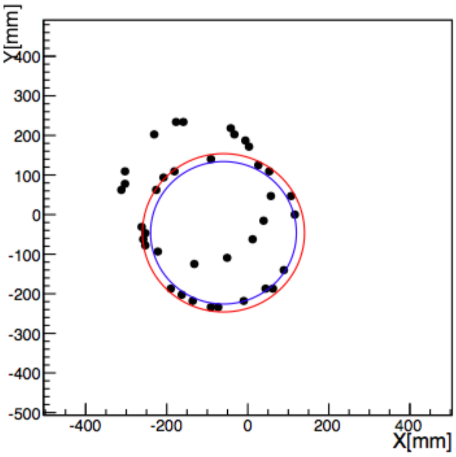

Figure 5.10: A $K^+ \rightarrow \pi^+ e^+ e^-$ event detected by the RICH. Two Cherenkov rings in the RICH acceptance are visible. The two circles identify the electron Cherenkov-ring after applying the hit-scan algorithm.

The next parameter of the hit-scan algorithm to be fixed is the distance on the x and y direction between two neighbour points of the lattice, i.e. the lattice-step. The efficiency as a function of different lattice-step is shown in Figure 5.11. The efficiency and the error are computed as defined in 5.1 and 5.2, respectively. For these studies, the lattice covers an area equal to the wide-red region shown in Figure 5.6. The values of the inner and outer radii are set as in 5.3. Looking at Figure 5.11, a lattice-step equal to 6 mm is chosen as it leads to an efficiency of 82%.

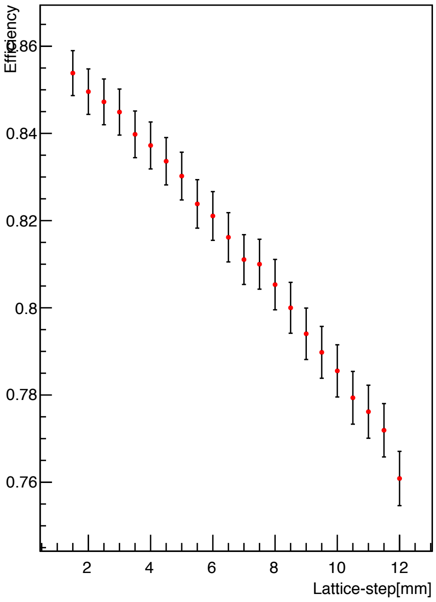

Figure 5.11: Efficiency of the algorithm in selecting a $K^+ \to \pi^+ e^+ e^-$ decay as a function of the lattice-step. It is worth to note that the errors are correlated between different lattice-step sizes.

The last parameter to set is the area of the region over which the lattice is built. The efficiency as a function of the number of the lattice-points is shown in Figure 5.12. A spiral path starting from the centre of the wide-red region is applied on the lattice, Figure 5.6. The wide-red region is covered by roughly 23000 lattice-points with a lattice-step of 6 mm. After scanning $\sim$ 6000 lattice-points the efficiency is roughly constant at 82%, while the fraction of $K^+ \to \pi^+ \pi^+ \pi^-$ events is 31%. A spiral path, connecting $\sim$ 6000 lattice-points with a lattice-step of 6 mm, covers the whole area identified by the inner-blue region in Figure 5.6.

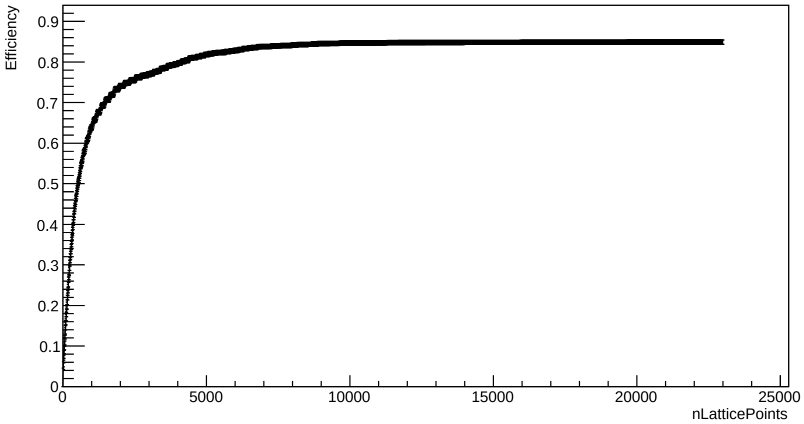

Figure 5.12: Efficiency of the algorithm in selecting a $K^+ \rightarrow \pi^+ e^+ e^-$ decay as a function of the number of the lattice-points. A spiral path is applied on the lattice with a lattice-step of 6 mm.

In conclusion, after the considerations on the efficiency, all the parameters of the hit-scan algorithm are set. The final values of the parameters are summarized in table 5.1.

Electron Cherenkov-ring Inner Radius	183 mm
Electron Cherenkov-ring Outer Radius	200 mm
Lattice-step	6 mm
Number of lattice points	5930

Table 5.1: Parameters of the hit-scan algorithm to identify an electron Cherenkov-ring.

5.3 Execution time studies

Since the hit-scan algorithm is studied to run as an online software trigger, it has to satisfy the execution time constraints. In particular, considering a mean rate of 1 MHz from the L0 trigger stage, the events are distributed among 30 PCs of the PC-farm. Each PC works in multi-threading mode that means they can run more than one process in parallel. Considering 15 threads for each PC, the time budget available to process one event at L1 stage is:

$$1/1\,\mathrm{MHz} \times 30\mathrm{PCs} \times 15\,\mathrm{threads} = 450\,\mu\mathrm{s}. \tag{5.4}$$

In this section several improvements on the implementation are described to make the algorithm as fast as possible.

The measurement of the execution time of the algorithm is performed using a function provided by the Linux system[2]. The function allows us to put several time counters along the code. Putting two counters at the beginning and at the end of the code and subtracting the last time-counter from the first one, the execution time of the code is then obtained. The code is always run on the same machine on lxplus at CERN. However, this approach gives an approximate value of the running time since it may be subject to effects caused by other users logged on the lxplus machine. It would be better to run the algorithm on a dedicated machine for any further time-studies. The execution time studies are performed on a $K^+ \to \pi^+\pi^+\pi^-$ Monte Carlo sample.

The efficiency of the algorithm is always checked after each time improvement implementation and it has to remain constant.

5.3.1 Execution time shape

Before analysing the mean value of the execution time, studies on the behaviour of the execution time are performed. The execution time t depends linearly on the number of the total PMT hits per event (NHits) and it scales with the inverse square of the lattice-step, called Δ. This is because the algorithm scans over a square[3]

---

[2] For Unix or Linux based system the function to evaluate the execution time of the algorithm is *gettimeofday()*. This function is declared in "sys/time.h".

[3] If the region were rectangular, the considerations would be the same.

lattice with points placed at the same distance on the x and y direction:

$$t(\Delta) = f(\frac{1}{\Delta^2}) \cdot \mathrm{NHits} + \mathrm{const}$$
$$f(\frac{1}{\Delta^2}) = t(\Delta)/\mathrm{NHits} + \mathrm{const}, \tag{5.5}$$

where $f(\frac{1}{\Delta^2})$ is a function of Δ^{-2}. If the relation 5.5 is valid, a hyperbolic behaviour of the execution time as a function of the lattice-step should be visible. The hit-scan algorithm is applied on several lattices with different lattice-steps. The rectangular path is used. The execution time per PMT hit as a function of lattice-step Δ is shown in Figure 5.13. A fit is superimposed with the following function:

$$f(\Delta) = \frac{\mathrm{p}_0}{\Delta^2} + \mathrm{p}_1, \tag{5.6}$$

where p_0 and p_1 are two constants. In particular the p_1 constant is compatible with zero from the fit results. It is possible to conclude that the execution time of the algorithm has a linear-dependence on the number of PMT hits and a hyperbolic behaviour with the lattice-step as expected.

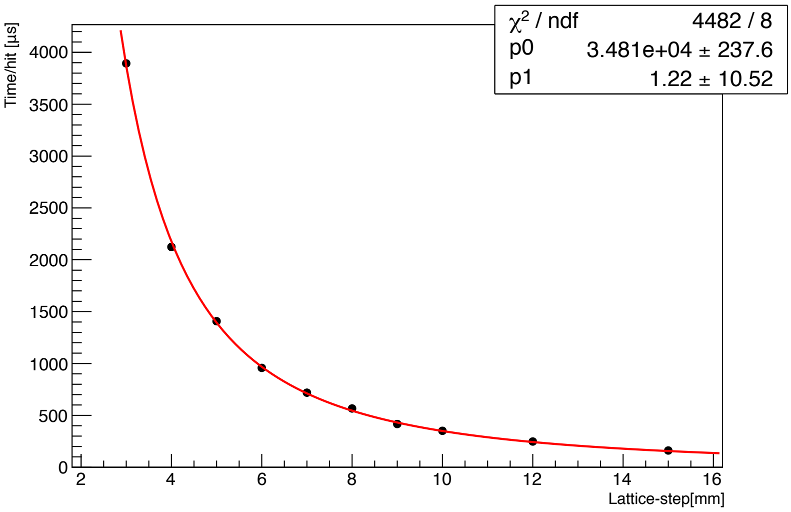

Figure 5.13: Execution time of the algorithm per PMT hit as a function of the lattice-step Δ with an hyperbolic fit superimposed. The rectangular path is applied.

The execution time per PMT hit as a function of the total number of lattice-points is shown in Figure 5.14. From this plot it is possible to state that the execution time per PMT hit per lattice-point is constant and equal to 0.1 μs.

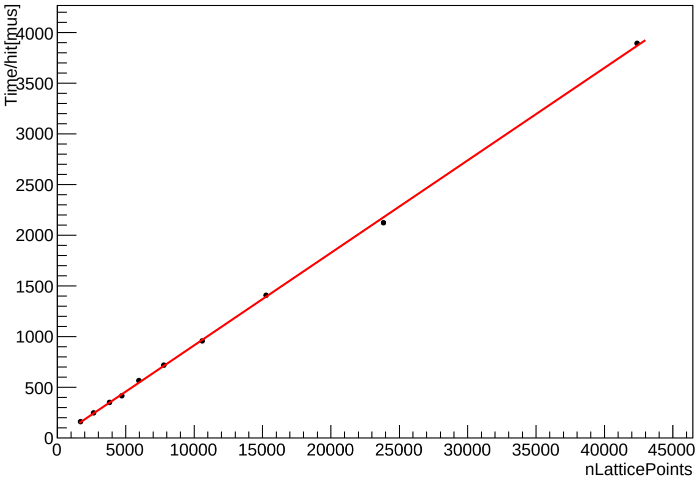

Figure 5.14: Execution time of the algorithm per PMT hit as a function of the number of lattice-points with a linear fit superimposed. The rectangular path is applied.

5.3.2 A first execution-time improvement

A first execution-time improvement consists in stopping the hit-scan algorithm as soon as it collects 10 PMT hits within the range of the scan (*first improvement*). A $K^+ \rightarrow \pi^+\pi^+\pi^-$ Monte Carlo sample is chosen to perform studies on the execution time of the algorithm. In this case the hit-scan algorithm should not identify any electron ring. This implies that the algorithm is forced to compute all the distances of the PMT hits from all the 5930 points of the lattice. It means more computational operations than when the algorithm is stopped as soon as it collects 10 PMT hits. This is a scenario closest to the reality since the $K^+ \rightarrow \pi^+\pi^+\pi^-$ is one of the dominant source of background to multi-track decays. Hence studies on the execution time are performed with the $K^+ \rightarrow \pi^+\pi^+\pi^-$ sample for which the algorithm is slower.

The rectangular path and the spiral path are now compared. The algorithm is applied over a lattice covering the wide-red region in Figure 5.6. The mean value of the execution time after the *first improvement* as a function of the lattice-step is shown in Figure 5.15 for the rectangular path (left) and the spiral path (right).

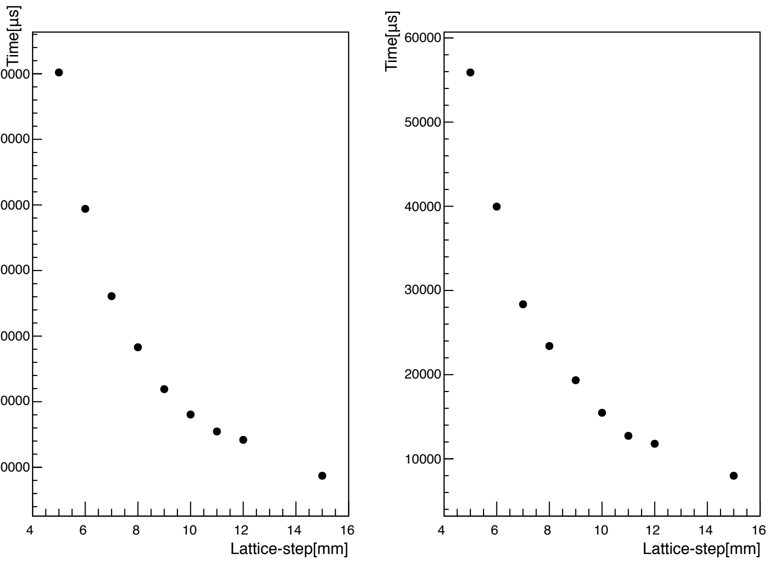

Figure 5.15: On the left-hand side(right-hand side) the mean value of the execution time as a function of the lattice-step is shown for the rectangular(spiral) path. The result is obtained after the *first improvement*.

An improvement factor of 1.3 on the execution time, with lattice-step of 6 mm, is gained moving from the rectangular path to the spiral path. One important difference between the two paths is that the spiral path starts from the centre of the square lattice, where most part of the ring-centres are concentrated, see Figure 5.6. Unlike the spiral path, the rectangular path starts from the bottom-left corner of the lattice that is less populated. If the scan starts where most part of the ring-centres are concentrated, there is a faster identification of the ring-centre in that region and more computational time is saved. This justifies the time-improvement factor between the two paths. The spiral path is then chosen to scan over the lattice. The choice of the lattice-step equal to 6 mm is a good compromise between the efficiency, Figure 5.11, and the execution time in Figure 5.15 on the right.

As already demonstrated, the efficiency of the algorithm is roughly constant after scanning $\sim$ 6000 lattice-point, see Figure 5.12. The inner-blue region in Figure 5.6, corresponding to 5930 lattice-points with a lattice-step of 6 mm, is then chosen as the best region over which the lattice is built. It is interesting to analyse the execution time improvement moving from a scan over the wide-red region in Figure 5.16, to the inner-blue region Figure 5.17. An improvement factor of 3.7 on the mean execution time, with lattice step of 6 mm, is achieved between the two scanned-regions.

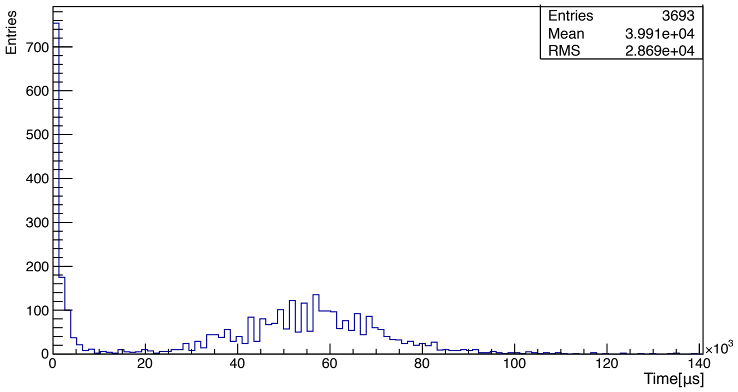

Figure 5.16: Execution time of the hit-scan algorithm per event applied over the wide region after the *first improvement.* A $K^+ \to \pi^+\pi^+\pi^-$ sample is used.

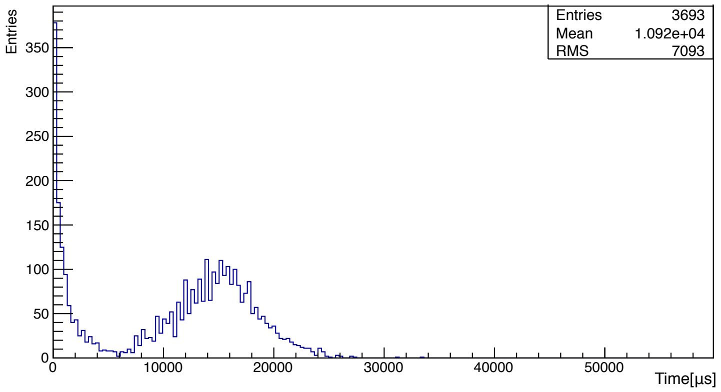

Figure 5.17: Execution time of the hit-scan algorithm per event applied over the inner region after the *first improvement.* A $K^+ \to \pi^+\pi^+\pi^-$ sample is used.

Looking at the time distribution in Figures 5.16 and 5.17 two components are visible: a fast and a slow component. The fast component is when the scan finds the ring-centre after few operations, i.e. it does not scan over all the points of the lattice, according to the *first improvement.* The slow component is because the algorithm does not find the electron ring-centre after few computations and it is forced to scan over all the $\sim$ 6000 points of the lattice. In this case the slow component is the result of a correct operating-mode of the algorithm on a $K^+ \to \pi^+\pi^+\pi^-$ sample. In fact, the algorithm should not have to find an electron Cherenkov-ring-centre in a $K^+ \to \pi^+\pi^+\pi^-$ sample.

Focusing on the slow component of both of the execution time distributions, an improvement factor of 3.8 on the mean time is achieved. The execution time of the hit-scan algorithm for those events where the ring-centre is not found is shown in Figures 5.18 and 5.19 for the wide and inner region, respectively. In principle, the execution time scales with the number of the scanned lattice-points. Knowing that the wide region is covered by $\sim$ 23000 points (NStepsWide), while the inner region by $\sim$ 6000 points(NStepInner), it results that:

$$\frac{\text{NStepWide}}{\text{NStepInner}} = \frac{23000}{6000} = 3.8. \tag{5.7}$$

Considering the mean-times of the distributions in Figures 5.18 and 5.19, their ratio, that is 3.8, confirms that the execution time scales with the total number of scanned lattice-points.

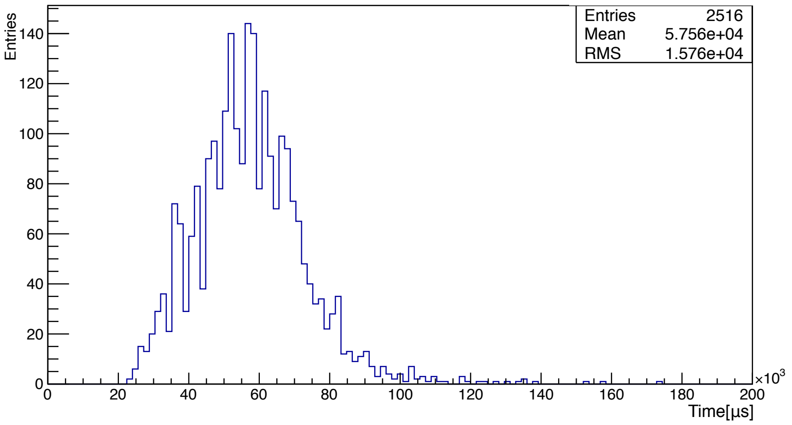

Figure 5.18: Execution time of the hit-scan algorithm for those events where the ring-centre is not found after the *first improvement*. The scan is applied on the wide region.

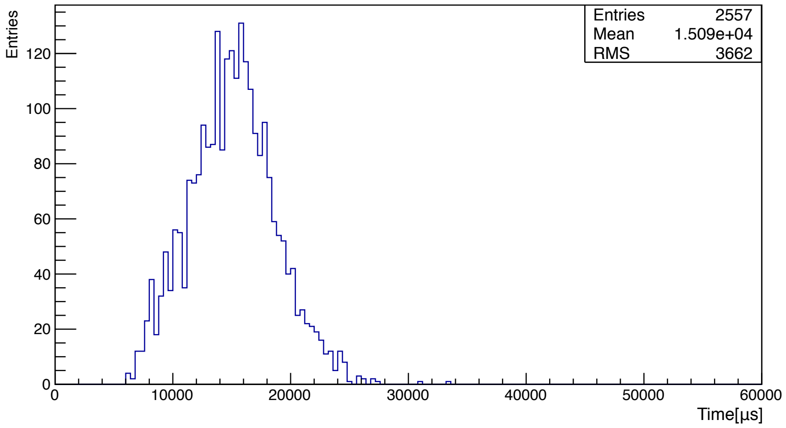

Figure 5.19: Execution time of the hit-scan algorithm for those events where the ring-centre is not found after the *first improvement*. The scan is applied on the inner region.

Focusing now on the spiral path applied on the lattice built in the inner region, the execution time as a function of the number of the PMT hits (NHits) is shown in Figure 5.20. This is a proof that the time depends linearly on the number of the PMT hits. The fast and a slow component of the time are visible.

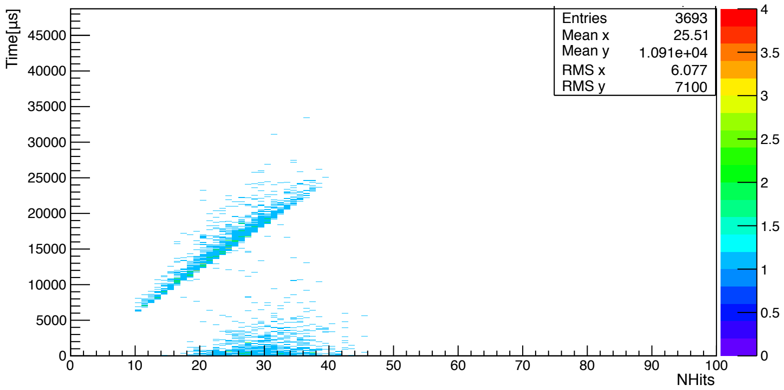

Figure 5.20: Execution time of the hit-scan algorithm as a function of the number of PMT hits after the *first improvement*. The spiral path is applied on the inner region. The lattice is built with a lattice-step of 6 mm.

The execution time as a function of the number of the scanned lattice-points is shown in Figure 5.21. A slow component is visible also here at 5930 lattice-points that corresponds to the total number of points on the lattice. The slow component is due, as already explained, to the failure of the algorithm in identifying an electron Cherenkov-ring centre. In this case all the points of the lattice are scanned, i.e. 5930 points as confirmed by Figure 5.21.

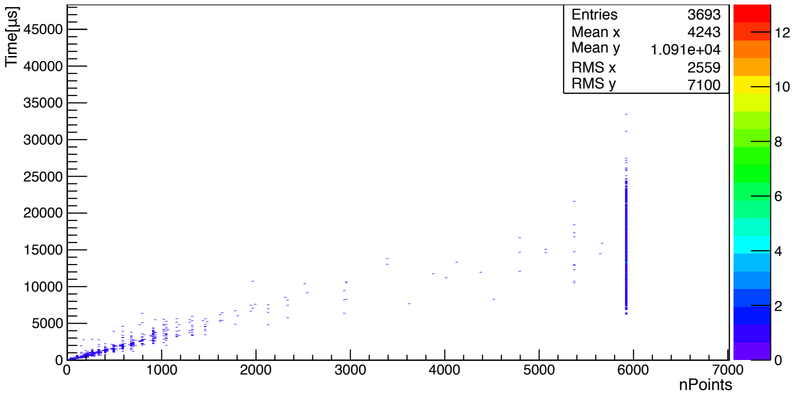

Figure 5.21: Execution time as a function of the number of the lattice-points after the *first improvement*. The spiral path is applied on the inner region. The lattice is built with a lattice-step of 6 mm.

5.3.3 A second and third execution-time improvements

As already mentioned, the main feature of the spiral path is that the distance d of two neighbour points of the lattice from a PMT hit does not change more than the lattice-step, see Figure 5.4. Hence knowing the distance of a lattice-point from a PMT hit, the distance at the next point can not change more than the lattice-step. This is an important feature that allows us to avoid useless distance computation. For instance, a distance d larger than the value of the outer radius R_{max} is considered. Computing the difference between the distance d and the outer radius R_{max}, dividing it by the step-size, the lattice-point N at which the distance d from the same PMT hit can be computed again is given (*second improvement*). This means that for all the previous N-1 lattice-points the distance d is larger than the outer radius and the distance computation can be avoid. If the distance d at N lattice-point is still larger than R_{max}, the procedure is applied again until the distance d is smaller than R_{max}. The number N is computed for each point of the lattice for each PMT hit. The same procedure is applied if the distance d is less than the inner radius R_{min} (*third improvement*). The two conditions are exclusive: the PMT hit lies either outside the outer circle or inside the inner circle. Applying the *second improvement* on top of the *first improvement*, the execution time as a function of the number of PMT hit is shown in Figure 5.22. A double component of the execution time is also visible here. Comparing the mean values of the execution time, an improvement factor of 1.7 is achieved. The execution time as a function of the number of PMT hit after the *third improvement* on top of the previous two is shown in Figure 5.23. An improvement factor of 1.8 is obtained from the *second improvement* to the *third improvement*. A total improvement factor of 3.2 between the *first* and the *third improvement*.

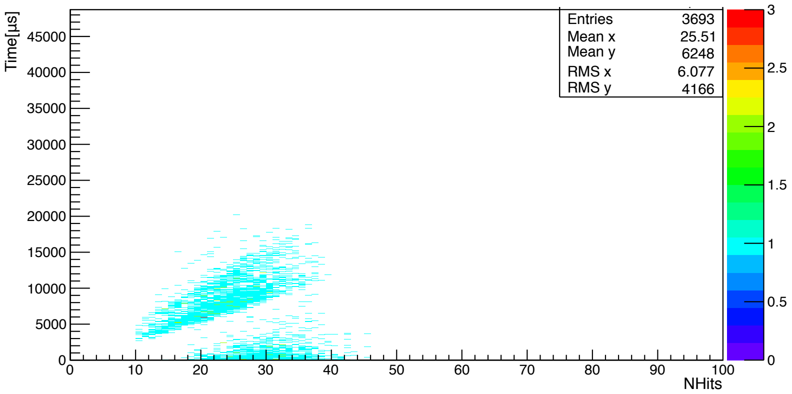

Figure 5.22: Execution time as a function of the number of PMT hits after the *second improvement*. The spiral path is applied on the inner region. The lattice is built with a lattice-step of 6 mm.

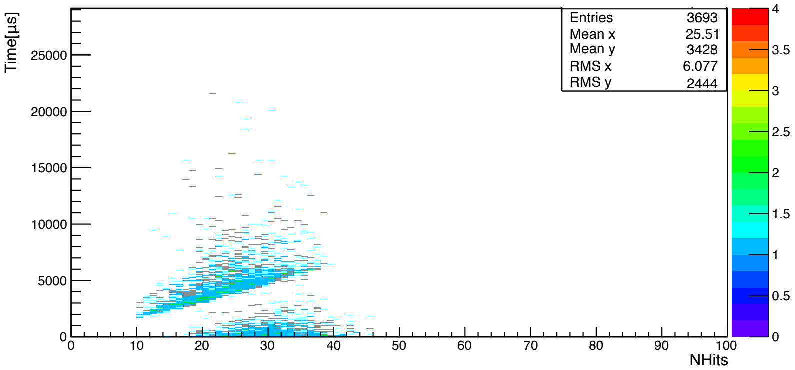

Figure 5.23: Execution time as a function of the number of PMT hits after the *third improvement*. The spiral path is applied on the inner region. The lattice is built with a lattice-step of 6 mm.

5.3.4 Further improvements

The positions of the lattice points are stored in a look-up table: the algorithm then can read directly the coordinates of the points from the look-up table. For a further time-improvement, another look-up table containing more information on the lattice-points is built as follows. For each point of the lattice, moving over it through a spiral path, the direction and the number of the following points before changing direction are known. Figure 5.24 shows a lattice with the spiral path on it: on each point of the lattice the direction along which the spiral is moving and the number of the following points before changing direction are written.

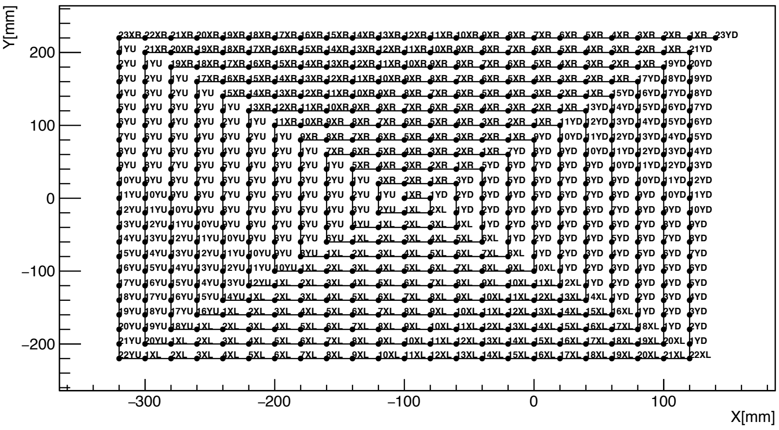

Figure 5.24: The spiral path on a lattice. For each point the number of the following points before changing direction is shown. The first number is the number of the following points in the X or Y direction, moving right(R)/left(L) or up(U)/down(D) respectively.

At the starting point of the spiral, the x-component, ΔX, and the y-component, ΔY, of the distance are computed for each PMT hit. The following points before changing direction are read from the look-up table. Hence, if $\Delta X(\Delta Y)$ is larger than the outer radius R_{max}, the computation of the distance for that PMT hit for the following points if moving in the $y(x)$ direction is avoided. This is because the $\Delta X(\Delta Y)$ does not change moving along the $y(x)$ direction. This procedure is applied until ΔX or ΔY is less than R_{max}. In this new scenario, as soon as either ΔX or ΔY component is less than R_{max}, the previous *second* and the *third improvement* are applied. The new execution time as a function of the number of PMT-hits is shown in Figure 5.25. An improvement factor of 1.7 is achieved if the mean values of the distributions in figure 5.23 and 5.25 are compared.

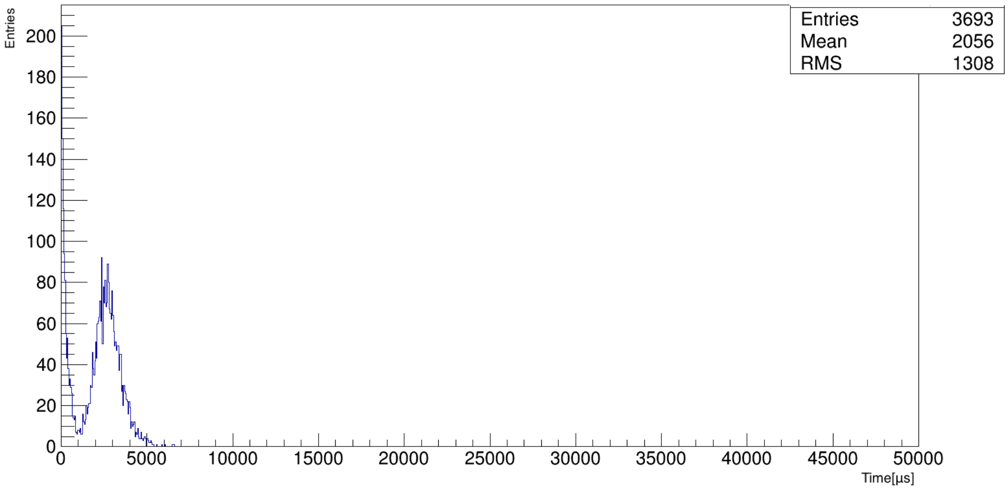

Figure 5.25: The execution time as a function of the number of PMT hit. The results is obtained after taking into account the direction-information of the spiral path at each lattice-point.

A last execution time improvement is studied. The idea is to compute the distance of each RICH PMT position from each lattice-point before applying the hit-scan algorithm. The positions of the RICH PMTs are read from a configuration file. Having 1952 PMTs and 5930 lattice-points, more than ten-million distances are computed. If the distance is within the inner and outer radius, a boolean equal to 1 is stored in a look-up table, otherwise it is set to 0. The algorithm does not compute any distance online. It reads directly from the look-up table for each lattice-point and for each PMT-hit if the distance is acceptable or not. In this new implementation no additional operations are foreseen, it consists only in reading values from a look-up table with more than ten-million entries. The execution time after the new improvement is shown in Figure 5.26. The results is not improved from the previous one. It is also slower from the execution time estimation in Figure 5.25. Actually it is not possible to state if it is really a worst result or it is just a fluctuation in the time measurement. It is noticed that the time measurement on the lxplus machine depends strongly on the number of users working on that machine at the same time. A quantitative estimation of the contribution of the fluctuations to the real time measurement is not performed. The result demonstrates that reading the information from a look-up table with more than ten million entries does not improve the execution time of the algorithm.

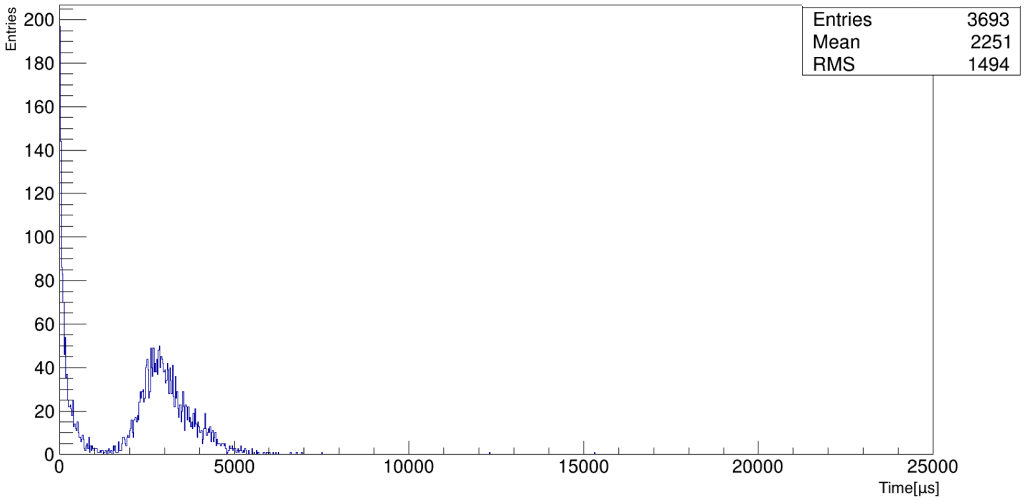

Figure 5.26: Execution time after reading from the look-up table.

In conclusion, the mean-value of the execution time of the algorithm is above 2 ms and the looking-up table improvement may be fastest. A total improvement factor of 5.3 on the execution time is achieved after several time-improvement implementations. However, a dedicated machine where to run the algorithm is needed for timing studies. It is worth to remind that the mean value for the execution time of a L1 trigger algorithm is 450 μs and then the hit-scan algorithm is too slow to run as an online software trigger. Further improvements on the execution time are needed.

Chapter 6

The PC-farm and the L1 trigger algorithms

6.1 The NA62 PC-farm

The NA62 PC-farm framework is the interface between the raw data produced by the readout boards of the sub-detectors, the online software trigger algorithms, the PC data storage (PC-merger) located at the experiment and at the main data centre at CERN. Some of the main projects of the NA62 PC-farm framework are listed below:

- na62-farm-lib (static library);
- na62-farm-lib-networking (static library);
- na62-trigger-algorithms;
- na62-farm;
- na62-merger;
- na62-farm-dim-interface.

The na62-farm-lib is a static library used by all other software components. It stores all data types for the communications protocols and useful helper classes. The na62-farm-lib-networking is used by the projects adopting PF_RING (a type of network socket) for network communications [61]. The na62-trigger algorithms project is the part of the framework containing all the algorithms of the higher-level trigger. The higher-level trigger consists of two stages: the L1 and L2 trigger. A first cut on the trigger rate is applied by the algorithms acting at L1 trigger stage. A further rejection factor on the trigger rate is achieved by the algorithms implemented at the L2 trigger stage where a better reconstruction of the events, with respect to the L1 trigger stage, is performed. Each L1 algorithm uses information from single sub-detector.

The L1 trigger algorithm using information from the RICH sub-detector, has been implemented by me on the NA62 PC-farm.

The L1 trigger algorithms are executed with all data sent by all sub-detectors except the Liquid Krypton calorimeter. The result of the L1 is an 8-bit word that is the L1 trigger type word. In each bit of the L1 trigger type word the verdict from each sub-detector algorithm is stored. If the event is accepted at L1 stage, the remaining data from the Liquid Krypton calorimeter is requested and the L2 algorithms are executed. The result of the L2 trigger algorithms is a 8-bit word representing the L2 trigger type word. If the event is accepted at L2 stage, it will be sent to the PC-merger.

The na62-farm is the main program running on the PC-farm machines. This program links the processes of the na62-farm-lib, na62-farm-lib-networking and na62-trigger-algorithms projects. Raw data are received in Multi Event Packets (MEPs) format. A variable number of events from each sub-detector data acquisition board are collected into a single MEP and then sent to the acquisition PC-farm. The number of events in any MEP ("MEP factor") can vary between sub-detectors. The PC-farm also processes the trigger algorithms and sends the events to the PC-merger. The na62-merger is the main program running on the PC-merger. It receives the accepted events from the PC-farm, generates files with all the events within a burst and stores the files on the local disk buffer. The maximum output data rate of the PC-merger is limited by the network (10 Gb/s) and by the writing speed at the data centre (about 200 MB/s). Given the size of data packet expected at NA62, this translates into a maximum output rate of 20 kHz.

To distribute status updates of all components within the NA62 experiment, the communication system DIM[1] is used. The na62-farm-dim-interface is linked with both na62-farm and na62-merger projects. In this way the PC-farm and the PC-merger can send and receive status updates during the NA62 data taking.

6.1.1 Data flow and format

After a positive L0 trigger has been processed within the readout hardware, all sub-detectors send the raw data of the accepted event in MEP format to the PC-farm. As the sub-detectors have several readout boards and the number of readout boards is fixed for every sub-detector, the PC-farm waits until it receives data from all readout boards (each board being defined by a unique source ID). This process is called *event building*. As soon as an event is complete, the L1 trigger algorithms can be executed with the built event. Raw data coming from the sub-detectors are decoded by a specific online class implemented within the na62-trigger-algorithms project before the L1 trigger algorithms can be applied.

The MEP format received by the PC-farm is represented in Figure 6.1. This consists of a series of aligned 32-bit words containing sub-detector specific information. The number of bits for each word is indicated at the bottom of the data format.

The "Source ID" stored in the MEP header word is an 8-bit identifier specifying the sub-detector which has sent the data. The following "First event number" is a 24-bit word storing the event number of the first event in the MEP. The event number and the burst ID information uniquely identify the event. The burst or spill

---

[1] Distributed Information Management System providing a network inter-process communication layer.

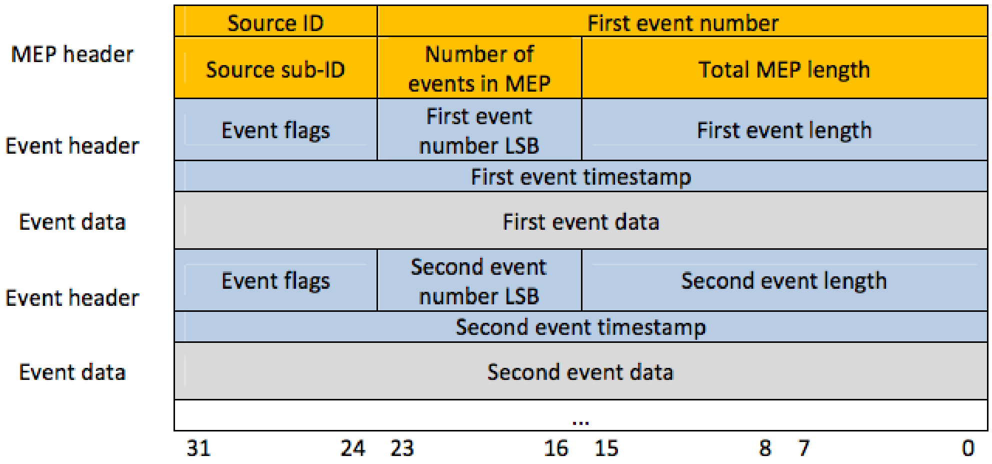

Figure 6.1: The MEP format arriving at the PC-farm [62].

is the period of the SPS beam-delivery cycle. The duration can vary between 1-20 s and during each run is roughly constant. A burst represents the basic data-taking time unit, it means that the event numbering is relative to a burst and restarts from the beginning again at each new burst. The "source sub-ID" is an 8-bit identifier specifying the individual readout board of the sub-detector. Two readout boards of the same sub-detector do not have the same source sub-ID. During the 2015 run the number of events stored in a MEP was varied between one and eight. The "Total MEP length" indicates the total length of the MEP in bytes including the MEP header.

After the MEP header, the event header and data words are encountered. The "Event flags" in the header is an 8-bit word not yet filled with the exception for the bit 7 that is set only for the end of burst event. The "Event number Least Significant Bit (LSB)" represents the least significant 8-bit of the event number. The "first event length" is the length of the following event data in bytes including the event header itself. The "First event time-stamp" is a 32-bit word relative to which all the times of the individual channel are interpreted. The event data block stores the raw data coming directly from the readout board of each sub-detectors. The event data block for the TEL62-based sub-detector is shown in Figure 6.2 . The board header word contains the "Format" that is a 8-bit word identifying the version of

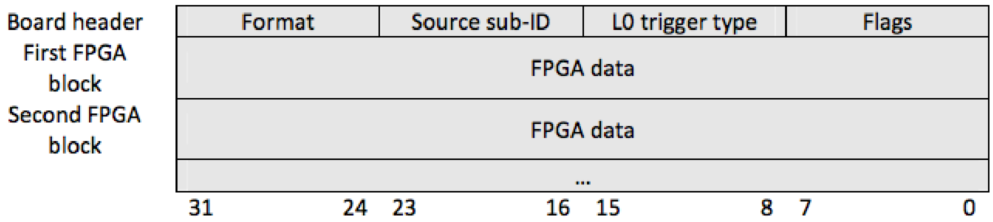

Board header	Format	Source sub-ID	L0 trigger type	Flags
First FPGA block	FPGA data			
Second FPGA block	FPGA data			
	...			
	31 24	23 16	15 8	7 0

Figure 6.2: The Event data block for the TEL62-based sub-detectors [62].

data format. The "Source sub-ID" is the readout board identifier (in this case the TEL62) of the sub-detector (the same as the word present in the MEP header). The "L0 trigger type" is an 8-bit word defined by the L0 Trigger Processor (L0TP) by analysing the L0 trigger primitives. The "Flags" word in FPGA indicates which FPGA data sub-blocks are present. Each TEL62 can be equipped with up to four FPGAs. These four FPGAs sub-blocks may be present. The structure of the FPGA data sub-block is shown in Figure 6.3. This contains the FPGA header and data words, which are structured in time-slots.

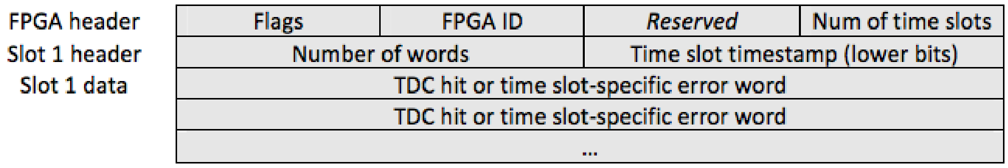

FPGA header	Flags	FPGA ID	*Reserved*	Num of time slots
Slot 1 header	Number of words		Time slot timestamp (lower bits)	
Slot 1 data	TDC hit or time slot-specific error word			
	TDC hit or time slot-specific error word			
	...			

Figure 6.3: The FPGA data block [62].

The "Flags" word in the FPGA header indicates the presence of an error after the time slot data. The "FPGA ID" identifies the FPGA, numbers from 0 to 3 identify the PP-FPGA (Pre-Processing FPGA), while 4 is used for the SL-FPGA (SyncLink FPGA). Each FPGA contains a fixed number of 25 ns slots in which data are stored. The header of each slot contains the number of 32-bit words stored in the time-slot, including the header word itself and the lower 16 bits of the time slot timestamp.

The data of each slot correspond to the TDC word encoding the TDC hit information and to the error word in case time-slot specific error might have occurred during the data acquisition. The TDC word stores the hit time information from each readout channel and it is shown in Figure 6.4. The "ID" indicates if the time is the leading or the trailing edge of the hit. The "TDC" and "Chan" identify the TDC and the TDC-channel. The time information is stored in the 19 least significant bits.

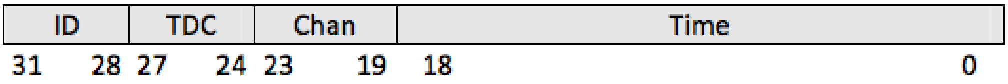

Figure 6.4: The TDC data word [62].

As mentioned before, an online decoder is implemented to read data from each specific sub-detector readout system. For instance, the decoder for the TEL62 board reads all the information stored in the MEP packet, Figure 6.1. It decodes the information and then it stores them in some variables ready to be used by each sub-detector trigger algorithms.

6.2 L1 and L2 software triggers

The maximum event rate produced by the L0 trigger is 1 MHz and further event rate reduction is required from the L1 and L2 software triggers in order to match the available bandwidth for the permanent storage of data (20 kHz). To do that, two logical levels of software triggers are available in the NA62 trigger and data acquisition (TDAQ) system (see Chapter 2):

- the L1 trigger receives raw data of L0 accepted events at 1 MHz rate and it has to provide a reduction factor of 10 to the event rate;
- the L2 trigger processes data from events accepted at L1 at 100 kHz rate and relies on partially reconstructed events. Complex correlations between information from different sub-detectors can be exploited at this level to ensure a further reduction factor of 10 to the event rate.

As part of online data processing the implementation of the L1 and L2 software triggers is optimized so that the minimum CPU processing time is used. The integrated available time budget for L1-L2 trigger algorithms can be estimated by considering the L1 input rate (1 MHz) distributed over 30 PCs with multi-threading capabilities. When considering about 15 effective cores, then the available time budget adds up to 450 μs:

$$1/1\ \text{MHz} \times 30\text{PCs} \times 15 = 450\ \mu\text{s}. \tag{6.1}$$

In reality this time budget can be stretched out by considering the out-of-burst time, which is the time passing between the End Of Burst (EOB) signal and the next Start Of Burst (SOB) signal. This is because after the EOB signal the PC-farm has received all events within a burst and part of the out-of-burst time can be addressed for processing the L1 and L2 trigger algorithms if needed. Nevertheless, it is not possible to foresee the portion of the out-of-burst time available to the L1 and L2 trigger stages because this might vary with the running conditions.

It is desirable to achieve a L1-L2 trigger system that is both powerful and flexible at the same time. This allows us to have several physics programs to be pursued during the data taking. The flexibility of software L1-L2 triggers is ensured by many available options and features, such as global and individual trigger downscaling, by-passing and flagging options. During data taking, the online performances of L1-L2 triggers can be controlled with data sub-samples in which the events are flagged with the trigger verdicts, the ratios of flagged over total events within the sub-samples are computed and compared with expectations. Several data channels selected by different L1-L2 trigger chains can be handled in parallel by means of conditional data-stream using exclusive bandwidth depending of the different L0 trigger mask.

6.2.1 The L1 algorithms

All the L1 trigger algorithms are implemented in the na62-trigger-algorithms project within the NA62 PC-farm framework. The algorithms implemented and available during the 2015 run are the algorithms for the RICH, KTAG, CHOD and LAV sub-detectors. In particular the following algorithms have been studied with data collected during the 2015 run:

1. the L1 KTAG algorithm cutting on the minimum number of KTAG sectors (light-boxes) fired in time with the L0 trigger, i.e. ±5 ns with respect to the L0 trigger time;
2. the L1 CHOD algorithm cutting on the maximum number of slabs fired in time with the L0 trigger, i.e. ±5 ns with respect to the L0 trigger time;
3. the L1 RICH algorithm cutting on the spatial range of the PMT hits coordinate fired in time with the L0 trigger, i.e. ±5 ns with respect to the L0 trigger time;
4. the L1 LAV algorithm cutting on the maximum number of LAV hits in time with the L0 trigger, i.e. ±5 ns with respect to the L0 trigger time (all the LAV stations have been used).

During the 2015 run some of the above L1 trigger algorithms have been tested to select $K^+ \to \pi^+\nu\bar{\nu}$ decays that is the main physics goal of NA62. Hence proper cuts have been studied offline in order to select the signal. The offline analysis to compute the L1 trigger rates, the efficiency of the L1 trigger algorithms and the corresponding rejection factors have been performed using reconstructed 2015 data collected at 10% of the nominal beam intensity with a minimum bias L0 trigger requiring at least two hits in the CHOD. The following L0 trigger conditions have been implemented offline in order to develop a suitable L0 trigger to select $K^+ \to \pi^+\nu\bar{\nu}$ decay:

- more than two hits in the RICH;
- no hits in the LAV stations;
- no hits in the MUV3;
- no hits in the IRC;

- no hits in the SAC.

Both the L1 CHOD and L1 RICH algorithms mentioned above, being multiplicity triggers, aim to reject multi-tracks events; the L1 KTAG algorithm aims to reject the non-kaon component of the NA62 secondary beam and the L1 LAV algorithm aims to reject decays with photons at large angle and inelastic interactions.

The following analysis on the L1 trigger algorithms has not been performed by me and it is described to provide a complete scenario of the L1 trigger algorithms performance.

To test the rejection power of each software trigger algorithm and to get a preliminary estimate of the signal efficiency, different event categories are defined within the offline analysis of 2015 data:

- beam tracks;
- kaon decays with multi-tracks in the final state;
- $K^+ \to \pi^+\pi^0$ decays;
- $K^+ \to \mu^+\nu_\mu$ decays.

In the following analysis the track is defined as the track reconstructed with at least three chambers of the spectrometer.

Each event category is selected according to the following requirements:

- **beam tracks**: all the events classified as beam tracks are those that have a single, positively-charged reconstructed track with a Distance of Closest Approach (CDA) less than 2 cm, generated before the fiducial region (z_{CDA} <105m) with a momentum P above 65 GeV/c. The CDA is the minimum distance between a given track and the nominal beam axis;

- **multi-tracks in the final state**: they are events with more than one track in the final state. The vertex of the track is required to be generated from the beam line and to lie in the fiducial region, 105m< z_{CDA}<165m, with a momentum 15 GeV/c < P < 65 GeV/c;

- **$K^+ \to \pi^+\pi^0$ decays**: they are events with one positive track in the final state detected by the spectrometer. As before, the vertex of the track is required to be generated from the beam line and to lie in the fiducial region, 105m< z_{CDA}<165m, with a momentum 15 GeV/c < P < 65 GeV/c. The squared missing-mass (M^2_{miss}) at the decay vertex is evaluated using the nominal K momentum and direction and it is computed assuming the charged-pion mass. The missing mass of a particle is defined as:

$$M^2_{miss} = (P_K - P_{\pi^+})^2, \tag{6.2}$$

where P_K and P_{π^+} are the four-momenta of the K and of the charged detected particle for which the mass of the charged pion has been assumed. The distribution of the missing mass for different kaon decays under the hypothesis that the charged track is a pion is shown in Figure 6.5.

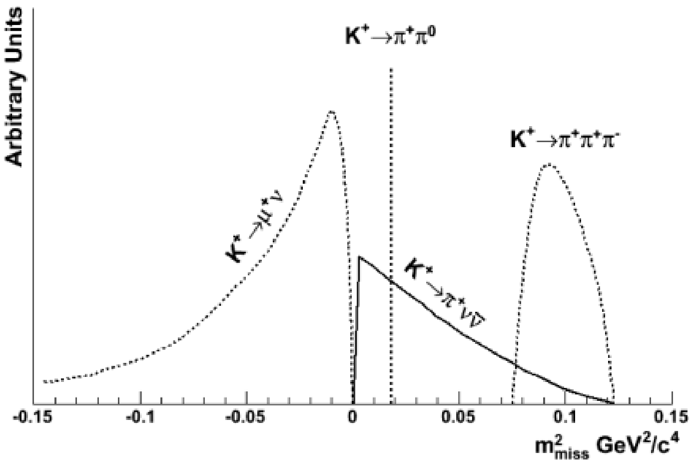

Figure 6.5: Distribution of the missing mass M^2 for the $K^+ \to \pi^+\nu\bar{\nu}$ signal (thick solid line) and background events under the hypothesis that the charged track is a pion.

In order to select the $K^+ \rightarrow \pi^+\pi^0$ decay, the squared missing masses lying in the region 0.01 GeV^2 < M^2_{miss} < 0.025 GeV^2 are selected as shown in Figure 6.5. All the events satisfying the previous conditions are classified as a $K^+ \rightarrow \pi^+\pi^0$ decay;

- **$K^+ \rightarrow \mu^+\nu_\mu$ tracks**: they are events with one positive track in the final state detected by the spectrometer. The vertex of the track is required to be generated from the beam line and to lie in the fiducial region, 105m< z_{CDA}<165m, with a momentum 15 GeV/c < P < 65 GeV/c. The squared missing-mass (M^2_{miss}) at the decay vertex is evaluated using nominal values for the K momentum and direction and it is computed assuming the charged-pion mass. The squared missing mass is evaluated as in 6.2. In order to select the $K^+ \rightarrow \mu^+\nu_\mu$ decay, the missing masses lying in the region -0.02 GeV^2 < M^2_{miss} < 0.01 GeV^2 are selected as shown in Figure 6.5. All the events satisfying the previous conditions are classified as a $K^+ \rightarrow \mu^+\nu_\mu$ decay.

No L2 software triggers have been used during the 2015 run.

The L1 KTAG algorithm

The L1 KTAG algorithm aims to reject the non-kaon component of the NA62 secondary beam, in particular the dominant pion component. From Monte Carlo simulation, the KTAG can distinguish the kaon component of the beam from the pion component by the number of fired KTAG sectors.

Studies on the performance of the KTAG sub-detector [5] show that a cut on the minimum number of sectors (N_{sector}) allows us to select the kaon component of the beam with an efficiency above 95%, and to reduce the pion mis-tagging probability to $\sim 10^{-4}$.

As shown in Figure 6.6, from the offline studies with reconstructed 2015 data collected at 10% of the NA62 nominal intensity, the L1 cut based on the number of fired KTAG sector allows us to reduce the amount of acquired data after the L0 trigger cut ("all

L0 data" points in Figure 6.6) leading to a rejection of the non-kaon component of the beam ("Beam tracks" points in Figure 6.6). The cut is optimised in the plateau area of the data rejection factor, which is about 0.6 if $N_{sector} \geq 4$, that corresponds to a factor 10 reduction for the non-kaon beam component. Efficiency studies give above 95% efficiency for the various categories of kaon decays ("Multi-tracks", $K^+ \to \pi^+\pi^0$ and $K^+ \to \mu^+\nu_\mu$ decays).

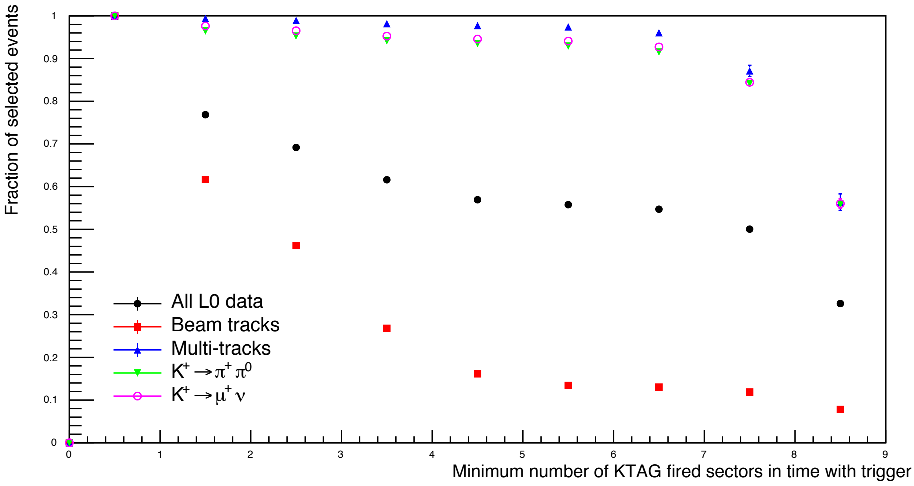

Figure 6.6: Fraction of selected events as a function of the minimum number of KTAG sectors fired within 5 ns with respect to the L0 trigger time. The results are shown for all acquired data after L0 trigger cut ("All L0 data"), for the beam track component ("Beam tracks"), for multi-track kaon decays ("Multi-tracks") and for the $K^+ \to \pi^+\pi^0$ and $K^+ \to \mu^+\nu_\mu$ decays.

The L1 CHOD algorithm

Monte Carlo studies show that the main source of background to $K^+ \to \pi^+\nu\bar{\nu}$ are $K^+ \to \pi^+\pi^+\pi^-$ and $K^+ \to \pi^+\pi^0$ decays. These decays can produce photon-induced showers upstream of the CHOD sub-detector, by interacting with matter on the beam line. A cut based on the multiplicity of the number of hits in the CHOD sub-detector can help in rejecting them.

The cut based on the hit-multiplicity of the CHOD requires a maximum number of CHOD slabs fired in a window of 5 ns around the L0 trigger time. As shown in Figure 6.7, from the offline analysis on reconstructed 2015 data collected at 10% of the NA62 nominal intensity, the request that $N_{slab} \leq 6$ rejects "Multi-tracks" and $K^+ \to \pi^+\pi^0$ decays (Figure 6.7) with a further data reduction of 0.6 obtained on top of the L1 KTAG trigger cut ("All L0 data" points in Figure 6.7).

In order to evaluate the efficiency of the L1 CHOD trigger cut for the $K^+ \to \pi^+\nu\bar{\nu}$ signal, kaon decays with a single charged particle in the final state are taken into account, such as $K^+ \to \mu^+\nu_\mu$ decay. From the offline analysis, an inefficiency of 15% is expected. To improve the performances in rejecting the background, the cut might be tighter, e.g. $N_{slab} \leq 4$, but further validations at higher rates are needed.

The L1 RICH algorithms

Two different algorithms were available during the 2015 run for the RICH sub-detector: the RICH multiplicity and the RICH hit spatial-range algorithm. Both the algorithms were successfully developed, tested and deployed on the PC-farm by me during the 2015 run.

The RICH multiplicity algorithm allows a cut on the number of RICH hits in time with respect to the L0 trigger. The RICH hit spatial-range algorithm allows a cut on the spatial spread distribution of the PMT hits (for more details on the trigger cut see Chapter 4).

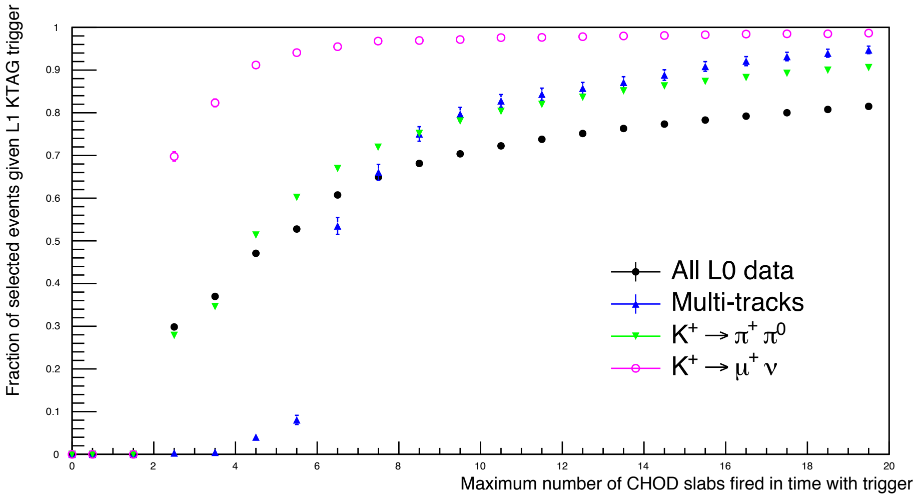

Figure 6.7: Fraction of selected events as a function of the maximum number of CHOD slabs fired within 5 ns with respect to the L0 trigger time. The results are shown for all acquired data after L0 trigger cut ("All L0 data"), for the beam track component ("Beam tracks"), for multi-track kaon decays ("Multi-tracks") and for the $K^+ \to \pi^+\pi^0$ and $K^+ \to \mu^+\nu_\mu$ decays.

Both the algorithms read the data stored in variables from the online TEL62 decoder. The information available are the ID of the TEL62 board, the ID of the TDC, the ID of the PMT channel, the time of the hit and the information indicating if the time is the leading or the trailing edge of the hit.

Both RICH algorithms need to read a configuration file to get some fundamental information on the RICH sub-detector, as the PMT mapping. In order to do that, a "conf-file-reader" class is built to allow the algorithm to read from a configuration file. This class communicates with the RICH trigger algorithms. As this was a feature needed also by the other L1 trigger algorithms, I extended the class so that it became the common interface for all the sub-detector algorithms to access their own configuration file.

It is worth recalling that the RICH photon-detection system consists of 1952 PMT mounted on two flanges. The two flanges are placed one on the right of the beam pipe and the other one on the left upstream the gas tank (Chapter 2). The ID of the PMT readout channel is converted into a geometrical channel read from the configuration file. The geometrical channel contains information like the ID of the flange to which the PMT channel belongs and the ID of the PMT. Once the geometrical channel is given, the algorithm identifies the position of the PMT reading the geographical map of the PMT. The position is read in the reference frame of the PMT flange. It is then necessary to apply a correction to the PMT position in order to have all the PMT coordinates of both flanges in the same reference frame. The correction to the PMT position requires the knowledge of the flange to which the PMT belongs and it is retrieved from the geometrical channel. All these operations from the readout channel to the final correct geographical position of the PMT are performed online within the L1 RICH trigger algorithm.

In order to reject the residual multi-track component, a cut on the spatial range in x (ΔX) or in y (ΔY) of the RICH PMT hits can be considered. This is an alternative cut to the L1 CHOD multiplicity cut.

From offline studies, the request that ΔX or ΔY is smaller than 400 mm, after requiring $N_{sector} \geq 4$ and $N_{slab} \leq 6$, would efficiently reject residual multi-tracks (80% of multi-tracks events are discarded after the L1 RICH trigger cut). On the other hand, it is observed that the cut on the spatial range of the RICH PMT hits to select $K^+ \to \pi^+ \nu \bar{\nu}$ decays might be not so useful after applying trigger cuts using the CHOD sub-detector.

The execution time of the two algorithms (the RICH multiplicity and the RICH hit spatial range algorithm) has been tested directly on the PC-farm by me and it was less than 30 μs for both the algorithms.

The L1 LAV algorithm

Although the main backgrounds to the $K^+ \to \pi^+ \nu \bar{\nu}$, i.e. $K^+ \to \mu^+ \nu_\mu$ and $K^+ \to \pi^+ \pi^0$ decays, are substantially reduced at L0, a further reduction for decays with photons emitted at large angle or with pion inelastic interactions is required at the L1 trigger stage. The LAV hit multiplicity algorithm uses information from all the

LAV stations. This algorithm requires a maximum number of LAV hits fired in a time window of 5 ns around the L0 trigger time. The cut on the number of LAV hits is applied on top of the following L1 trigger cuts:

- $N_{sector} \geq 4$;
- $N_{slab} \leq 6$.

As shown in Figure 6.8, from offline analysis on reconstructed 2015 data collected at 10% of the NA62 nominal intensity, the request of $N_{hit} \leq 2$ rejects $K^+ \rightarrow \pi^+\pi^0$ decays with one or more photons in the final state at large angle, leading to a further reduction on data of 0.75 obtained on top of the L1 KTAG and L1 CHOD trigger cuts (see "All L0 data" points in Figure 6.8). In order to evaluate the efficiency of the L1 LAV trigger cut for the $K^+ \rightarrow \pi^+\nu\bar{\nu}$ signal, kaon decays with a single charged particle in the final state are taken into account, such as $K^+ \rightarrow \mu^+\nu_\mu$ decay. The efficiency results exceed 95%.

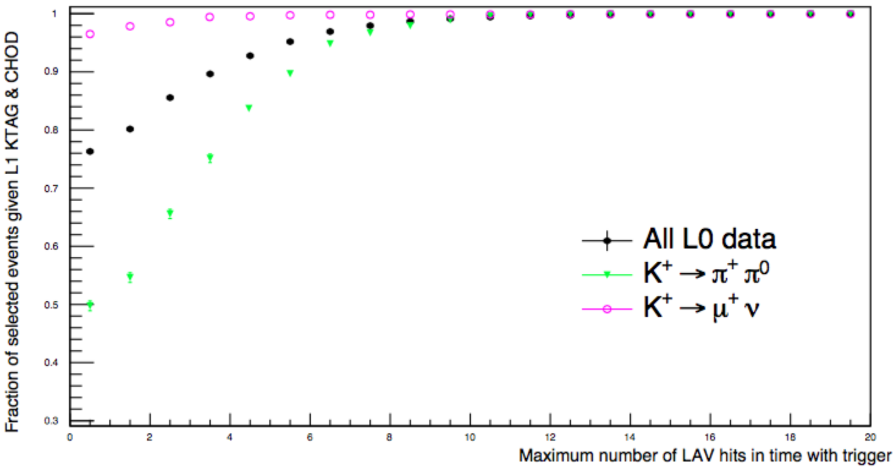

Figure 6.8: Fraction of selected events as a function of the LAV hits fired within 5 ns with respect to the L0 trigger time. The results are shown for all acquired data after L0 trigger cut ("All L0 data"), for the beam track component ("Beam tracks"), for multi-track kaon decays ("Multi-tracks") and for the $K^+ \rightarrow \pi^+\pi^0$ and $K^+ \rightarrow \mu^+\nu_\mu$ decays.

6.2.2 Final considerations

As a result of the offline studies with 2015 data, a combined L1 trigger efficiency and the corresponding rejection power including the KTAG, CHOD, and LAV algorithms has been obtained. The L1 performance has been studied offline with data collected at 10% of the NA62 nominal beam intensity. Two sets of data from different runs have been analysed. The results are summarised in table 6.1.

Run Number	L1 trigger efficiency	Fraction of kept events	Rejection factor
3015	0.763 ± 0.004	0.2071 ± 0.0002	4.829 ± 0.005
3077	0.742 ± 0.005	0.2059 ± 0.0003	4.857 ± 0.007

Table 6.1: Expected performances of L1 combined (KTAG+CHOD+LAV) trigger. Data used for these estimates have been acquired at 10% of the NA62 nominal beam intensity. The uncertainties are only statistical.

The processing time of the L1-combined (KTAG+CHOD+LAV) trigger was continuously monitored during 2015 data taking, by means of a dedicated plot on the NA62 run control displaying the L1-combined trigger processing time per event as a function of the event time within the burst. The distribution of L1-combined trigger processing times for all events within a burst shows an average at 50 μs with tails up to 200 μs at high beam intensities (up to the NA62 nominal intensity).

Conclusions

Potential ways to improve the efficiency of the L1 trigger algorithm are studied. These are critically important because data rejected at L1 cannot be recovered. The official offline algorithm for the reconstruction of trackless rings in the RICH, based on Ptolemy's algorithm, is investigated as a starting point.

The procedure is quite challenging if there are more than one Cherenkov ring to reconstruct in the absence of any information about the ring centre position (trackless ring reconstruction algorithm). The aim of the efficiency study of the RICH multi-ring reconstruction algorithm is to check how many rings the algorithm reconstructs with respect to the number of Cherenkov rings, expected from the Monte Carlo truth, that are above the Cherenkov threshold.

The result of the analysis shows that the efficiency of the official RICH multi-ring reconstruction algorithm is $\sim 70\%$. A further analysis is performed to investigate the reason behind the $\sim 30\%$ inefficiency of the algorithm. From this investigative analysis, it is clear that most of the $\sim 30\%$ inefficiency of the algorithm is due to the hit sharing of the reconstructed rings. It is possible to improve the algorithm performance and make it more efficient by tightening the conditions in the pattern recognition. This would represent an important task for future studies of the algorithm.

In parallel to the algorithm efficiency analysis, studies on the L1 trigger strategy to select multi-track events are performed.

In order to study both the efficiency of the L1 trigger algorithm and the final event rate after applying the L1 trigger cut, the input events to the L1 stage surviving the L0 trigger cut are produced. The sub-detectors I considered in the L0 cut strategy are the CHOD and the RICH sub-detectors. The cut is based on the multiplicity in the RICH and CHOD. In particular, to select multi-track events, at least 10 super-cells in the RICH (R_{10}) and at least one coincidence in the two CHOD planes in a pair of opposite quadrants (Q_X) are required. The results on the L0 trigger rate are a reproduction of the studies described in the internal note NA62-14-07. The incoming event rate at L1 trigger stage after the L0 trigger cut is estimated to be 0.76 MHz. At the nominal beam intensity, 10 MHz of primitives are produced and the L0 trigger cuts have to reduce this rate by a factor 10, and then 1 MHz is the input rate to the L1 trigger stage. The L1 and the L2 trigger cuts have to reduce the input rate by a 10 factor each, in order to write few kHz on disk.

A final cut to select a multi-track signature, as result of the analysis of the PMT hits spatial-range, is $\Delta X > 400$ mm OR $\Delta Y > 380$ mm, giving the acceptance of multi-track events and of one-track events in the signal region of $A_{K^+\to\pi^+e^+e^-} = 82\%$ and $A_{K^+\to\pi^+\nu\bar{\nu}} = 1\%$, respectively. The $K^+ \to \pi^+\nu\bar{\nu}$ is chosen as a good one-single track kaon decay. A suppression factor of 1.5 on the total rate is achieved after the cut on the spatial-range of the PMT hits. Since the L1 trigger cut has to reduce the event rate by a factor 10, it is then necessary to develop a further trigger cut in order to discard the remaining background, using the RICH sub-detector.

The main sources of background to the signal $K^+ \to \pi^+e^+e^-$ are the $K^+ \to \pi^+\pi^0$ (0.14 MHz) and $K^+ \to \pi^+\pi^+\pi^-$ (0.26 MHz) decay channels. The $K^+ \to \pi^+\pi^0$ decay can mimic the signal after the π^0 decay in two photons with a photon conversion in the RICH or before the RICH. Studies on the origin of the total Q_X rate demonstrate that the contribution of the RICH sub-detector in decreasing the Q_X rate from $K^+ \to \pi^+\pi^0$ with respect to the total Q_X would be smaller than 40%.

The $K^+ \to \pi^+\pi^+\pi^-$ is demonstrated to be the second main source of background to multi-track decays. A possible way to distinguish a Cherenkov ring generated by a pion from one generated by an electron is from the distribution of the reconstructed ring radius. From the reconstructed radii distribution, the classification of all the reconstructed rings having radius R $<$ 180 mm as pions leads to the identification of all the rings with a radius R $\geq$ 180 mm as electrons. From the distribution of the number of reconstructed electron Cherenkov rings versus the number of pion Cherenkov rings, both for $K^+ \to \pi^+ e^+ e^-$ and $K^+ \to \pi^+ \pi^+ \pi^-$ sample, it seems that a powerful L1 cut to select $K^+ \to \pi^+ e^+ e^-$ events is to require $N_{electron} > 0$ for which 80% of background is discarded while more than 80% of signal is kept. It is then necessary to develop an algorithm able to identify an electron Cherenkov-ring. The $K^+ \to \pi^+ \pi^+ \pi^-$ event rate, after the $N_{electron} > 0$ L1-request applied on top of the spatial range cut, is 0.15 MHz. Comparing the $K^+ \to \pi^+ \pi^+ \pi^-$ event rate after the L1 trigger cut with the $K^+ \to \pi^+ \pi^+ \pi^-$ rate after the $\mathbf{R_{10}} \cdot \mathbf{Q_X}$ condition required by the L0 trigger, i.e. 0.30 MHz, a rejection factor equal to 2 is obtained.

A new L1 software trigger algorithm to identify an electron Cherenkov ring using the RICH sub-detector is studied. Based on purely geometrical considerations, the algorithm aims to find the centre of the electron Cherenkov-ring. The algorithm performs a spatial scan over the x and y coordinates of points placed on a two-dimensional lattice. Each point represents a potential centre of the ring. In order to find the centre of the electron Cherenkov-ring, for each lattice-point the algorithm computes the number of the PMT hits within an annular region. Various improvements in the algorithm were studied in details.

The three parameters of the hit-scan algorithm to be tuned in order to have a good efficiency are the distance along the x and y axis between two neighbouring points of the lattice, called lattice-step, the region of the lattice where the scan is applied and the path through which the algorithm scans over the points of the lattice. The final values of the inner and outer radii of the electron Cherenkov rings and of the parameters are:

Electron Cherenkov-ring Inner Radius	183 mm
Electron Cherenkov-ring Outer Radius	200 mm
Lattice-step	6 mm
Number of lattice points	5930

These values lead to an efficiency on the $K^+ \rightarrow \pi^+ e^+ e^-$ selection bigger than 80%.

Since the algorithm has to run as online software trigger, improvements are performed to make the algorithm as fast as possible. A final mean-value of the execution time of the algorithm is estimated to be above 2 ms. It is worth noting that the mean value for the execution time of a L1 trigger algorithm is 450 μs and then the hit-scan algorithm is too slow to run as an online software trigger. Further improvements on the execution time are needed.

Finally, an introduction to the software framework running on the NA62 PC-farm is given. A brief description of the NA62 data flow and NA62 data format is also presented.

An offline analysis of the reconstructed data collected during the 2015 run at 10% of beam intensity is described. The aim of the analysis is to study the efficiency of the L1 trigger cuts and the following rejection factors using some sub-detectors, in particular the KTAG, CHOD and LAV. The processing time of the L1-combined (KTAG+CHOD+LAV) trigger was continuously monitored during 2015 data taking. The distribution of L1-combined trigger processing times for all events within a burst shows an average at 50 μs with tails up to 200 μs at high beam intensities (up to the NA62 nominal intensity).

The description of the implementation on the PC-farm of the RICH L1 trigger algorithm is described in detail. The execution time of the algorithm was tested online directly on the PC-farm and it resulted to be less than 30 μs.

Bibliography

[1] F. Halzen and A. D. Martin. Quarks and leptons: An introductory course in modern particle physics. 1984. New York, Usa: Wiley 1984 396p.

[2] G. Aad et al. Observation of a new particle in the search for the Standard Model Higgs boson with the ATLAS detector at the LHC. *Phys. Lett.*, B716:1–29, 2012.

[3] K. A. Olive et al. Review of Particle Physics. *Chin. Phys.*, C38:090001, 2014.

[4] A. Atre, T. Han, S. Pascoli, and B. Zhang. The Search for Heavy Majorana Neutrinos. *JHEP*, 05:030, 2009.

[5] F. Hahn et al. *NA62: Technical Design Document.* Geneva: CERN, Tech. rep. NA62-10-07. edition, 2010.

[6] G.Bernardi, G. Carugno, J. Chaveau, et al. Search for neutrino decay. *Phys. Lett.*, **166B**(4), 1986.

[7] W. Bonivento et al. Proposal to Search for Heavy Neutral Leptons at the SPS. 2013.

[8] M. Anelli et al. A facility to Search for Hidden Particles (SHiP) at the CERN SPS. 2015.

[9] A. Ali, A. V. Borisov, and N. B. Zamorin. Majorana neutrinos and same sign dilepton production at LHC and in rare meson decays. *Eur. Phys. J.*, C21:123–132, 2001.

[10] CHARM Collab., F.Bergsma et al. *Phys. Lett.*, **128B**(361), 1983.

[11] D. A. Bryman, R. Dubois, T. Numao, B. Olaniyi, A. Olin, M. S. Dixit, J. M. Poutissou, and J. A. Macdonald. Search for Massive Neutrinos in $\pi \to \nu_e$ Decay. *Phys. Rev. Lett.*, 50:1546, 1983. [,173(1984)].

[12] T.Yamazaki et al. Search for heavy neutrinos in Kaon Decay. *Proc. Neutrino 84, eds. K. Kleinknecht and E.A. Paschos*, page 183, 1984.

[13] R.Abela et al. . *Phys.Lett*, **105B**(263):183, 1981.

[14] R. Shrock. New tests for and bounds on neutrino masses and lepton mixing. *Phys.Lett.*, **B96.1-2**:159–164, 1980.

[15] F. Newson. *Kaon identification and the search for heavy neutrinos at NA62.* PhD thesis, School of Physics and Astronomy, University of Birmingham, 2015.

[16] J. Dorenbosch et al. A search for decays of heavy neutrinos in the mass range 0.5-2.8 GeV. *Phys.Lett.*, **B166.4**:473–478, 1986.

[17] J.Badier et al. Mass and lifetime limits on new long-lived particles in 300 GeV/c π interactions. *Zeitschrift fur Physik C Particles and Fields*, (31.1):21–32, 1986.

[18] D.I. Britton et al. Measurement of the $\pi^+ \rightarrow e^+\nu$ branching ratio. *Phys. Rev. Lett.*, **68**(20):3000–3003, 1992.

[19] O.Adriani et al. Search for isosinglet neutral heavy leptons in Z^0 decays. *Phys. Lett.*, **B295.3**:371–382, 1992.

[20] P. Abreu et al. Search for neutral heavy leptons produced in Z decays. *Z. Phys.*, C74:57–71, 1997. [Erratum: Z. Phys.C75,580(1997)].

[21] A. Vaitaitis et al. Search for neutral heavy leptons in high energy neutrino beam. *Phys. Rev. Lett*, **83**(24):4943–4946, 1999.

[22] A. Cooper-Sarkar et al. Search for heavy neutrinos decays in the BEBC beam dump experiment. *Phys. Lett*, **B106.1**:207–211, 1985.

[23] E. Gallas et al. Search for neutral weakly interacting massive particles in the Fermilab Tevatron wideband neutrino beam. *Phys. Rev.*, **D52**(1):6–14, 1995.

[24] P. Vilain et al. Search for heavy isosinglet neutrinos. *Phys. Lett.*, **B343.1-4**:453–458, 1995.

[25] R. Aaij et al. Search for Majorana neutrinos in $B^- \rightarrow \pi^+\mu^-\mu^-$ decays. *Phys. Rev. Lett.*, 112(13):131802, 2014.

[26] X. C. Vidal. Searches for Majorana Neutrinos and Direct Searches for Exotics at LHCb. In *LISHEP-International School on High Energy Physics- Session C MANAUS, Amazonas, Brazil, August 2-9, 2015*, 2015.

[27] G. J. Feldman and R. D. Cousins. A Unified approach to the classical statistical analysis of small signals. *Phys. Rev.*, D57:3873–3889, 1998.

[28] K. Massri. *Kaon identification and search for Lepton Number Violation in $K^\pm$ decay-in-flight experiments at CERN.* PhD thesis, School of Physics and Astronomy, University of Birmingham, 2014.

[29] L.L. Chau and W.-Y. Keung. Comments on the Parametrization of the Kobayashi-Maskawa Matrix. *Phys.Rev.Lett.*, 53:1802, 1984.

[30] L. Wolfenstein. Parametrization of the Kobayashi-Maskawa Matrix. *Phys.Rev.Lett.*, 51:1945, 1983.

[31] G. Buchalla and A. J. Buras. The rare decays $K \to \pi\nu\bar{\nu}$, $B \to X\nu\bar{\nu}$ and $B \to ll$: An Update. *Nucl.Phys.*, B548:309–327, 1999.

[32] J. Bijnens and K. Ghorbani. Isospin breaking in K pi vector form-factors for the weak and rare decays K(l 3), K —> pi nu anti-nu and K —> pi l+ l-. 2007.

[33] Gorbahn M. Brod, J. and E. Stamou. Two-Loop Electroweak Corrections for the $K \to \pi\nu\bar{\nu}$ Decays. *Phys. Rev.*, D83:034030, 2011.

[34] M. S. Atiya et al. A detector to search for K+ —> pi+ neutrino anti-neutrino. *Nucl. Instrum. Meth.*, A321:129–151, 1992.

[35] A.V.Artamonov et al., [E949 Collaboration]. Study of the decay $K^+ \to \pi^+\nu\bar{\nu}$ in the momentum region 140< P_π <199 MeV/c. *Phys. Rev.*, **D79**(092004), 2009.

[36] F. Marcastel. CERN's Accelerator Complex. La chaine des accelerateurs du CERN. https://cds.cern.ch/record/1621583, Oct 2013. General Photo.

[37] G.Anelli, et al. (P326 Collaboration). Proposal to measure the rare decay $K^+ \to \pi^+\nu\bar{\nu}$ at the CERN SPS. *CERN-SPSC-2005-013 and CERN-SPSC-P-326*, 2005.

[38] http://doble.web.cern.ch/doble/k12hika+.txt.

[39] P.Valente and F.Hahn. Material for NA62 presentations. http://na62.web.cern.ch/NA62/Documents/MaterialPresentationSchemas.html, 2010.

[40] V. Fanti et al. The beam and detector for the NA48 neutral kaon CP violation experiment at CERN. *Nuclear Instruments and Methods in Physics Research Section A: Accelerators, Spectrometers, Detectors and Associated Equipment*, 574:433–471, 2007.

[41] F. Ambrosino et al. The CHarged ANTIcounter for the NA62 Experiment at CERN. *Physics Procedia*, (2012).

[42] C.Bovet, et al. The CEDAR Counters for Particle Identification in the SPS Secondary Beams. *CERN Report:CERN 82-13*, 1982.

[43] E. Goudzovski et al. Development of the kaon tagging system for the NA62 experiment at CERN. *Nucl. Instrum. Meth.*, A801:86–94, 2015.

[44] K. Nakamura and Particle Data Group. Review of particle physics. *Journal of Physics G: Nuclear and Particle Physics*, 37(7A):075021, 2010.

[45] E. Tamm, I. M. Frank. Coherent radiation of a fast electron in a medium. *Dokl.Akad.Nauk SSSR*, 14:107–112, 1937.

[46] M.Lenti. Progress of the NA62 RICH detector. *Journal of Instrumentation*, 9.01: C01054., 2014.

[47] NA62 Collaboration. 2015 NA62 Status Report to the CERN SPS. Technical report, CERN, 2015.

[48] F. Anghinolfi, P.Jarron, F. Krummenacher, E. Usenko, and M. Williams. NINO: An ultrafast low-power front-end amplifier discriminator for the time-of-flight detector in the ALICE experiment. *IEE Trans.Nucl.Sci*, 51:1974–1978, 2004.

[49] F. Anghinolfi, P. Jarron, F. Krummenacher, E. Usenko, H. Wenninger et al. NINO: An ultrafast low-power front-end amplifier/discriminator ASIC designd for the multigap resistive plate chamber. *IEE Trans.Nucl.Sci*, A533:183–187, 2004.

[50] E. Pedreschi, M. Sozzi, and F. Spinella. From TELL1 to TEL62. http://na62.web.cern.ch/NA62/Documents/ReferenceDocuments.html, 2010. NA62-10-06.

[51] J. Christiansen. HPTDC high performance time to digital converter. *Nuclear Science Symposium Conference Record*, 2, 2000.

[52] K. Ahmet at el. The OPAL detector at LEP. *Nucl. Instrum. and Meth.*, A 305, OPAL Collaboration, 275:275–319, (1991).

[53] F.Ambrosino et al. A prototype large-angle photon veto detector for the P326 experiment at CERN. *Nuclear Science Symposium Conference Record. NSS '07. IEE.*, 1: 57–64., (2007).

[54] G. Lamanna. Almagest, a new trackless ring finding algorithm. *Nucl. Instrum. Meth.*, A766:241–244, 2014.

[55] S. Agostinelli et al. GEANT4: A Simulation toolkit. *Nucl. Instrum. Meth.*, A506:250–303, 2003.

[56] NA62 framework. http://sergiant.web.cern.ch/sergiant/NA62FW/html/.

[57] A. Cassese. Particle ID with RICH, December 2013. NA62 Physics Working Group CERN.

[58] E. Goudzovski and C. Parkinson. Studies of the L0 trigger for rare decays. http://na62.web.cern.ch/NA62/Documents/ReferenceDocuments.html, 2014. NA62-14-07.

[59] D. C. Carey, K. L. Brown, and F. C. Iselin. Decay TURTLE (Trace Unlimited Rays Through Lumped Elements): A Computer Program for Simulating Charged Particle Beam Transport Systems, Including Decay Calculations. 1982.

[60] M. de los Reyes. Preliminary studies of the NA62 RICH L1 trigger. http://na62.web.cern.ch/NA62/Documents/ReferenceDocuments.html, 2014. NA62-14-08.

[61] $http : //www.ntop.org/products/packet - capture/pf\_ring$.

[62] NA62 TDAQ Working group. NA62 data formats. https://twiki.cern.ch/twiki/pub/NA62/TdaqSystem/DataFormats.pdf , 2016.